UNIVERSITAT DE BARCELONA

Coupling fluid-dynamics and non-thermal processes to study sources of high-energy emission

Víctor Moreno de la Cita

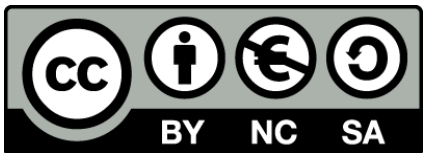

UNIVERSITAT DE
BARCELONA

COUPLING FLUID-DYNAMICS AND NON-THERMAL PROCESSES TO STUDY SOURCES OF HIGH-ENERGY EMISSION

VÍCTOR MORENO DE LA CITA

Programa de Doctorat en Física
Línia de Recerca en Astronomía i Astrofísica
2013 – 2017

Tesi doctoral presentada por Víctor Moreno de la Cita
per optar al títol de doctor per la Universitat de Barcelona

DIRECTORS
Dr. Valentí Bosch Ramon
Dr. Dmitry Khangulyan

TUTOR
Dr. Alberto Manrique

Víctor Moreno de la Cita: *Coupling fluid-dynamics and non-thermal processes to study sources of high-energy emission*, January 2017
Front page: adapted from an ilustration by Ana Yael (www.anayael.net)

Dedicado a mis padres y mi hermana

I'm doing science but I'm still alive.

— GLaDOS

(...) I wander'd off by myself,
In the mystical moist night-air, and from time to time,
Look'd up in perfect silence at the stars.

— Walt Whitman

RESUMEN

En estos más de tres años de investigación hemos trabajado en uno de los grandes problemas de la astrofísica de altas energías: cuál es el mecanismo de producción de radiación no térmica en fuentes relativistas. Nosotros hemos propuesto una serie de modelos centrándonos en la relación de *outflows* relativistas con su entorno, proponiendo que si éstos interaccionaban con ciertos obstáculos, formarían choques. En estos choques, aunque en el caso relativista aún no se tiene un conocimiento profundo de su funcionamiento, se sabe que se produce aceleración de partículas no térmicas, dando lugar también a emisión de altas energías.

Distinguimos la emisión no térmica (responsable de los fenómenos que emiten rayos gamma, que son los que más nos interesan) de la térmica porque, a diferencia de ésta, no se produce por la agitación aleatoria de las partículas debido a su temperatura. La emisión no térmica involucra a menudo la interacción de las partículas con los campos electromagnéticos de sus alrededores. En nuestro caso, nos hemos centrado en la emisión IC *(Inverse Compton*, interacción partícula-fotón) y en la emisión sincrotrón (interacción partícula-campo magnético) porque eran las más relevantes en nuestros casos de interés.

El método que hemos seguido para estudiar los distintos casos ha sido el siguiente: nuestros colaboradores hacían simulaciones hidrodinámicas (2D, relativistas, con simetría cilíndrica, para más información, ver Cap. 2) de la fuente de interés, obteniendo una red de datos en dos dimensiones. Después reducían el problema a una serie de líneas de fluído (ver Sec. 2.1.1), que contenían los datos hidrodinámicos que nos facilitaban a nosotros.

Con estas líneas de fluido nosotros calculábamos la inyección de partículas no térmicas siguiendo una serie de prescripciones fenomenológicas sobre su distribución de energías, su evolución a lo largo de la línea de fluido y del tiempo, y por último su radiación no térmica (IC y sincrotrón). Con este método podíamos obtener las distribuciones espectrales de nuestras fuentes, así como mapas de emisión.

Hemos empleado este método para estudiar tres tipos de fuentes:

INTERACCIONES JET–ESTRELLA EN AGNS

Algunas galaxias que tienen un núcleo de galaxia activo (AGN, por sus siglas en inglés) presentan un par de chorros de partículas relativistas, muy colimados y opuestos, también conocidos como *jets*. La formación de estos jets está ligada a episodios de colisión de galaxias, un proceso llamado *merging* que también suele implicar que se dispare el ritmo de formación estelar. De esta forma, es esperable que el número de interacciones de estos jets con las poblaciones de estrellas circundantes sea alto.

Nosotros nos centramos en una sola interacción, para la que simulamos un jet persistente interaccionando con una estrella individual (Cap. 3). El resultado de estas simulaciones es que el área efectiva donde se produce la emisión no térmica es mucho mayor que el área asociada a la región donde el choque es más intenso, por lo que la cantidad de radiación que puede generar es mayor de la que se esperaba. En cuanto a los resultados radiativos, observamos que la orientación del jet con respecto al observador (situado en la Tierra) es de vital importancia, debido al efecto Doppler que sufre la radiación, al ser el jet relativista. También observamos que un campo magnético relativamente alto puede atenuar mucho la componente IC de la radiación y, por tanto, disminuir la emisión por encima del GeV. Los niveles energéticos que encontramos hacen pensar que una población de estrellas interactuando con el jet de un AGN podrían dar lugar a emisión gamma detectable desde la Tierra.

PÚLSAR INTERACCIONANDO CON UN VIENTO ESTELAR INHOMOGÉNEO

Las binarias de rayos gamma son sistemas de dos cuerpos en los que uno es un objeto compacto (básicamente, un agujero negro o una estrella de neutrones) y el otro es una estrella, con la peculiaridad de que su distrubución espectral de emisión (SED) tiene el máximo por encima de 1 MeV, es decir, están fuertemente dominados por procesos no térmicos. La emisión en rayos gamma de estas binarias ha sido estudiada con anterioridad, pero aquí nos centramos, de nuevo, en la interacción de un viento relativista (en este caso, proveniente del púlsar) con un obstáculo de gran inercia (en este caso, una inhomogeneidad del viento estelar). Estas inhomogeneidades, o grumos (*clumps* en inglés), pueden tener una densidad considerablemente mayor que el resto del viento estelar, y se espera que estén presentes en los vientos de las estrellas más masivas (Cap. 4).

La interacción del viento del púlsar con el grumo del viento estelar produce una región chocada alrededor de este último. En función del tamaño y la densidad del grumo, esta región chocada puede acercarse más al púlsar, siendo afectada así por un viento más potente, menos diluído, modificando los patrones de pérdidas de energía de las partículas. Con nuestros cálculos hemos podido comprobar cómo al introducir estas inhomogeneidades se consiguen efectivamente emisiones significativamente mayores en la mayoría de configuraciones.

Este modelo se ha aplicado a una fuente concreta, la binaria PSR B1259–63, no siendo posible explicar los estallidos en la banda de los GeV observados por Fermi. Por otra parte, para esa misma fuente se encontró que si se modelaba el disco de decreción que se espera que tenga la estrella compañera como una inhomogeneidad grande interactuando con el viento del púlsar, la SED se acercaba más a las luminosidades en TeV observadas 20 días después del periastro, apuntando a una relación entre el objeto compacto y el disco de decreción como fuente de rayos gamma en el rango TeV.

INHOMOGENEIDADES DE UN VIENTO ESTELAR EN UN JET DE HMMQ

Los microquásares de alta masa (HMMQ, por sus siglas en inglés) consisten en un objeto compacto orbitando alrededor de una estrella masiva. Parte del material de la estrella, que en este caso tiene vientos muy poderosos, es acretado por el objeto compacto formando una pareja de jets. En nuestro estudio, hemos intentado modelar la emisión gamma explorando el escenario en el que ciertas inhomogeneidades en el viento estelar (de nuevo, grumos) eran capaces de entrar en el jet, provocando un choque y, por lo tanto, acelerando partículas no térmicas.

El estudio, en este caso, tuvo dos componentes importantes, el cálculo de las condiciones necesarias para que la interacción entre el grumo del viento estelar y el jet fuera posible y eficiente, y la simulación del proceso, llevadas a cabo por nuestros colaboradores; y el posterior cálculo de la radiación no térmica, llevada a cabo mediante el código desarrollado en esta tesis. La primera parte del estudio estimaba que básicamente deberíamos esperar que más o menos siempre hubiese una inhomogeneidad del tamaño y densidad estudiados interaccionando con el jet. Grumos más grandes serían menos probables y quizá demasiado masivos para el jet, disgregándolo en el proceso, mientras que grumos más pequeños, menos

densos, o impactando en las zonas más cercanas a la base del jet, serían destruídos antes de poder penetrar.

En este caso, aunque el trabajo se hizo de forma genérica para cualquier microquasar de alta masa, nos centramos en los dos HMMQs que emiten en rayos gamma que se conocen hasta la fecha, Cyg X-1 y Cyg X-3. El resultado de nuestro trabajo es que con los parámetros que nosotros manejamos pueden reproducirse las luminosidades de estas fuentes imponiendo eficiencias no térmicas conservadoras. Incluso comparamos las SED predichas con las observaciones Fermi de Cyg X-1, mostrando que son compatibles empleando valores razonables del campo magnético, ángulo de visión y eficiencia en la aceleración de partículas no térmicas.

AGRADECIMIENTOS

En (aproximado) orden cronológico: a mi madre. Darme a luz te debió parecer un juego de niños cuando más tarde te tocó lidiar con alguien (todavía) más cabezota que tú. Me has enseñado a querer y a respetar mi opinión y la de los demás, a llevar la contraria y a dudar siempre, y creo que de eso va la ciencia. A mi padre, porque no hay nada mejor que tener un padre maestro, que te dedica sus tardes y sus veranos como si fuese lo más natural del mundo. Aquel brick de leche en la cima de la peña del Cuerno estaba sentando las bases de algo. A los dos, junto con el resto de mi familia, porque he sido profundamente feliz y querido, y eso es lo más importante que me podíais dar. No hay manera de agradecéroslo suficientemente.

A mi hermana, por la ostia de razones. Por ser un referente vital con diez años menos, porque te admiro y aprendo de tí cada día. Sin tí sería mucho peor persona y mucho más estúpido, así que, de parte del mundo, gracias.

A Martita.

A mis amigos, por darme palos hasta en el carnet de identidad, siempre. Los musmen, mis primeros amigos de verdad, la amistad que se forja en una charanga es inmortal. Qué trabajo tenemos estos meses, entre confesionarios y paracaídas. Los colegas del Zambrano, porque sigo sintiéndoos super cerca aunque os tenga muy lejos, porque con vosotros aprendí lo bonito que es ser revolucionario. Los compañeros de la carrera, con vosotros he aprendido más que con ningún profesor universitario; entre otras cosas, que la ciencia puede ser apasionante y que consiste en compartir el conocimiento. La gente del máster y derivados, el año más divertido de mi vida lo pasé íntegro con vosotros, qué necesarios son los amigos para recordarte lo que has hecho alguna noche. A mis compañeros de piso, porque nunca digo *mi piso*, sino *mi casa*, y eso es gracias a vosotros.

A Mar.

A la gent del DAM, si he acabat el doctorat sense recórrer a assistència psiquiàtrica ha estat pels nostres dinars a la terrassa. Quan anar a la feina es un plaer, tot és molt més senzill. JR, por salvarme el culo una y otra vez. Lluis, tus competiciones de galletas casi acaban con mi salud. Xavi y Benito, sigo odiando Python. María, Rosa, Neus, qué facil es echaros de

menos. Flor, quiero volver a irme de congreso contigo, mejor si es a La Plata. Núria, te felicito, tenerme de compañero de despacho en exclusividad puede acabar con el más valiente... ¿quieres queso? Santi, caminar a tu lado por la montaña es un ejercicio (extremo) de aprendizaje. Lluis, Sara, Estef, Pacheco, menos mal que tengo gente que me apoya con los temas disparatados en la comida. Nico, no descansaré hasta que conozcas todo el refranero español. Dani, eres mi mejor referencia friki, y mira que he tenido. Núrias, Guillem i Pol, molt d'ànims amb la investigació. Roger, gracias por enseñarme que en el DAM se puede hablar de todo menos de Bola de Drac, esa mierda sobrevalorada. Ups. Jose, ¿quién nos manda meternos en estos rastaberenjenales? Pere, [símbolo de corazoncito] no veo el momento de hacernos un selfie con la Moreneta. Laia, et trobaré a faltar com a ningú. És un plaer treballar (i ballar, i ensenyar...) amb tu, quina caixa de sorpreses. E Ignasi, a fuerza de no entender lo que decías me has hecho entender cómo piensas. Y eres un tío genial, por lo que he visto. Moltes gràcies per ser, des de el primer dia, un boníssim amic.

To Gill.

A mis compañeros de cordada, sé que atarse al otro lado de mi cuerda no es fácil, gracias por llevarme a sitios que antes solo podía soñar. Realmente este doctorado os debe mucho, igual que mi salud mental y mi felicidad en general. A las meves companyes de ball, per el vostre somriure encara que us trepitgés o us llancés contra les columnes de la Iguana.

A mis maestros Mario, Fermín, Enrique, Fernando y Pedro, Esteban, Luís, Cesca y tantos otros. Gente que transmite su pasión y que te impone retos. A mis alumnos, especialmente a mis Joves i Ciència, porque aunque suene a tópico me habéis enseñado mucho más de lo que yo os he enseñado a vosotros. A mis colaboradores, de los que he aprendido muchísimo: Manel, Santiago, Gustavo. Al meu director Valentí, per ensenyar-me tot el que sé sobre coses que es mouen ràpid i s'estampen amb altres coses. La gent diu que és normal voler matar al teu director de tesi i amb tu mai he sentit aquest impuls, això vol dir alguna cosa. To Dmitry, for his maths, and more importantly for a very important month in Tokyo. Japan is always an experience, I guess.

También a toda la gente que hace su trabajo impecablemente, en la sombra, sin llevarse nunca crédito por ello. Son secretarios, informáticos, programadores (hay mucho software libre en esta tesis), equipadores, entrenadores, tipógrafos, cineastas, escritores, ingenieros, cocineros... En definitiva, gracias a todo aquél que tuvo una palabra amable, que compartió su tiempo conmigo antes y durante esta tesis.

Per últim, a la Nadia. Perquè has estat una de les millors sorpreses de Barcelona, perquè una conversa amb tu és, sempre, un descobriment, i per que tens els llavis més bonics del Vallès. Com a mínim. Pel futur.

CONTENTS

Part I

ASTROPHYSICAL INTRODUCTION AND METHODS

1

ASTROPHYSICAL SOURCES UNDER STUDY

1.1 HIGH-ENERGY ASTROPHYSICS

There have been a few moments in history when astronomy has jumped a step ahead by opening a new observational window in the sky. The discovery of gamma rays in astronomy is, in that sense, comparable to the use of the first optical telescope, the first astronomical detections of non-visible wavelengths (infrared, ultraviolet, radio, X-rays) or, more recently, the direct detection of gravitational waves. With the gamma-ray astronomy we enter the exciting domain of the non-thermal (NT) radiation: for the first time we know positively that the origin of that light is not thermal; it cannot be modelled by a black-body spectrum and must be generated by accelerated particles. This allows us to explore the most extreme events in the universe, far from equilibrium and, therefore, of non-thermal nature.

Motivated by the first discoveries in radio astronomy, in the early 1950s the interest in the most energetic band of the spectrum started to grow. The first prediction of gamma rays from space was published by Hayakawa,

1952, in a work predicting a galactic diffuse gamma ray background coming from the decay of pions produced in the interaction between cosmic-rays and interstellar matter. This pioneering publication was soon followed by others, foreseeing an easy detection of this new light. However, given that the atmosphere of Earth is opaque to gamma rays, the necessity of placing the telescope in space delayed the first observations by several years. The first gamma ray telescope (the Explorer XI) was launched in April 27, 1961, and managed to detect the first cosmic gamma ray photon (Kraushaar et al., 1965). Since that pioneering detection until the first astronomical discovery through gamma rays there was a span of more than 20 years: it was the detection of the Geminga pulsar by the NASA satellite SAS-II (reported as an unidentified source by Thompson et al., 1977), what paved the way of precision astronomy in gamma rays. Launched in 1975 and with a lifetime of $\sim$ 7 years, the ESA satellite Cos-B detected several binary systems and γ-ray pulsars in the 2 keV - 5 GeV range.

The next big step forward in gamma-ray astronomy took place in the 1990s with the launch of the Compton Gamma-ray Observatory (CGRO), with the key instruments Imaging Compton Telescope (COMPTEL) (0.75 - 30 MeV) and Energetic Gamma Ray Experiment Telescope (EGRET) (30 MeV - 20 GeV) on board. The latter conducted the first all sky survey above 100 MeV and discovered 271 sources (Hartman et al., 1999). Currently, the high energy (HE) gamma-ray range ($\sim$ 0.1 – 100 GeV) is observed mainly by Fermi[1] (launched in 2008) and AGILE[2] (launched in 2009), with improved sensitivities and spectral, time and spacial resolutions.

In the XXI century a window to even higher energies has been opened with the operation of modern ground-based Imaging Atmostpheric Cherenkov Telescopes (IATCs). These telescopes detect the Cherenkov light produced by the electromagnetic cascades that take place in the Earth's atmosphere when a gamma-ray photon arrives to its upper layers. That technique allows to reach decent sensitivities above 100 GeV, i. e. the very high energy (VHE) range. The current most important IATC are MAGIC[3], H.E.S.S[4], VERITAS[5] and HAWC[6], and the future Cherenkov Telescope

1 Fermi Gamma-ray Space Telescope
2 Astro-Rivelatore Gamma a Immagini LEggero
3 Major Atmospheric Gamma Imaging Cherenkov Telescopes
4 High Energy Stereoscopic System
5 Very Energetic Radiation Imaging Telescope Array System
6 High-Altitude Water Cherenkov Observatory

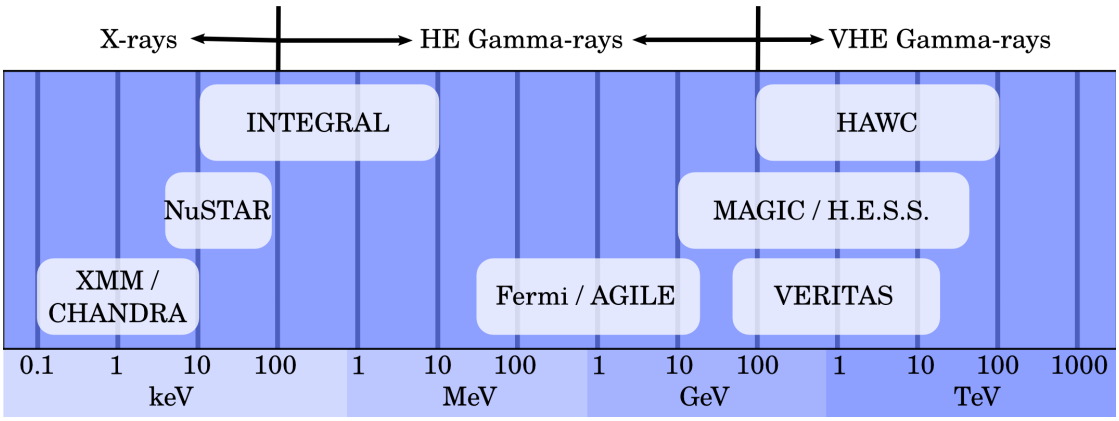

Figure 1.1: Electromagnetic spectrum above 100 eV, in logarithmic scale, showing the effective energy range of the most important missions ongoing at the moment of this thesis publication. The future CTA will cover the range between 10 GeV and ~300 TeV. Please note that all the missions operating below 10 GeV are space telescopes whereas the ones above that threshold are ground-based IATCs.

Array (CTA) has been approved. An overview of the current and future X-ray and gamma-ray telescopes is shown in Fig. 1.1.

1.2 GAMMA-RAY SOURCES

Among the identified gamma-ray sources we find a vast *zoo* of astronomical objects, of both galactic and extragalactic origin, transient and persistent sources, point-like and extended emitters. An overview of the whole-sky at gamma rays and very energetic gamma rays is shown in Figs. 1.2 and 1.3, respectively. The only intrinsic characteristic these sources have in common is the existence of NT processes playing an important role on their emission.

1.2.1 *Thermal vs. non-thermal radiation*

Thermal radiation is the electromagnetic radiation produced by a body with a given temperature, due to the random (thermal) motion of its charged particles. For a system, to reach gamma rays, it should get temperatures of thousands of millions of Kelvin and be optically thin, which is not found in nature. Hence, with gamma rays we can be sure that what we observe is of non-thermal origin.

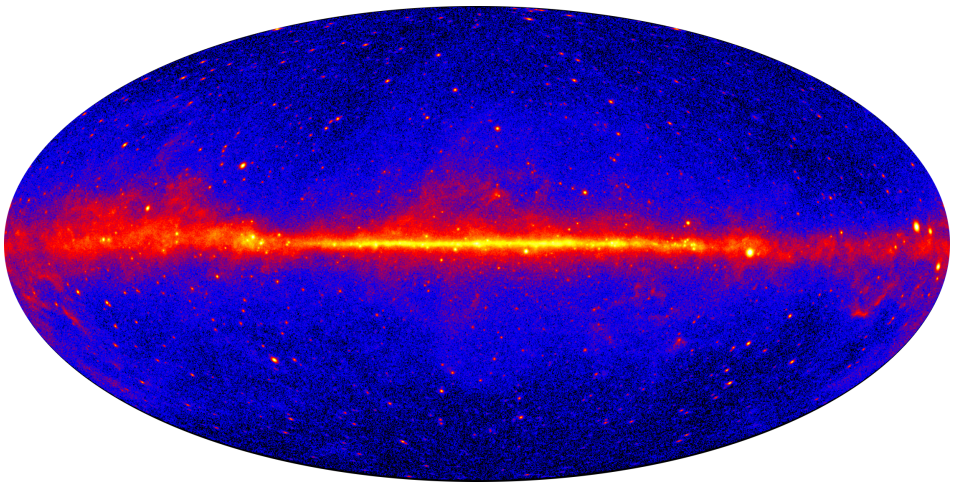

Figure 1.2: All sky view at energies greater than 1 GeV, based on five years of data from the LAT instrument on the Fermi Gamma-ray Space Telescope. Credit: NASA/DOE/Fermi LAT Collaboration (`http://fermi.gsfc.nasa.gov/ssc/`).

All NT processes involve the presence of accelerated particles (see Sec. 2.2), and shocks and other sort of energy dissipation processes inside plasmas are good sites to accelerate charged particles, so we are very interested in sources presenting them. On the other hand, relativistic motion of the emitter will boost the emitted radiation towards higher energies and luminosities if the bulk velocity is *roughly* pointing towards us (see Sec. 2.4.1). Taking this into account we have focused in this thesis on sources with relativistic outflows that are embedded in complex environments, which favours the acceleration of particles, for instance, in shocks.

1.3 GAMMA-RAY SOURCES WITH RELATIVISTIC OUTFLOWS

Here we mostly overview the main types of gamma-ray sources with intrinsic motions comparable with c, the speed of light. This relativistic motion is the responsible for the Doppler boosting, described in 2.4.1, which, if the outflow points towards the observer, amplifies the luminosity of the source and shifts the spectrum to higher energies.

1.3.1 *Active Galactic Nuclei*

The centre of some galaxies presents an Active Galactic Nucleus (AGN), a region of extraordinary luminosity in a wide range of wavelengths, both

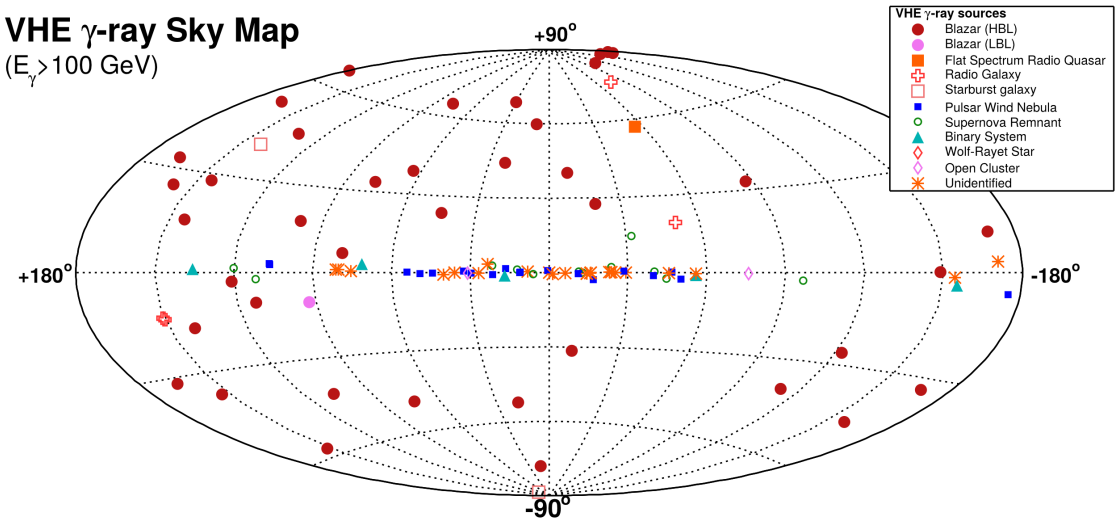

Figure 1.3: All sky view of the sources detected above 100 GeV. An up-to-date plot is available at `http://fermi.gsfc.nasa.gov/ssc/`.

as continuum and spectroscopic line emission. These phenomena are related with the accretion of surrounding material onto the central supermassive black hole (SMBH), supposedly through an accretion disk that can create two relativistic collimated outflows, or *jets*.

In the optical range, a bright point-like continuum in the centre of the galaxy may be present, as well as broad and/or narrow emission lines. Also it may show reprocessed infrared (IR) emission, extended radio emission and both continuum and emission lines in X-rays. Some of these radiation components are related to NT processes but in some cases it is hard to disentangle from the thermal contribution of the host galaxy. In the case of the gamma rays coming from these objects, the NT origin is clear, as well as in general their relation with the relativistic jets. Moreover, if the jet is pointing towards the observer, these objects can reach very high luminosities, and therefore, can be seen even at cosmological distances. The first observation of this kind of sources was the quasar[7] 3c 273, the optically brightest AGN in the sky. A deeper description of these objects from the point of view of their HE component can be found in Chap. 3.

7 Portmanteau of *quasi-stellar* object, due to their resemblance to stars in the optical range, except for the broad emission lines.

1.3.2 *Gamma-ray binaries*

A gamma-ray binary is a two-body system formed by a compact object —namely, a neutron star (NS) or a black hole (BH)— and a companion star, and with the NT spectral energy distribution (SED) peaking in the gamma-ray range. These systems, given the shorter, *human* time-scale of their periods and their extreme environments, are perfect laboratories to study phenomena like particle acceleration, magnetic plasmas, radiation absorption, etc. Although systems with low-mass companion may exist, the companion stars in gamma-ray binaries are massive, presenting high mass-loss rate and strong winds, which play an important role in the NT emission of the system. Up to now, there are only a handful of these sources, listed in Dubus, 2013; Paredes-Fortuny, 2016.

There are two main different scenarios for gamma-ray emitting binaries, depending on whether the compact object is accreting or not. If the compact object does not accrete material from the companion star, then the NT radiation is produced by the collision of the relativistic pulsar wind with the stellar wind, and it is the shock between the two winds what accelerates particles. The accreting compact objects can also emit in the gamma-ray range, but in this case the high-energy emission peak falls in the X-ray band, and hence are known as X-ray binaries. The gamma-ray emitting X-rays binaries pertain to the class of microquasars.

1.3.3 *Microquasars*

Among the X-ray binary population, microquasars are of special interest for gamma-ray astronomy, given that two of these sources, Cyg X-1 and Cyg X-3 have been detected above GeV (Zanin et al., 2016; Tavani et al., 2009, respectively). This kind of sources are binary systems that host a compact object accreting material from its stellar companion, which forms an accretion disk and two jets, in a similar manner to those formed in a quasar, but orders of magnitude smaller and less powerful (this is where its name comes from).

In the specific case of Cyg X-1 and Cyg X-3, the companion is a massive star with powerful winds, which, as has been stated before, has great importance concerning NT processes.

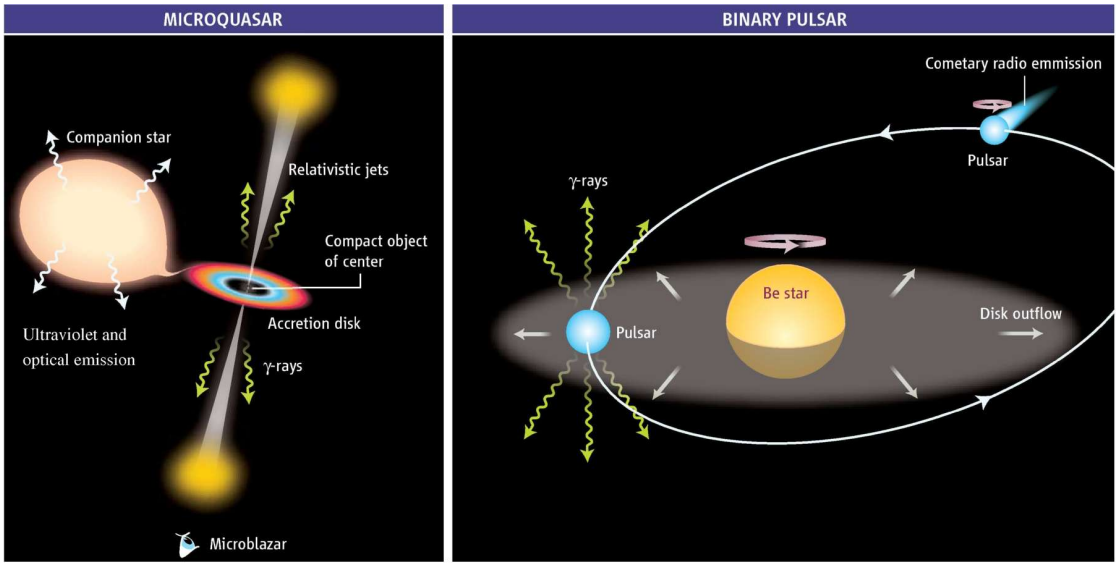

Figure 1.4: Representation of the two classic models of gamma ray production in binary systems, on the left the microquasar scenario and on the right the binary pulsar scenario. Credit: Mirabel, 2006

1.3.4 *Gamma-ray Bursts*

Among the gamma-ray emitters with relativistic outflows, Gamma-ray Bursts (GRBs) are the only kind that we have not studied within this thesis. These sources were discovered in the 1960s by the military *Vela* program during the cold war, while the US government was looking for evidences of soviet nuclear tests. The discovery was declassified and published years later, by Klebesadel et al., 1973.

GRBs appear to be fast transients[8] related to catastrophic events such as compact-object mergers and core-collapse supernova. Also, the isotropic distribution of GRBs in the sky (see Fig. 1.5) points towards an extragalactic origin. Given their enormous bolometric flux, these events are supposed to be related to flows highly collimated towards the observer, and presenting very high Lorentz factors.

GRBs are even more energetic than AGN but take place in time-scales associated with stellar-mass objects, as microquasars; thus, GRBs can be seen as an extreme version of these two other sources. Therefore, at this stage we have decided to focus on AGN and high-mass microquasars, together with gamma-ray binaries hosting a non-accreting pulsar.

8 Between miliseconds, or short GRB, and seconds to minutes, or long GRB.

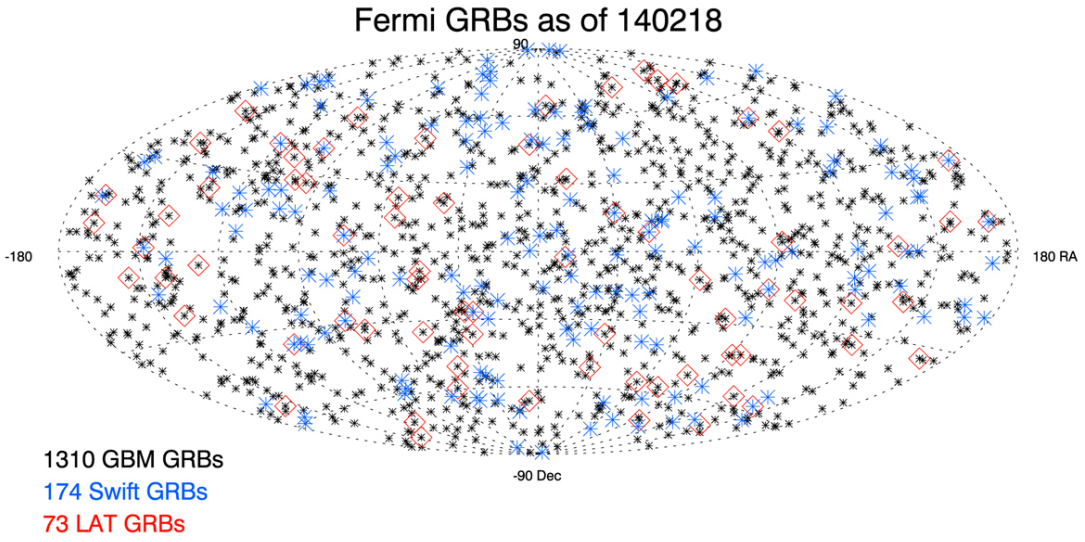

Figure 1.5: GRBs observed by the GBM instrument on board the Fermi Gamma-ray Space Telescope (Fermi) satellite, along with the counterparts found by the X-ray telescope Swift and the Large Area Telescope (LAT) afterglow detection in gamma rays. See Gruber et al., 2014; von Kienlin et al., 2014

1.3.5 *Some examples of non-relativistic sources*

Although they are not studied in this thesis, there are some examples of systems with non-relativistic outflows that present gamma-ray emission. The *slower* counterpart of the relativistic gamma-ray binaries would be the massive star binaries (e. g., Eichler and Usov, 1993), in which the acceleration of particles is produced at the site of stellar wind collision. Analogous, but again, slower, than the microquasar jets, are the outflows produced in high-mass young stellar objects, where the interaction with the dense surrounding medium is of capital importance. The termination shocks of the thermal jets are good candidates for particle acceleration and HE emission (Araudo et al., 2007).

1.4 COMPLEX ENVIRONMENTS

As already mentioned, shocks and other processes dissipate energy from the outflows accelerating particles, although acceleration in shocks is possibly the most common mechanism[9]. To produce these shocks a number

9 Shocks are conventional accelerators in the non-relativistic regime. The acceleration in relativistic shocks is not well understood yet.

of scenarios have been proposed, depending on the specific characteristics, structure and size of the source, such as different velocities inside the outflow (Rees, 1978) or asymmetric recollimation shocks produced by external factors (e.g. Perucho and Bosch-Ramon, 2008). However, a general idea can be applied to all supersonic outflows: the formation of shocks due to the interaction of the flow with a massive obstacle. When the flow impacts the obstacle, a shock forms in the former potentially accelerating particles, and if the obstacle has enough inertia, the outflow will not be able to destroy it (at least, immediately). The presence of a complex environment around the source is, then, clearly important.

In the context of AGNs, the interaction of jets with their surroundings (stars, gas, and clouds), and in particular their dynamical impact on the jet, have been studied since long ago (Komissarov, 1994; Bowman et al., 1996). Later on, several authors (Bednarek and Protheroe, 1997; Bosch-Ramon et al., 2012a; Khangulyan et al., 2013; Bosch-Ramon, 2015) proposed these encounters, and specifically jet-red giant interactions, as plausible acceleration sites and, moreover, efficient NT emitters.

For galactic sources, the scenario is even more complex, given that the relativistic outflows we found in nature do not appear only in the form of jets, but may exhibit different geometries, such as the broader wind of a pulsar. In this context, the obstacles found interacting with the outflows are expected to be related with a close star. Density inhomogeneities are thought to be present in the stellar winds of early-type stars[10] (Lucy and Solomon, 1970; Runacres and Owocki, 2002; Moffat, 2008) and these overdensities (or clumps) can be massive enough to have a dynamical effect in the outflow (e. g. Perucho and Bosch-Ramon, 2012 for microquasars or Paredes-Fortuny et al., 2015 for pulsar winds). Such interactions has been proposed to have a close relation with high energy NT radiation (e. g., Araudo et al., 2009; Owocki et al., 2009; Romero et al., 2010; Bosch-Ramon, 2013).

Also, in some cases the inhomogeneity of the environment can be even more extreme, like in the case of fast-rotating Be stars. This type of object are early-type stars with such a fast rotation that their winds are strongly dependent on their latitude, even forming a *decretion* disc around them, where the material is significantly denser than the spherical wind. These objects are present in some gamma-ray and X-ray binaries and therefore are thought to play a role in the NT emission of these sources (Maraschi and Treves, 1981; Tavani and Arons, 1997; Khangulyan et al., 2007).

10 Namely, O-, B- and A-type stars, the most massive kinds.

2

COUPLING HYDRODYNAMICS AND NON-THERMAL RADIATION

Hydrodynamic simulations have been an extremely useful tool in the study of astrophysical problems since the advent of computers. The complexity of these simulations has grown at the same pace as the computational power available, from simple simulations with very few parameters to the modern three-dimensional (3D) codes, gradually including more and more physics. The study of NT sources has also made use of these techniques to understand the dynamical evolution of the systems, but up to now most of the NT radiation computation codes where *one-zone*; i. e., they could not address properly the spacial complexity and extent of the high-energy source.

In this thesis we couple the results of (relativistic) hydrodynamic simulations with the computation of the NT emission, allowing us to take into account the structure of the sources in the model of their emission. The different positions and velocities of the fluid elements of the emmitting flow may be of capital importance to characterize the high-energy radiation, and therefore its precise determination is needed for the study of their interaction with the ambient photon and magnetic fields through inverse Compton (IC) scattering or synchrotron losses, for instance. Also,

a proper characterisation of the fluid allows us to compute more precisely the NT radiation, accounting more accurately for effects like photon absorption or Doppler boosting.

Given the nature of the problems addressed throughout this thesis, we have focused on a specific kind of simulations. First of all, the systems simulated present an axial symmetry that allow us to perform 2D simulations, less complex and time consuming than 3D ones. Also, at this stage, we focus on stationary hydrodynamic solutions, which is enough for our purposes. And finally, we treat only problems in which the radiative efficient population consist of electrons and positrons, specifically with losses and radiation dominated by IC and synchrotron.

In this context, we have followed the next workflow:

- We perform relativistic hydrodynamical (RHD) simulations, obtaining a 2D grid of hydrodynamical data.
- We compute the streamlines (Sec. 2.1.1) from the hydrodynamical results[1].
- We identify the shocks in the streamline, where the acceleration of particles takes place, and assume what fraction of the fluid energy is transferred to a NT population of particles (Sec. 2.2).
- We let the NT population evolve along the streamline, affected by a number of energy losses (Sec. 2.3).
- Finally we compute the IC and synchrotron radiation, accounting for the relevant absorption processes and Doppler boosting (Sec. 2.4).

2.1 RELATIVISTIC HYDRODYNAMICS

Although the hydrodynamic simulations performed in the context of this thesis, were carried out by our colaborators, it is worth to introduce some concepts to understand the methods employed, given that we have made use of hydrodynamical results to compute the NT radiation. Throughout this thesis we have used the results of finite-difference codes based on a high-resolution shock-capturing scheme that solves the equations of RHD in two dimensions (2D) in a conservation form (Martí et al., 1997). An ideal gas with a constant adiabatic index of $\hat{\gamma} = 4/3$, between a relativistic and a non-relativistic index, was adopted for most of the cases, and the magnetic field was assumed to be dynamically negligible.

1 These first two items are done by our collaborators.

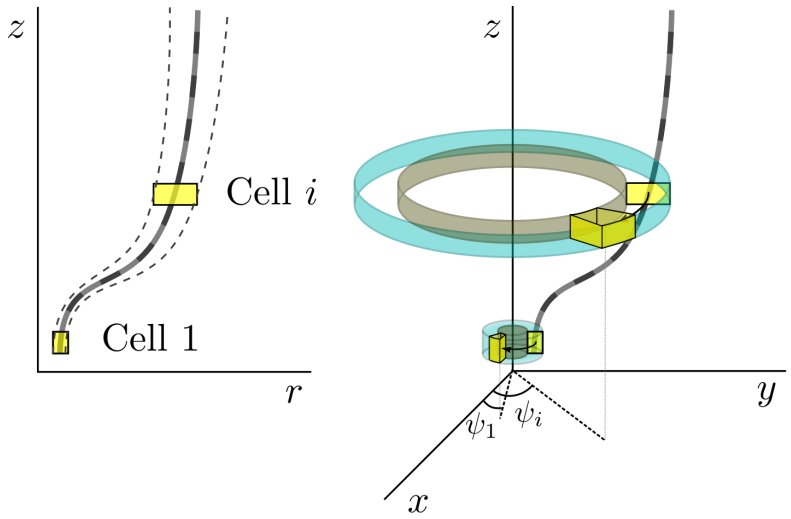

Figure 2.1: Sketch of two cells of the same streamline in the 2D axisymmetric representation (left) and in the real 3D space (right). In the latter, the azimuthal angle ψ_i is also shown.

In each study we specify the particular characteristics of the set-up, so we will not extend here on this issue, but in all cases we have worked with axisymmetric 2D simulations, performed over the same computer: a workstation with two Intel(R) Xenon(R) CPU E5-2643 (3.30 GHz, 4 cores each, with two threads for each core) and four modules of 4096 MB of memory (DDR3 at 1600 MHz).

The output of these simulations is a 2D grid with the hydrodynamic information of each point, which is of little help for our purposes in its *raw* form. Given that we want to follow the evolution of the NT particles, we need to keep track of each fluid element throughout its life inside the grid. To do so, we can identify different fluid elements the locations they are injected in the grid, and compute their spacial trajectories, obtaining the corresponding streamlines.

Before going into detail, there is an important note to be done. All the thesis is developed in the cgs system of units, so unless it is explicitely said, energies are given in ergs, masses in grams, times in seconds, and so on. The vectors are shown in boldface and, in general, any quantity expressed in the comoving frame will have a prime, whereas the quantities in the laboratory frame will not have it.

2.1.1 *Streamline computation*

To compute the streamlines we need the simulation to reach a stationary state, that is, the time it takes for a fluid element to cross the entire streamline has to be shorter than the scale of times of any relevant dynamical change. Then we can introduce a stream function, Φ, as

$$\Gamma\rho\mathbf{v} = \frac{\nabla\Phi \times \mathbf{e}_\psi}{2\pi r}. \tag{2.1}$$

Then the whole grid can be divided into a set of regions, V_i, based on the value of the stream function: $\Phi_{i-1} < \Phi(r,z) \leq \Phi_i$, where $1 \leq i \leq N$ and $\Phi_0 = 0$. We have chosen this condition to impose that the cross section of all of these regions is crossed by the same amount of matter.

In all our simulations the main relativistic outflow is represented along the z axis, pointing upwards, so the beginning of the streamlines is at the bottom of the grid. Given that the grid of hydrodynamic results is 2D, but represents a 3D space, each region forms a 2D layer with axial symmetry in the 3D space, and the cross sections of the regions V_i correspond to a sequence of annular surfaces: $r_{i-1} < r \leq r_i$ (see, in blue, in Fig. 2.1).

If the thickness of these regions is small enough they can be considered homogeneous in the directions perpendicular to the fluid motion, and we can select a streamline that shares characteristics with any other within the same region. Later we divide the streamline into segments by an equidistant time step Δt:

$$\begin{aligned} r_{\mathrm{s},j} &= r_{\mathrm{s},j-1} + v_{r,j-1}\Delta t, \\ z_{\mathrm{s},j} &= z_{\mathrm{s},j-1} + v_{z,j-1}\Delta t, \end{aligned} \tag{2.2}$$

where Δt is the size of the smallest cell divided by the highest speed in the simulation. After each time step, a new position is reached, and we have to apply bilinear interpolation (Press et al., 1992) to get the physical values of interest v_r, v_z, density ρ, and pressure P. The initial point for the streamline in the region V_i is selected as $r_{\mathrm{s},0} = (r_{i-1} + r_i)/2$ and $z_{\mathrm{s},0} = 0$. This division of the streamlines leads to the splitting of the regions V_i into annular cells. Given that the whole fluid has been divided in a number of streamlines, we can easily pass the information of the entire grid to our radiative code.

The cross sections transversal to the flow velocity of the cells, S, can be computed assuming conservation of the energy crossing those sections per time unit:

$$S = S_0 \frac{\rho_0 \Gamma_0^2 h_0 v_0}{\rho \Gamma^2 h v}, \tag{2.3}$$

where

- $\Gamma = 1/\sqrt{1-(v_0/c)^2}$ is the Lorentz factor,
- $h = 1 + \frac{\epsilon}{c^2} + \frac{p}{\rho c^2}$ the specific enthalpy, and
- v the modulus of the three-velocity.

The subscript 0 denotes the conditions at the bottom boundary of the region V_i, that is, in particular,

$$S_0 = \pi\left(r_i^2 - r_{i-1}^2\right). \tag{2.4}$$

We finally downsample each streamline to 200 cells, to reduce the computation time in the non-thermal particle evolution without compromising the accuracy of the final radiation results.

2.1.2 *Magnetic field*

The simulations we have performed do not include the dynamical effect of magnetic fields (i. e., we have not computed magneto-hydrodynamics). Taking them into account requires simulations far more complex, and more time-expensive, and in general the magnetic fields present in the systems of study are weak enough to be safely considered not to be dynamically relevant to first order.

Throughout this thesis we have imposed a value for the magnetic field in the fluid frame (FF) at the beginning of the streamlines equal to a fraction χ_B of the Poynting flux:

$$\frac{B_0'^2}{4\pi} = \chi_B \rho_0 h c v. \tag{2.5}$$

Then, assuming an ideal plasma, we have applied the Alfvén's theorem (or *frozen in* theorem, Alfvén, 1942) which states that in an ideal plasma the conductivity is infinite and therefore the electric field vanishes in the FF. This implies that the magnetic field lines are frozen into the plasma

and have to move along with it, and also that the magnetic field value in the FF B' would evolve along the fluid lines proportional to the section of the streamlines. From Eq. (2.5), we can write, then:

$$B' = B'_0 \sqrt{\frac{\rho v_0 \Gamma_0}{\rho_0 v \Gamma}}. \tag{2.6}$$

We note that χ_B cannot be too large (formally $\chi_B \ll 1$) because otherwise this would collide with the assumption of a dynamically negligible magnetic field made when using a purely RHD code.

2.2 NON-THERMAL PARTICLE INJECTION

With the data from the hydrodynamic simulations we are ready to compute the injection, cooling and radiation of the NT population. The streamlines are divided in 200 cells considered homogeneous, characterised by their position and velocity vector information, pressure (P), density (ρ), section (S), magnetic field (B'), and the flow velocity divergence ($\nabla(\Gamma\mathbf{v})$) to compute adiabatic losses (Sec. 2.3.1). A parameter accounting for wind/wind or wind/jet mixing is also computed, given that in our simulations there is always material of two different origins (e. g. AGN jet + stellar wind). This tracer goes from 0 (100% relativistic outflow) to 1 (100% stellar wind).

Before computing the NT particle evolution, we have to prepare the hydrodynamic data, following some instructions:

1. Read the hydrodynamic data from the streamlines.

2. Read the simulation parameters: the intensity of the magnetic field χ_B, the angle between the line of sight and the z axis in the laboratory frame ϕ, the position, temperature $T_\star$, and luminosity $L_\star$ of the source of target thermal photons (typically, a star), and the acceleration efficiency ($\eta_{\rm NT}$, see Sec. 2.2).

3. Cut the line if the mixing tracer is higher than 0.5 to avoid strong numerical mixing, which affects the radiation results.

4. Identify the sites of acceleration (we call it injection of NT particles in the code) and determine the energetics (luminosity) of the injected population ($L'_{\rm inj}$).

Here we do not choose any specific acceleration mechanism; we just assume that acceleartion takes place in the shocks and we assign a certain efficiency $\eta_{\rm NT}$ to the process. To track the position of the shocks, we assume that they take place at the cells where there is an increment in the internal energy and a decrement in the fluid velocity.

The rate of energy injection in the form of NT particles in the FF $L'_{\rm inj}$ is a fraction $\eta_{\rm NT} \leq 1$ of the generated internal energy per second in the cell U', that is, the time derivative of the 00-component of the energy-momentum tensor times the volume in the FF:[2]

$$\begin{aligned} L'_{\rm NT} &= \chi_{\rm NT} \dot{U}'_k \\ &= \chi_{\rm NT} v_k \Gamma_k^2 \times \left(S_+ \Gamma_+^2 h_+ \rho_+ c^2 \left(1 + \frac{v_+^2}{c^2}\right) - S_- \Gamma_-^2 h_- \rho_- c^2 \left(1 + \frac{v_-^2}{c^2}\right)\right), \end{aligned} \tag{2.7}$$

where $v_{+/-}$ and $\Gamma_{+/-}$ are the velocities and Lorentz factors in the cell right (+) and left (−) boundaries, respectively. This energy rate $L'_{\rm inj}$ gives us the *energetics* of the injected particles. Now we have to assign them a spectral distribution. This is assumed to follow a power-law of index −2, typical for shock acceleration, with two cutoffs at low and high energies:

$$Q'(E') \propto E'^{-2} \left[\exp\left(\frac{-E'_{\rm c,low}}{E'}\right)\right]^5 \exp\left(\frac{-E'}{E'_{\rm c,high}}\right). \tag{2.8}$$

The steep low-energy cutoff is fixed arbitrarily at $E'_{c,low} = 1$ MeV to avoid numerical artefacts, given that it has a moderate impact on the high-energy emission we are interested in. The highe-energy cutoff is more delicate, since it is dependent on the rate at which particles gain energy and determines the highest energy spectrum.

The cutoff is fixed at the energy at which the acceleration timescale is equal to the shortest cooling (diffusion) timescale. For the acceleration times, given that acceleration in relativistic shocks is not well understood yet, we adopt a phenomenological prescription. Therefore, we take $t'_{\rm acc} = \eta E'/qB'c$ with $\eta = 2\pi(c/v)^2$, which tends to ~ 10 when $v \to c$. This expression is correct for acceleration in strong non-relativistic shocks (e. g. Drury, 1983). The shortest cooling or escape timescales are given by the synchrotron timescale, dominant at high energies, $t'_{sync} = 1/a_{\rm s} B'^2 E'$ ($a_{\rm s} = 1.6 \times 10^{-3}$, cgs units[3]), and the Bohm diffusion timescale, $t'_{\rm diff} = R'^2_{\rm a}/2D'$,

2 Reminder: the quantities with prime are expressed in the fluid (comoving) frame.

3 Here we have averaged over the particle momentum-magnetic field pinch angle (see Sect. 2.3.1).

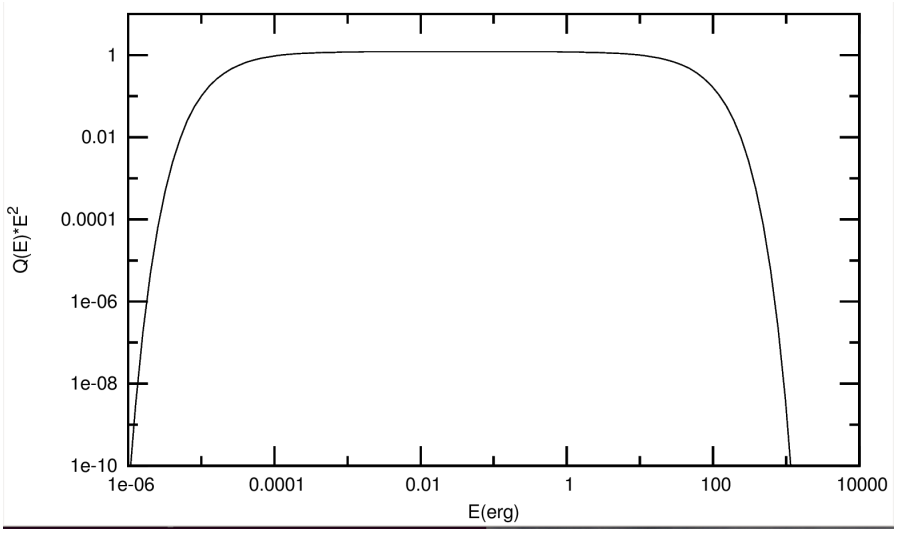

Figure 2.2: Example of SED of the NT particle population injected. The normalisation is fixed to 1 here, in the code is given by $L_{\rm inj}$, computed as in Eq. 2.7.

with $R'_{\rm a}$ being the typical size of the emitter, and $D_{\rm Bohm} = cE'/3qB'$ being the Bohm diffusion coefficient. The high-energy cutoff can be obtained by combining the different mentioned timescales:

$$E'_{\rm c,high} = \min\left(\frac{94}{\sqrt{B'\eta}}, \frac{5.6\times10^{-10}B'R'_{\rm a}}{\sqrt{\eta}}\right). \tag{2.9}$$

Once we have the spectral distribution of the injected particles we can normalise it taking into account the energy rate in the fluid frame $L_{\rm NT}$:

$$\int E'Q'(E')dE' = L'_{\rm NT}\,. \tag{2.10}$$

2.3 PARTICLE EVOLUTION ALONG THE STREAMLINES

The number of different timescales that play a role in the whole physical problem is large. However, there is a hierarchy between them that has to be respected to ensure the validity of our calculations. Any dynamically relevant time in the system has to be much larger than the time step of the hydrodynamic simulation, in order not to lose important details. Also, the typical hydrodynamical evolution timescale, set by the slowest flow (i. e.the stellar wind) has to be longer than the total amount of time it takes to the NT population to reach the steady state, $t_{\rm T}$ (set by the relativistic outflow). And finally the time steps in the particle spacial evolu-

tion code Δt_i have to be shorter than the cell-crossing time of the particles. Taking this into account, the advection time steps of this code are chosen to be $1/4$ of the shortest cell crossing time:

$$t_{\rm T} = \sum \Delta t_i = \sum \frac{1}{4} \min[\Delta x_{k,i}/v_{k,i}]\,, \tag{2.11}$$

where the subindex i relates to the time step at time t_i in the laboratory frame (LF), k to the cell, and $\Delta x_{k,i}$ being the cell length.

The computation of the evolution is done in the (relativistic) fluid frame, so in fact the advection time steps in the code are $\Delta t'_i = \Delta t_i/\Gamma$. This computation is done in three stages:

1. The first step is to inject the particles according to the $Q'(E')$ distribution computed before. After a time step $\Delta t'_i$ the SED in the cell is:

$$N'_1(E',t) = \frac{1}{|\dot{E}|}\int_{E'}^{E'_{eff}} dE^* Q'(E^*)\,, \tag{2.12}$$

   where $E'_{\rm eff} \leq E'_{\rm c,high}$ is the energy that particles had before advancing the FF time a $\Delta t'$, and is given implicitly by

$$\Delta t' = \int_{E'}^{E'_{eff}} \frac{dE^*}{|\dot{E}'(E^*)|}\,. \tag{2.13}$$

   Eq. 2.12 is the solution of the equation adapted from Ginzburg and Syrovatskii, 1964 to compute the evolution of particles in an homogeneous region,

$$\frac{\partial n'(E',\Delta t')}{\partial t'} + \frac{\partial(\dot{E}'(E')\,n(E',\Delta t'))}{\partial E'} = Q'(E')\,, \tag{2.14}$$

   where $\dot{E}'$ is the particle energy-loss rate including all the relevant losses in the FF.

2. Secondly, even if no particles are accelerated in a cell, there may be particles that had come at a previous time from the previous cell following an energy distribution $N'(E'_{\rm eff}, t_{i-1})$. These particles evolve as

$$N'_2(E',t_i) = N'(E'_{\rm eff},t_{i-1})\frac{\dot{E}'(E'_{\rm eff},t_{i-1})}{\dot{E}'(E',t_i)}\,; \tag{2.15}$$

   although under steady cooling conditions, $\dot{E}'(E'_{\rm eff},t_{i-1}) = \dot{E}'(E'_{\rm eff},t_i)$.

3. After particles are evolved in energy, flow advection has to be taken into account to include the contribution from the previous cell, and to eliminate the particles that flow to the next one. In the cell k the advection effect is

$$N'_3(E',t_i) = N'_{k-1}(E',t_i)\left(\frac{\Delta t v_{k-1}(t_i)}{\Delta x_{k-1}(t_i)}\right) - N'_k(E',t_i)\left(\frac{\Delta t v_k(t_i)}{\Delta x_k(t_i)}\right), \quad (2.16)$$

where

$$N'_k(E',t_i) = N'_1(E',t_i) + N_2(E',t_i), \quad (2.17)$$

and $(\Delta t v_k(t_i)/\Delta x_k(t_i))$ is the fraction of particles of a given cell k leaving that cell.

Now we will make a detailed description of the different cooling mechanisms that we take into account. Given that the code has been used for non-thermal electrons but not protons, we list the most relevant channels for leptons in the cases studied in this thesis.

2.3.1 *Non-thermal and adiabatic losses*

Given that the computation of the losses and the NT radiation is done in the comoving FF, every quantity (energy, angle, volume, etc.) expressed in the formulas is referred to the FF, so to be consistent with the rest of the text they should have a prime. However, in some parts we have dropped the primes for the sake of clarity, stating clearly with a note in the margin when this happens (*Fluid frame/Lab. frame*).

Fluid frame

IC LOSSES For the IC losses one has to use approximations that are valid both in the Thompson and the Klein-Nishina (KN) regimes. The most complete study on this issue was done by Khangulyan et al., 2014b and we use a prescription based on their expression for the energy losses of an electron of energy E and in a Planckian photon field of temperature T:

$$\dot{E}_{\rm IC} = \frac{2r_0^2 m_e^3 c^4 \kappa T^2}{\pi \hbar^3} \times F_{\rm ani}(t_\theta), \quad (2.18)$$

with $t_\theta = 2E(1-\cos\theta)$, θ being the scattering angle in the FF and $\kappa = (R_\star/2R)^2$ the factor of dilution of the stellar photons (R is the distance to the star).

$$F^{(0)}_{\rm ani}(u) = \frac{c_{\rm ani}\, u \log(1 + 2.16u/c_{\rm ani})}{1 + c_{\rm ani}\, u/0.822}. \quad (2.19)$$

For a value $c_{\rm ani} = 6.13$ the accuracy of this approximation is of about 1%

SYNCHROTRON LOSSES Following the description in the textbook Padmanabhan, 2001, the energy loss-rate of a charged particle with energy E inside a magnetic field is given by:

$$\dot{E}_{\rm sync} = \frac{4}{3}(\sigma_T\, c\, (E/m_e)^2 \beta^2) \times U_B, \tag{2.20}$$

where $U_B = B^2/8\pi$ is the magnetic energy density, $\beta = \sqrt{1-(E/m_e)^{-2}}$, and $\sigma_T = 8\pi/3(e^2/m_e)^2$ is the electron Thompson cross-section.

Other losses, like bremsstrahlung, are of much less importance in the systems studied here, and have therefore not been taken into account. They were implemented in the code, but we noticed that they were irrelevant and ignored them to save computational time.

ADIABATIC LOSSES The adiabatic losses are computed using the divergence of the spatial components of the flow four-velocity:

$$\dot{E}_{\rm ad}(E) = -\frac{1}{3}\nabla(\Gamma \mathrm{v}) \cdot E\,. \tag{2.21}$$

2.4 NON-THERMAL RADIATION

Lab. frame

The radiation produced by a black body with temperature T is described by the Plank Law:

$$B(\omega, T) = \frac{\hbar\omega^3}{4\pi^3 c^2} \times \frac{1}{\exp(\hbar\omega/k_{\rm B}T) - 1}, \tag{2.22}$$

where $k_{\rm B}$ is the Boltzmann constant, $\hbar$ is the reduced Planck constant, and $\hbar\omega$ is the energy of the resulting photon. As we stated before, this mechanism is not able to reach gamma-ray energies, so in our work we have focused on NT mechanisms of radiation. Here we present the most important channels of emission for a population of leptons (electrons and positrons) interacting with electromagnetic and external photon fields, but a number of other mechanisms exist if the NT population is dominated by hadrons (Bosch-Ramon and Khangulyan, 2009).

We note here that in all the cases of study, the non-thermal emitters are 3D structures, whereas the hydrodynamic simulations are 2D. Therefore, the streamlines have to be distributed in azimuthal angle around the axis of symmetry to properly account for IC, gamma-ray absorption, and

Doppler boosting for an observer looking from a certain direction. To do so, an azimuthal random position has been assigned to each streamline cell conserving the values of the r- and z-components for position and velocity (see Fig. 2.1). This transformation, only concerned with the observer direction, as long as the source of target photons is in the symmetry axis[4], it affects just the radiative part of the code; the particle energy distribution in each cell is determined by axisymmetric processes and remains unaffected.

In what follows, we designate the energy of the NT particle with E and the energy of the gamma-ray photon with ϵ. The thermal photons that serve as targets in IC scattering have an energy noted by ϵ_0.

2.4.1 *Inverse Compton*

For the computation of the IC radiation we have to take into account that, given that the source of target photons in our works is treated as a point-like emitter (a small star compared with the grid size), the IC scattering operates in the anisotropic regime (see e. g. Bogovalov and Aharonian, 2000). We have therefore adopted the expression for the spectrum of the up-scattered radiation when a mono-energetic beam of low energy photons ϵ_0 interacts with an electron of energy E, at a given angle θ relative to the initial photon beam (Aharonian, 2004):

Fluid frame

$$\frac{\mathrm{d}N(\theta,\epsilon)}{\mathrm{d}\epsilon\mathrm{d}\Omega} = \frac{3\sigma_T}{16\pi\epsilon_0 E^2} \times \left[1 + \frac{z^2}{2(1-z)} - \frac{2z}{b_\theta(1-z)} + \frac{2z^2}{\beta_\theta^2(1-z)^2}\right], \quad (2.23)$$

where $b_\theta = 2(1-\cos\theta)\epsilon_0 E$, $z = \epsilon/E$, and σ_T is the Thomson cross section.

Knowing the spectrum we can convolute it with the number density of electrons $N(E)$, assumed isotropic, and target photons $N_0(\epsilon_0)$ as follows:

$$\epsilon L_\epsilon = 4\pi c\epsilon^2 \int_{E_{min}}^{E_{max}} \mathrm{d}E \int_0^\infty \mathrm{d}\epsilon_0 \frac{\mathrm{d}N(\theta,\epsilon)}{\mathrm{d}\epsilon\mathrm{d}\Omega} N(E) N_0(\epsilon_0). \quad (2.24)$$

Lab. frame

One has to compute the density of target photons and the scattering angle in the FF. Here we present our approach to take this into account.

We consider a 2D hydrodynamic flow and a coordinate system with the z-axis being the symmetry axis. The source of target photons is located at

4 This is not the case in the system studied in Chap. 5, there we make a small adaptation of the code.

$\mathbf{r}_\star = (x_\star, y_\star, z_\star)$ and the observer is in the rz-plane, that is, the plane in which the simulation takes place, and the line of sight is parallel to

$$\mathbf{n}_{\rm obs} = (\sin\phi, 0, \cos\phi)\,. \tag{2.25}$$

A fluid element located at $\mathbf{r} = (r\cos\psi, r\sin\psi, z)$ (with r, ψ and z being cylindrical coordinates) moves with four-velocity

$$\mathbf{u} = (\Gamma, u_r\cos\psi, u_r\sin\psi, u_z) = \Gamma(1, v_r/c\cos\psi, v_r/c\sin\psi, v_z/c) \tag{2.26}$$

along the direction represented by

$$\mathbf{n}_u = \frac{(u_r\cos\psi, u_r\sin\psi, u_z)}{\sqrt{u_r^2 + u_z^2}}\,. \tag{2.27}$$

Here, $\Gamma^2 = 1 + u_r^2 + u_z^2$ is the fluid element Lorenz factor. Particles in the flow are illuminated by photons with velocity directed along

$$\mathbf{n}_{\rm ph} = \frac{(r\cos\psi - x_\star, r\sin\psi - y_\star, z - z_\star)}{\sqrt{(r\cos\psi - x_\star)^2 + (r\sin\psi - y_\star)^2 + (z - z_\star)^2}}\,. \tag{2.28}$$

Doppler boosting

Not only the IC, but for other non-thermal emission calculations as well, we have to transform the output luminosity, which is computed in the FF, to the LF. The Doppler factor is given by the following expression:

$$\delta = \frac{1}{\Gamma\,(1 - \beta\mathbf{n}_u\mathbf{n}_{\rm obs})} = \frac{1}{\Gamma - u_r\cos\psi\sin\phi - u_z\cos\phi}\,, \tag{2.29}$$

where $\beta = \sqrt{u_r^2 + u_z^2}/\Gamma$. The output luminosity (both for IC and synchrotron) is therefore corrected taking:

$$\epsilon = \delta \times \epsilon' \tag{2.30}$$

and

$$\epsilon L_\epsilon = \delta^4 \times \epsilon' L'_{\epsilon'}. \tag{2.31}$$

Stellar photon field

To compute the IC losses, we need to transform the target photon field to the FF. This transformation is determined by the Doppler factor of the stellar photons:

$$\delta_\star = \frac{1}{\Gamma\left(1 - \beta\mathbf{n}_u\mathbf{n}_{\rm ph}\right)}. \tag{2.32}$$

Scattering angle

Another important issue in the computation of anisotropic IC radiation in the relativistic regime is the computation of the scattering angle in the FF. To derive $\mathbf{n}'_{\rm obs}\mathbf{n}'_{\rm ph}$, let $k = (k, k\mathbf{n}_{\rm obs})$ be the momentum of a photon propagating towards the observer, and $\omega = (\omega, \omega\mathbf{n}_{\rm ph})$ the momentum of a photon emitted by the star towards the fluid element. Since the scalar products (ku) and (ωu) are Lorentz invariant and the four-velocity of the fluid element in the FF is $u' = (1, 0)$, we obtain that

$$\omega' = \omega(\Gamma - \sqrt{u_r^2 + u_z^2}\mathbf{n}_u\mathbf{n}_{\rm ph}) = \omega\delta_\star^{-1}\,, \tag{2.33}$$

and

$$k' = k(\Gamma - \sqrt{u_r^2 + u_z^2}\mathbf{n}_u\mathbf{n}_{\rm obs}) = k\delta^{-1}\,. \tag{2.34}$$

Since $(k\omega)$ is an invariant,

$$k\omega(1 - \mathbf{n}_{\rm obs}\mathbf{n}_{\rm ph}) = k'\omega'(1 - \mathbf{n}'_{\rm obs}\mathbf{n}'_{\rm ph})\,, \tag{2.35}$$

and consequently,

$$\mathbf{n}'_{\rm obs}\mathbf{n}'_{\rm ph} = 1 - (1 - \mathbf{n}_{\rm obs}\mathbf{n}_{\rm ph})\delta\cdot\delta_\star\,. \tag{2.36}$$

2.4.2 *Synchrotron*

Fluid frame

To compute the synchrotron radiation we follow the steps described in the third chapter of Pacholczyk, 1970, where both the photon energies and the particle energies are given in units of $m_e c^2$. For a given photon energy ϵ, the emission coefficient $j(\epsilon)$ is given by:

$$j(\epsilon) = c_3 B \sin\theta \int_{E_{\rm min}}^{E_{\rm max}} N(E)F(x)\mathrm{d}E. \tag{2.37}$$

In this equation, $c_3 = \sqrt{3}e^3/4\pi mc^2$ and θ is the angle between the magnetic field B and the direction towards the observer. We consider the magnetic field inside the cell to be *isotropized* for simplicity, and we make the following approximation: $B \to B\sqrt{2/3}$. Also, we know that the motion of the particles inside the cell is also isotropic in the FF, so we do not have to consider every direction, and the integral over the solid angle reduces to a pre-factor 4π before the integral.

With regards to the function $F(x)$, firstly we define x as:

$$x = \epsilon/\epsilon_c, \text{where } \epsilon_c = \frac{c_1 B E^2}{h}, \tag{2.38}$$

where ϵ_c is the critical energy of the process, $c_1 = 3e/4\pi m_e^3 c^5$, and h is the Planck constant.

The function $F(x)$ is defined through an integral of the $K_{5/3}(z)$ Bessel function, but we take an approximation from Aharonian, 2004 valid in the interval $0.1 < x < 10$:

$$F(x) = \int_x^\infty K_{5/3}(z)\,\mathrm{d}z \simeq 1.85\, x^{1/3} e^{-x}. \tag{2.39}$$

Finally, the expression of ϵL_ϵ for the synchrotron emission can be written as:

$$\epsilon L_\epsilon = \epsilon \frac{4\pi \cdot c_3 \cdot B\sqrt{2/3}}{h} \int_0^\infty N(E) F(x)\,\mathrm{d}E. \tag{2.40}$$

As we mentioned in the case of the IC emission, this expression is valid in the comoving FF and we have to transform the output to the LF, multiplying $\epsilon = \delta \cdot \epsilon'$ and $\epsilon L_\epsilon = \delta^4 \cdot \epsilon' L'_{\epsilon'}$. *Lab. frame*

2.4.3 *Absorption of gamma rays through pair creation*

The photons coming from the source would have sometimes to go through an external, low energy photon field, e. g. from a companion/nearby star. Given the high energy of the radiation, some photon-photon collisions can produce electron-positron pairs. This process would absorb part of the emission, reducing the luminosity at certain energies. For the process $\gamma + \gamma \rightarrow e^- + e^+$ the total cross section (Gould and Schréder, 1967) is:

$$\sigma_{\text{pair}} = \frac{\pi}{2} r_0^2 (1 - \beta_\text{e}^2) \left[(3 - \beta_\text{e}^4) \ln \frac{1 + \beta_\text{e}}{1 - \beta_\text{e}} - 2\beta_\text{e}(2 - \beta_\text{e}^2) \right], \tag{2.41}$$

where $r_0 = e^2/m_e c^2$ is the classical electron radius and β_e is the electron (and positron) velocity in the centre-of-mass frame in c units. If we consider a high-energy photon (ϵ) and a low energy one (ϵ_0) colliding with an angle θ, we can use the invariance of the total 4-momentum of the particles to get an expression for β_e:

$$\beta_\text{e} = \sqrt{1 - 1/s}, \tag{2.42}$$

with

$$s = \frac{\epsilon \cdot \epsilon_0}{2m_e^2 c^4}(1 - \cos\theta). \tag{2.43}$$

So the threshold for pair production to occur is (in the most extreme case: a head-on collision) $\epsilon \cdot \epsilon_0 = m_e^2 c^4$, which is equivalent to impose $s > 1$.

Now we just have to compute the optical depth τ associated with this process and correct the luminosity by $\epsilon L_\epsilon = \epsilon L_{\epsilon,0} \times e^{-\tau}$. The computation of τ has been done as follows:

$$\tau = \int_0^{x_{\max}} \mathrm{d}x \int_{\epsilon_{0,\min}}^{\epsilon_{0,\max}} \mathrm{d}\epsilon_0 \, n_0(\epsilon_0) P(\epsilon, \epsilon_0, \theta), \tag{2.44}$$

where here P is the probability of interaction, given by $P(\epsilon, \epsilon_0, \theta) = \sigma_{\mathrm{pair}}(1 - \cos\theta)$.

Part II

EXTRAGALACTIC SOURCES

This part of the thesis is the result of the work published in the article *Coupling hydrodynamics and radiation calculations for star-jet interactions in active galactic nuclei*, V. M. de la Cita et *al.* A&A 591, A15 (2016)

3

STAR-JET INTERACTIONS IN AGN

3.1 INTRODUCTION

The winds and atmospheres of stars have been studied as an important factor in the propagation, stability, matter content, and potential disruption of the jets of AGN (e.g. Komissarov, 1994; Bowman et al., 1996; Hubbard and Blackman, 2006; Bosch-Ramon et al., 2012a; Perucho et al., 2014). Furthermore, the interaction of jets with stellar atmospheres or winds have also been suggested to be responsible of the radiation of NT emission, in both blazar and non-blazar AGN, and in the form of both transient and persistent radiation (e.g. Bednarek and Protheroe, 1997; Barkov et al., 2010, 2012b,a; Khangulyan et al., 2013; Bosch-Ramon et al., 2012a; Araudo et al., 2013; Bosch-Ramon, 2015; Bednarek and Banasiński, 2015). Indeed, there might already be direct observational evidence of such an interaction (e.g. Hardcastle et al., 2003; Müller et al., 2014), and some authors have pointed out that high-energy phenomena observed in some AGN might be interpreted in the context of jet-star interactions (e.g. Barkov et al., 2010, 2012b,a; Khangulyan et al., 2013). The actual extent of the dynamical and radiative impact of these interactions is however still unknown.

In the jet-star interaction scenario, stars are expected to cross AGN jets at different distances from the jet base, producing shocks that can transfer kinetic energy to non-thermal particles. In the case of highly magnetized jets, these would present different mechanisms to transfer jet energy, now in the magnetic field instead of being in kinetic form, to non-thermal particles (see, e.g. Bosch-Ramon, 2012, and references therein). Electric fields produced by jet-stretched magnetic field lines around an obstacle could also accelerate particles (e.g. Jones et al., 1996).

In the inner-most jet regions, stars are expected to move fast and the jet is narrower, which means that only a few stars can interact with the jet at a time. Here the emission might be released during relatively short events that are triggered by high-inertia targets, such as the external weakly bound layers of evolved giants (e.g. Barkov et al., 2010), or stars with very high mass-loss (e.g. Araudo et al., 2013). Persistent emission might also take place far from the jet base, as the jet propagates through the inner-most kpc regions of the galaxy, and even farther out (Araudo et al., 2013; Bednarek and Banasiński, 2015). In all these situations, several ingredients are required to accurately estimate the interaction duration, rate, effect on the jet properties, and related radiation: a proper characterization of the stellar populations and their spatial distribution, both galaxy-type dependent, and a detailed description of the physics of the jet-star interaction and the associated non-thermal processes. An approximate study by Bosch-Ramon, 2015 combining both hydrodynamics and radiation estimates was carried out, the result of which was that the emission from individual jet-star interactions may be significantly higher than previously thought.

A proper understanding of the AGN jet radiation and its underlying physics needs an accurate characterization of the emission produced in stars interacting with AGN jets. To proceed in this direction, we make use of the tools developed throughout the thesis and described in Chap. 2. We combine RHD simulations and radiation calculations, assuming no dynamical feedback from non-thermal processes (a rather good assumption in the cases studied in this chapter), to characterize the emission produced in the shocked jet region that forms when the jet flow is stopped by a stellar wind. First we simulate the interaction of a stellar wind and a relativistic jet until the steady-state is reached. Then, the obtained hydrodynamical information is used to characterize the injection of non-thermal particles, their propagation, and emission. As matter and radiation densities are generally low unless interactions occur close to the jet base (see Barkov et al., 2012b; Khangulyan et al., 2013), hadronic processes are

not expected to be relevant. Thus, the emitting particles are assumed to be leptons here, which might be electrons for a proton-dominated jet, or electrons and positrons ($e^{\pm}$) for a $e^{\pm}$-dominated jet. We consider a situation in which a star of relatively high mass-loss and luminosity, such as a red giant or a moderately early star, interacts with a jet of intermediate power. The results can be scaled, which allows deriving broader conclusions. As in the rest of this thesis, primed quantities are in the FF.

3.2 HYDRODYNAMICS

3.2.1 *Simulated cases*

The hydrodynamic simulations performed for this work were done by our collaborators as described in 2.1, here we present the specific details to give context to our NT calculations.

We assumed a collisionless adiabatic and relativistic ideal gas with a dynamically negligible magnetic field. For simplicity, the gas has one particle species with a constant relativistic adiabatic index $\hat{\gamma}$ of $4/3$ for both the jet and the stellar wind material. The physical size of the domain is $r \in [0, l_r]$ with $l_r = 2 \times 10^{15}$ cm, and $z \in [0, l_z]$ with $l_z = 1.5 \times 10^{15}$ cm. The total number of cells is 400 and 300 in the radial and axial directions, respectively. This resolution was chosen to have enough numerical dissipation to avoid a growth of instabilities that is fast enough to prevent the formation of a quasi-steady state (see Sect. 3.2.2). All these parameters are summarized in Table 3.1.

The star was located at $(r_0, z_0) = (0, 0.3 \times 10^{15})$ cm, and its spherical wind was injected through a region with radius $r_{\rm in} = 7 \times 10^{13}$ cm (14 cells), small enough not to be affected by the shock terminating this wind. The jet was injected at the bottom boundary of the grid. The jet streamlines were approximated as parallel instead of radially extending from the jet origin because the scales of the simulation were much smaller than the height of the jet at which the interaction takes place. The upper and right boundaries of the grid were set to outflow, while the left boundary was set to reflection.

The physical parameters of the jet, which is in an inflow condition at the bottom of the computational grid, are the total jet power within the grid, $L_0 \approx 4 \times 10^{37}$ erg s^{-1} ($\sim 10^{44}$ erg s^{-1} for a 1 pc jet radius), the Lorentz factor $\Gamma_0 = 1/\sqrt{1 - (v_0/c)^2} = 10$, with $v_0 = v_z = 0.995\ c$ and $v_r = 0$, and the

Parameter	Jet-stellar wind simulation
$\hat{\gamma}$	$4/3$
l_r	2×10^{15} cm
l_z	1.5×10^{15} cm
n_r	400
n_z	300

Table 3.1: Simulation parameters. Adiabatic index $\hat{\gamma}$, physical r-grid size l_r, physical z-grid size l_z, number of cells in the r-axis n_r, and number of cells in the z-axis n_z.

specific internal energy $\epsilon_0 = 9\times10^{18}$ erg g^{-1}. The jet power is computed as

$$L_0 = \pi l_r^2 \Gamma_0 \rho_0 (h_0\Gamma_0 - 1)c^2 v_0\,, \tag{3.1}$$

where $\rho_0 = 1.24\times10^{-27}$ g cm^{-3} is the jet density, $p_0 = (\hat{\gamma}-1)\rho_0\epsilon_0$ its pressure, and $h_0 = 1 + \frac{\epsilon_0}{c^2} + \frac{p_0}{\rho_0 c^2}$ its specific enthalpy.

The stellar wind is a spherical inflow condition imposed at 7×10^{13} cm from the star centre. The wind physical parameters at injection are the mass-loss rate $\dot{M} = 10^{-9}$ M$_\odot$ yr^{-1}, the radial velocity $v_{\rm sw} = 2\times10^8$ cm s^{-1}, and the specific internal energy $\epsilon_{\rm sw} = 9\times10^{13}$ erg g^{-1}. The derived stellar wind density at injection is $\rho_{\rm sw} \approx 5.2\times10^{-21}$ g cm^{-3}. The stellar wind was taken to be homogeneous, meaning that it is not clumpy, and since it is supersonic, its density profile from the injection radius up to its termination is $\propto 1/R^2$, with R being the distance to the star centre. The wind properties correspond to those of a high-mass star with a modest mass-loss rate. The thrust of this wind, $\dot{M}v_{\rm sw} \approx 1.3\times10^{25}$ g cm s^{-2}, would correspond to that of a red giant, although if a red giant wind had been simulated, the velocity would have been an order of magnitude lower (with $\dot{M}$ scaling accordingly), making the simulation much longer. However, since the relation between the jet momentum flux and the wind thrust determines to first order the shape of the interaction region, a lighter wind of equal thrust can be used to reduce the computational costs.

The star was assumed to be at rest. This is a reasonable assumption as long as the stellar velocity is much lower than $v_{\rm sw}$. Otherwise, the jet-wind interaction geometry will strongly depart from axisymmetry, making the results obtained here less realistic. The Keplerian velocity for a 10^8 M$_\odot$ central black hole at a distance of 10 pc is $v_{\rm K} \approx 2\times10^7$ cm s^{-1}, a 10% of

Parameter	Jet	Stellar wind
ρ	1.24×10^{-27} g cm^{-3}	5.12×10^{-21} g cm^{-3}
ϵ	9×10^{18} erg g^{-1}	9×10^{13} erg g^{-1}
v	0.995 c	2000 km s^{-1}

Table 3.2: Jet and stellar wind physical parameters. Density ρ, specific internal energy ϵ, and velocity v at $z = 1\times10^{13}$ cm for the jet (boundary condition), at a distance $r_{\rm in} \leq 7\times10^{13}$ cm with respect to the star centre at $(r_0, z_0) = (0, 0.3\times10^{15})$ cm (boundary condition).

the adopted $v_{\rm sw}$-value. We considered this $v_{\rm K}$-value low enough at this stage, but a caveat must be made: for a more realistic red giant wind, $v_{\rm K}$ would become of the order of $v_{\rm sw}$, and the star motion would then have to be taken into account. This requires 3D simulations, however, which are much more computationally expensive than the axisymmetric simulations carried out here, which are meant as a first step in coupling radiation and hydrodynamics studying jet-star interactions. Finally we note that in general the jet-crossing time will be much longer than the simulated times (given in Sect. 3.2.2).

The grid was initially filled with the jet properties except within the stellar wind injection region, which was filled with the stellar wind properties. The jet and stellar wind physical parameters are summarized in Table 3.2.

The jet momentum flux (thermal plus kinetic pressure) at the bottom of the computational grid is

$$F_0 = \rho_0 \Gamma_0^2 v_0^2 h_0 + p_0\,, \tag{3.2}$$

and the stellar wind momentum flux at a distance R is

$$F_{\rm sw} = \frac{\dot{M} v_{\rm sw}}{S_{\rm sw}} + p_{\rm sw}\,, \tag{3.3}$$

where $S_{\rm sw} = 4\pi R^2$, and $p_{\rm sw} = (\hat{\gamma} - 1)\,\rho_{\rm sw}\epsilon_{\rm sw}$ is the pressure of the stellar wind. Equations (3.2) and (3.3) allow us to set the point where the jet and the stellar wind momentum fluxes are equal, at $R_{\rm CD} = 0.1\times10^{15}$ cm from the star centre, locating the contact discontinuity (CD) on the simulation axis. This corresponds to a position $z_{\rm CD} = z_0 - R_{\rm CD} = 0.2\times10^{15}$ cm with respect to the bottom of the grid ($z = 0$).

3.2.2 *Results*

3.2.2.1 *Steady-state*

Figure 3.1 shows the density map and the trajectories of the computed streamlines for the jet-stellar wind simulation when a (quasi-) steady-state is reached at $t = 3.3 \times 10^7$ s. The dynamical timescale of the problem is determined by the stellar wind, which is $\sim l_z / v_{\rm sw} = 7.5 \times 10^6$ s, as it carries more mass and $v_{\rm sw} \ll v_0$. Thus, the t-value reached seems appropriate. The two shocks formed are bow-shaped towards the star, which has a much lower thrust than the jet within the grid. The CD in the simulation is at $z_{\rm CD}^{\rm num} \sim 0.2 \times 10^{15}$ cm, as obtained analytically in Sect. 3.2.1. Figure 3.2 illustrates the re-acceleration of the shocked jet material as it is advected upwards. This feature has a strong effect on the radiation because Doppler-boosting effects cannot be neglected. This is also shown in Fig. 3.3, where the Doppler-boosting enhancement of the emission in the jet direction is presented.

3.2.2.2 *Instability growth*

The simulation reaches a quasi-stationary numerical solution, with the shocked flow structure in a metastable state. There are recurrent perturbations coming from the numerical, spatial, and temporal discretization that grow as a result of the developing instabilities. Although the perturbations are of numerical origin, they can be considered to mimic the irregularities expected in real flows because they are hardly completely smooth or laminar. The double-shock structure presents variations in time caused by irregularities originated in the CD that grow as they are advected with the flow. The growth of these irregularities is mostly linked to the Kelvin-Helmholtz instability (KHI) because the velocity of the shocked jet flow along the CD grows very quickly from the simulation axis, which leads to a strong velocity difference with respect to the shocked wind; if the velocity of the CD perpendicular to itself were not zero, the Rayleigh-Taylor instability (RTI) would develop as well (Chandrasekhar, 1961). In our case, the average velocity of the CD was zero (although there are small fluctuations in its position). The KHI is thus the dominant source of perturbation growth in the CD close and far from the axis.

The development of instabilities has imposed a limitation on the simulation parameters. At the onset of the simulation, instabilities develop in the interacting flows, with the related growing irregularities being ad-

vected out of the grid and leaving the quasi-steady interaction structure described above. For lighter jets, heavier winds, or a higher resolution, the development and growth of the perturbations are enhanced and produce smaller and denser fragments of stellar wind able to penetrate deeper into the jet flow and generate shocks in the entire computational domain. This is caused by instability growth, which causes small wind structures to quickly develop and propagate within the grid, triggering shocks in the jet flow. This can lead to a grid that is partially occupied by hot material that reaches the grid boundaries with subsonic velocities. This renders the simulation results unrealistic because waves develop in the grid boundaries and bounce back, which affects the flow dynamics inside the grid. In addition, since the flow is subsonic at the grid boundaries, the subsonic flow is evacuated too slowly and accumulates and can potentially end up filling the whole grid. This could be avoided by a larger grid, although if a higher resolution were used, the disruptive effect of instabilities (see e.g. Perucho et al., 2004) would be enhanced, pushing the grid size requirements even further.

Strong sensitivity to resolution and flow density contrast was already faced in previous similar axisymmetric simulations. The fast growth of perturbations close to the axis was seen for instance in Paredes-Fortuny et al., 2015 in the context of a relativistic pulsar wind interacting with a non-relativistic stellar wind. It was noted that this effect might have a partially numerical origin in the coordinate singularity plus a reflective boundary at $r = 0$. However, a similarly fast perturbation growth also appeared in relativistic 2D simulations for that scenario (Bosch-Ramon et al., 2012b; Lamberts et al., 2013) in planar geometry, which shows that the perturbations were not only due to an artefact of the conditions at $r = 0$. For the jet-stellar wind scenario, we ran low-resolution 3D simulations (not presented here) focusing on the region close to the star. We found that the shocked structure was also prone to develop instabilities, although the small grid size prevented a deeper analysis.

3.2.2.3 *Perturbed state*

Although the fast growth of the instabilities may be partially linked to the axisymmetry of the simulations, judging from the discussion above, this growth seems to be a physical effect to a large extent. It is thus worth considering some instance of the interaction region when it is affected by a strong perturbation before reaching the steady-state. Such an instance is shown in the lower pannel in Fig. 3.1, which presents the density map and

trajectories of the computed streamlines at $t = 3.7 \times 10^6$ s. As seen in the figure, the perturbations deeply penetrate the jet, increasing the size of the interaction region and strongly modifying the streamline trajectories. This is an example of how important physical instability growth might be for the effective size of the stellar target the jet meets.

In the corner of the map in lower pannel of Fig. 3.1 where the top and right boundaries join, a reflection shock is visible in a small region. This reflection shock is an example of the presence of subsonic flow at the boundaries. However, this shock only affects a minor region of the simulation, even accounting for the cylindrical symmetry, so we have allowed for the presence of this small artefact. At our level of resolution, our simulation did reach a physically realistic steady-state (with the mentioned small fluctuations in the CD), although the hydrodynamical solution shown in the lower pannel of Fig. 3.1 does not correspond to steady-state. Nevertheless, as radiation is computed from the shocked jet material with a dynamical timescale $\sim l_z/c \ll l_z/v_{\rm sw}$, we can assume that the flow shown in Fig. 3.1, lower panel, is in a pseudo-steady state for emission computation purposes.

When characterizing the non-thermal emitters through streamlines, we discarded the lines that presented mixing between jet and stellar wind fluids that exceeded 50% in at least one cell of the streamline for the jet-star interactions in steady-state. The surface of any discarded streamline was added to the line immediate adjacent along the radial coordinate. This compensates for the lack of lines close to the jet axis because the hydrodynamical conditions are relatively similar there. On the other hand, the streamlines of the jet-star interaction in the perturbed state were computed regardless of the level of mixing because many lines were numerically affected. For this case, we just removed the segments of the streamlines that were affected by a mixing level > 50%.

3.3 RADIATION

We applied the radiative code described in Chap. 2 in conjunction with the RHD results of Sect. 3.2 to compute the radiation in the two studied scenarios: the star-jet interaction in the steady and the perturbed states. We let three parameters vary: the angle between the jet axis and the line of sight, ϕ; the initial ratio of Poynting-to-matter energy flux (see Eq. 2.5), χ_B; and the height in the jet with respect to the jet base, where the jet-star interaction takes place, $z_{\rm int}$.The values considered for these parameters

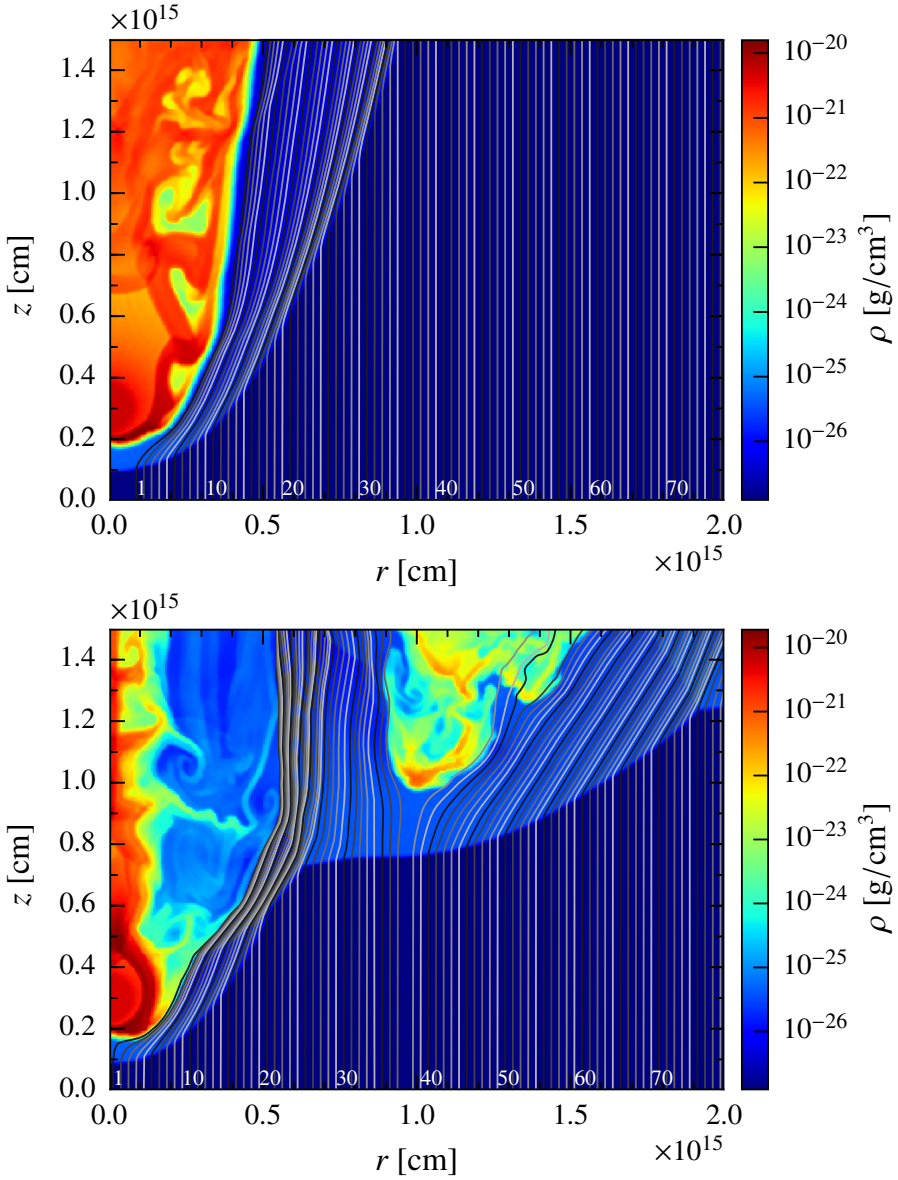

Figure 3.1: Upper pannel: Density distribution by colour at time $t = 3.3 \times 10^7$ s for the star-jet interaction in its steady configuration. Lower pannel: Density distribution by colour at time $t = 3.7 \times 10^6$ s for the star-jet interaction in a perturbed state. In both cases the star is located at $(r_0, z_0) = (0, 3{\times}10^{14})$ cm and the jet is injected at $z = 1{\times}10^{13}$ cm. The grey lines show the computed streamline trajectories; the numbers and the grey scale are added just for visualization.

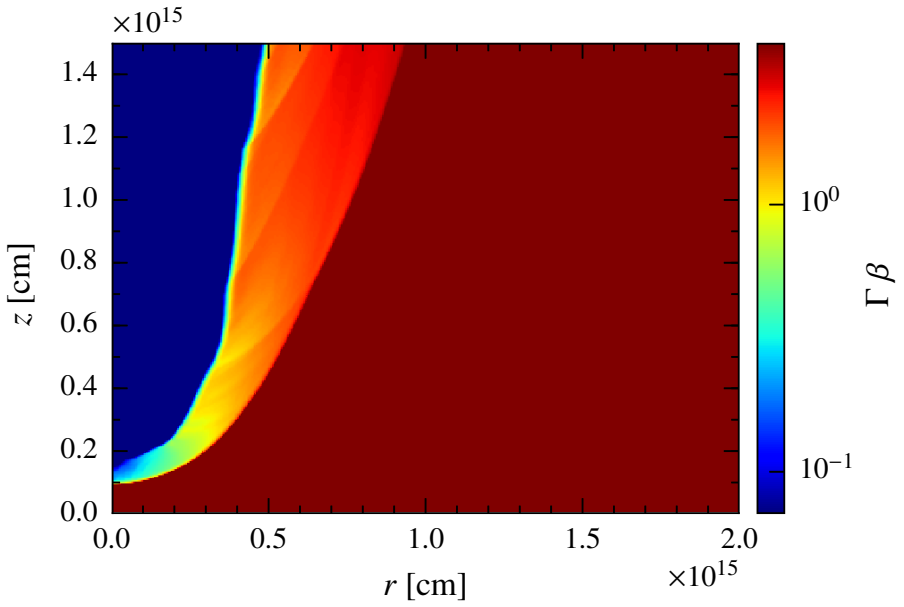

Figure 3.2: Distribution by colour of the module of the spatial component of the four-velocity at time $t = 3.3 \times 10^7$ s for the star-jet interaction in its steady configuration.

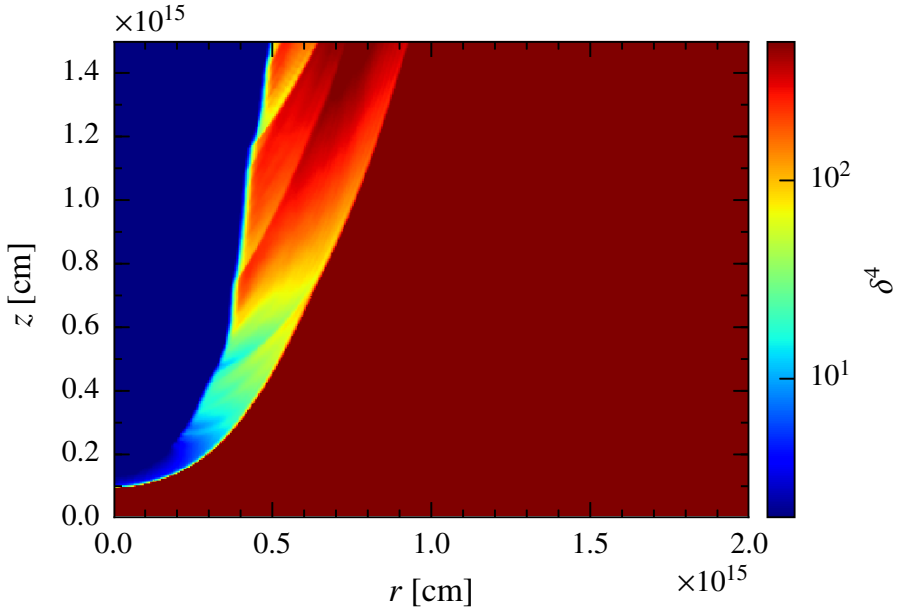

Figure 3.3: Distribution by colour of the Doppler-boosting enhancement of the emission, as seen from the top, at time $t = 3.3 \times 10^7$ s for the star-jet interaction in its steady configuration.

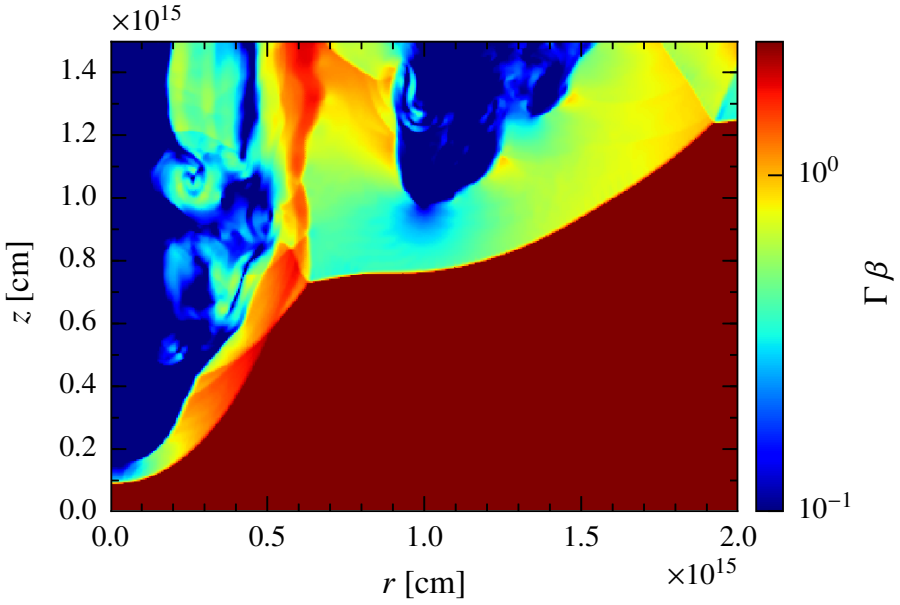

Figure 3.4: Distribution by colour of the module of the spatial component of the four-velocity at time $t = 3.7 \times 10^6$ s for the star-jet interaction in a perturbed state.

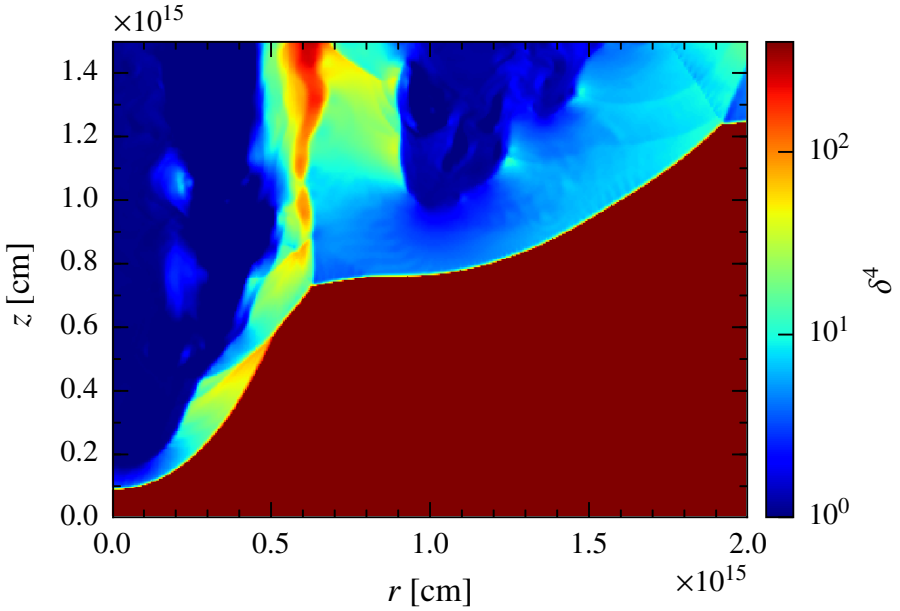

Figure 3.5: Distribution by colour of the Doppler boosting enhancement of the emission, as seen from the top, at time $t = 3.7 \times 10^6$ s, for the star-jet interaction in a perturbed state.

Parameter	Set of values
Jet observation angle ϕ	0, 45, 90, 135°
Fraction χ_B	$10^{-4}, 10^{-1}$
Height $z_{\rm int}$	1, 10, 100, 1000 pc

Table 3.3: Set of parameters for the two scenarios considered.

are summarized in Table 4.2. We recall that the simulations were computed with a purely RHD code, meaning that the magnetic field is not dynamically relevant and only high enough to allow the plasma to behave as a fluid. However, we adopted $\chi_B = 10^{-1}$ in some cases, which is still small enough to avoid violating the low-B condition, to have an example of a relatively high B-case.

3.3.1 *Scalability of the results*

Throughout this chapter, the jet power, L_0, opening angle (taken $\sim 1/\Gamma_0$, as in Bosch-Ramon, 2015, see references therein), and wind thrust, $\dot{M}v_{\rm sw}$, were fixed to the following reference values: $\approx 10^{44}$ erg s^{-1}, 0.1 rad, and 1.3×10^{25} dyn, respectively. The star temperature and luminosity were also fixed to those of a red giant. However, the obtained results for the different values of ϕ, χ_B, and $z_{\rm int}$ explored can be easily generalized if Γ_0 and T_* are fixed, and L_* is approximated as $\sim \dot{M}v_{\rm sw}c$ (Bosch-Ramon, 2015). An additional assumption to perform the generalization is that the radiation on the particle energy distribution (e.g. through synchrotron self-Compton) or the radiation itself (e.g. through internal pair creation) do not significantly interact. Under these conditions, the SEDs and mapped quantities presented below can be scaled as follows:

(i) The spectrum does not change if the escape-to-radiative timescale ratio,

$$t_{\rm esc}/t_{\rm rad} \propto \sqrt{\dot{M}v_{\rm sw}L_0}/z_{\rm int}\,,$$

is constant, where $t_{\rm rad} \propto R_{\rm CD}^2/\dot{M}v_{\rm sw}$ and $t_{\rm esc} \propto R_{\rm CD}$. The quantity $t_{\rm rad}$ typically depends on the particle energy, which means that the timescale ratio has to be computed by fixing this energy to some particular value. The quantity $t_{\rm esc}$ would correspond to the typical timescale required for particles to escape the emitting region (see Bosch-Ramon, 2015).

(ii) The SED normalization changes as (Bosch-Ramon, 2015)

$$\propto (R_{\rm CD}/R_{\rm j})^2 L_0 \propto \dot{M} v_{\rm sw}\,,$$

where $R_{\rm j}$ is the jet radius. In the adiabatic regime of the emitter, the SED normalization is also $\propto t_{\rm esc}/t_{\rm rad}$.

(iii) Thus, in the adiabatic regime, the non-thermal luminosity, either synchrotron or IC, can be simply scaled as

$$\propto (\dot{M} v_{\rm sw})^{3/2} L_0^{1/2}/z_{\rm int}\,,$$

which is the product of the dependences stated in (ii).

These relations are more refined versions than, but based on, those presented in Eqs. (6) and (9) in Bosch-Ramon, 2015.

For the jet Lorentz factor Γ_0, Bosch-Ramon, 2015 indicated that the normalization of the observer luminosity should approximately scale as $\propto \Gamma_0^2$. However, this is strictly valid in the ultra-relativistic regime, and far from the shock and/or under fast expansion of the streamlines; the scaling is less sensitive to Γ_0 for relatively slow expansion and in the simulated region.

3.3.2 *Spectral energy distributions and radiation maps*

Figures 3.6 and 3.7 show the observer synchrotron and IC SEDs for the star-jet interaction in the steady-state, for $\chi_B = 10^{-4}$ and 10^{-1}, $\phi = 0° - 135°$, and $z_{\rm int} = 10$ pc. For high magnetization, synchrotron emission strongly dominates and reaches much higher photon energies. However, even in this case, most of the particle energy distribution is dominated by advection escape, and therefore the synchrotron and IC SED shapes do not depend significantly on χ_B. The advection escape dominance also implies that the non-thermal particle population behaves as an adiabatic flow and that the ratio of non-thermal-to-thermal energy will approximately keep constant along the streamlines. As seen in the figures, the emission is significantly boosted for the jet on axis. Interestingly, for $\chi_B = 10^{-1}$ the synchrotron SEDs for high ϕ-values present softer spectra because particles coming from the more Doppler-boosted outer lines (thus beamed away for high ϕ) have higher maximum photon energies. This effect is not as clearly seen in the IC SED because the softening of the SED is already strong as a result of the KN effect in the cross section.

In Fig. 3.8 the observer synchrotron and the IC SED are shown for different values of $z_{\rm int}$ from 1 to 1000 pc, and for $\chi_B = 10^{-4}$, and $\phi = 0°$. It

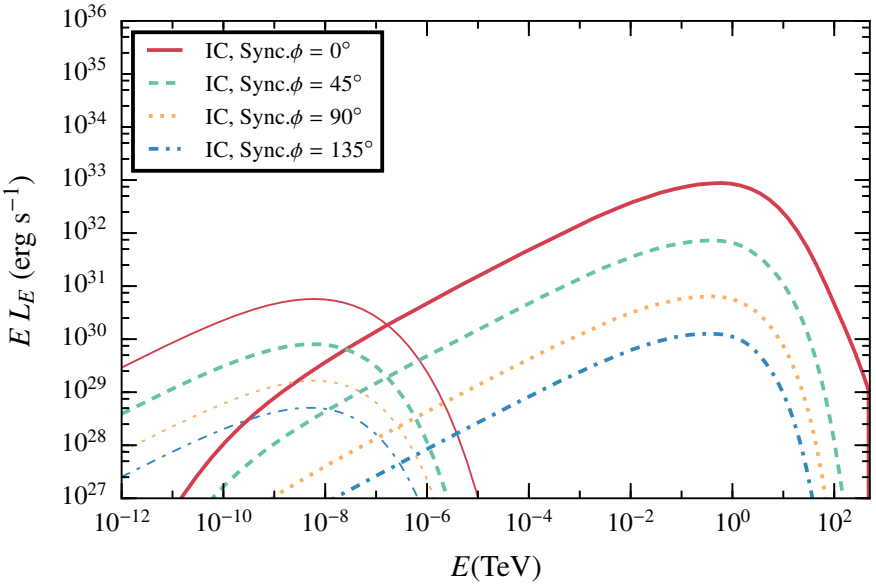

Figure 3.6: Synchrotron (thin) and IC (thick line) SEDs for the jet-star interaction in the steady-state, taking $z_{\rm int} = 10$ pc, $\chi_B = 10^{-4}$, and for $\phi = 0°$, 45°, 90° and 135°.

is clear from the figure that the closer to the jet base, the higher the ratio of radiative versus advection energy loss, which as mentioned is $\propto 1/z_{\rm int}$.

Figures 3.9 and 3.10 presents the distribution of the bolometric luminosity per cell in the rz-plane for both synchrotron and IC, taking $\chi_B = 10^{-4}$, $z_{\rm int} = 10$ pc, and $\phi = 0°$. We note that because of the azimuthal geometry, the computational cells correspond to annular physical regions. The maps show that the synchrotron emission is more widely distributed than IC emission. This is because the IC target photon field is concentrated towards the star.

Finally, in Figs. 3.11 and 3.12 we show the contribution of the different lines for $z_{\rm int} = 10$ pc, $\chi_B = 10^{-4}$, and $\phi = 0°$, to the observer synchrotron and IC SED, and total energy distribution in the LF, respectively. The contribution to the emission varies substantially between different streamlines, depending on the non-thermal particle content, the role of adiabatic cooling or heating along the lines, the flow velocity and direction, the local magnetic field, and the relative position with respect to the source of target photons.

Figure 3.13 shows the observer synchrotron and IC SEDs for the star-jet interaction in the perturbed state, for $\chi_B = 10^{-4}$ and 10^{-1}, $\phi = 0° - 135°$, and $z_{\rm int} = 10$ pc. Figures 3.14 and 3.15 present the distribution in the rz-

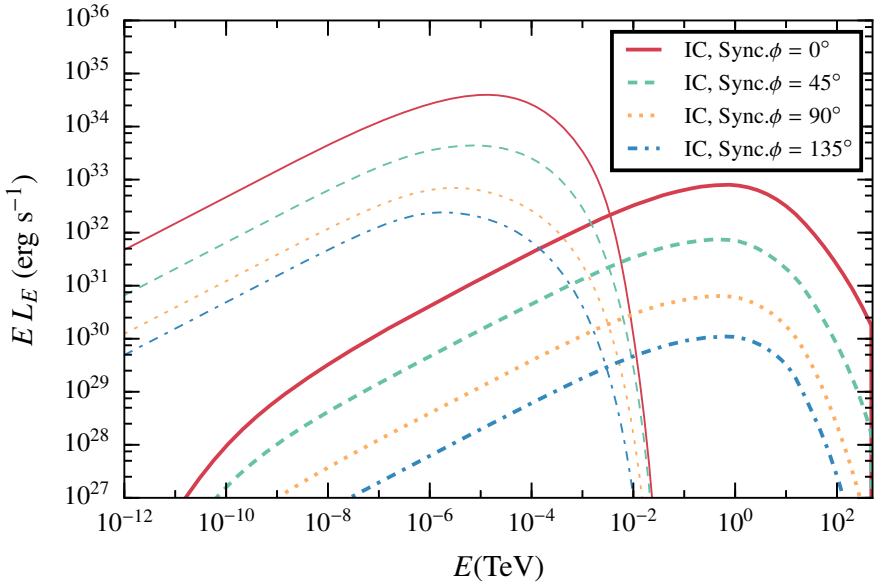

Figure 3.7: Same as in Fig. 3.6, but for $\chi_B = 10^{-1}$.

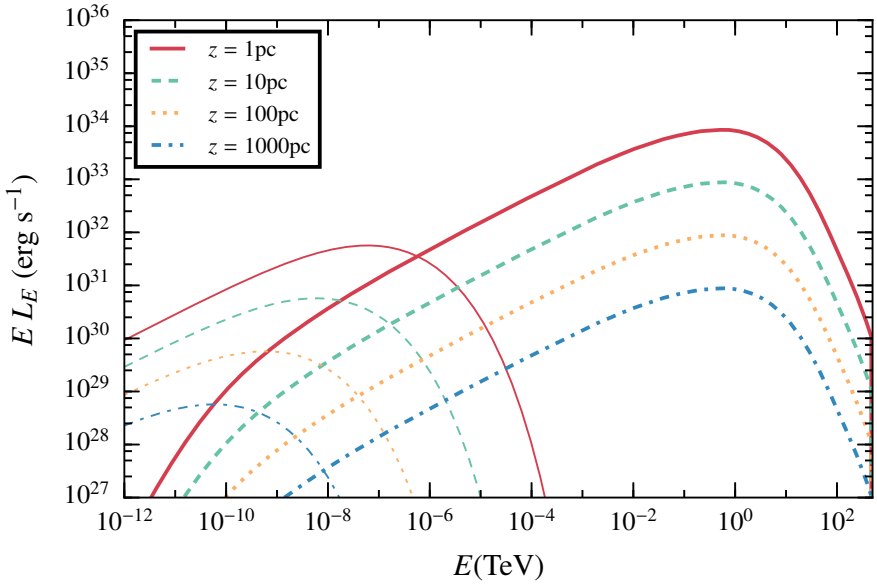

Figure 3.8: Synchrotron (thin) and IC (thick line) SEDs for the jet-star interaction in the steady-state, taking $\phi = 0°$, $\chi_B = 10^{-4}$, and for $z_{\rm int} = 1$, 10, 100 and 1000 pc.

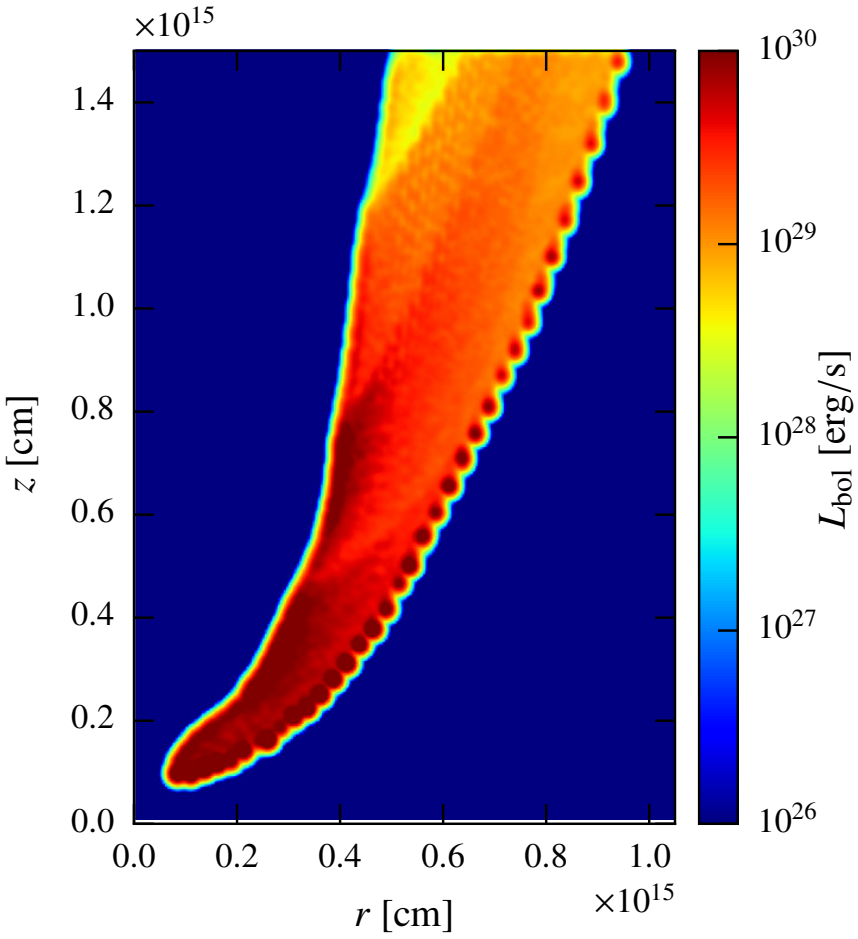

Figure 3.9: Map in the rz-plane of the distribution of IC, bolometric luminosity per cell, for the jet-star interaction in the steady-state. The adopted parameters are $\phi = 0$, $\chi_B = 10^{-4}$ and $z = 10$ pc.

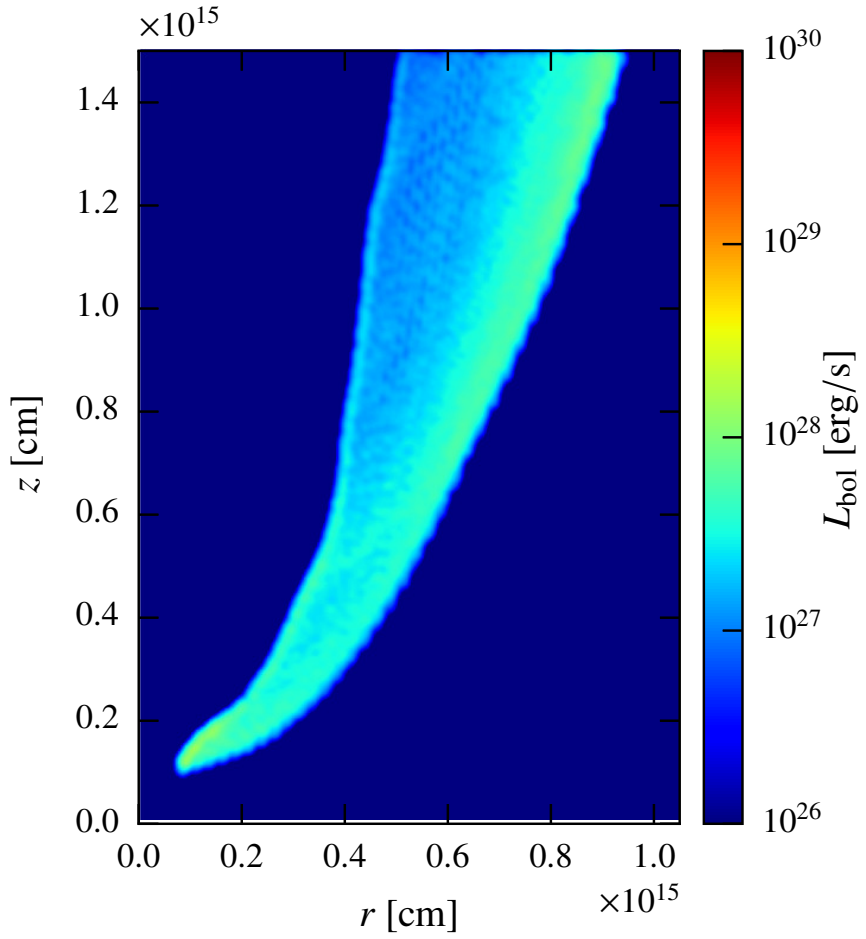

Figure 3.10: Map in the rz-plane of the distribution of synchrotron, bolometric luminosity per cell, for the jet-star interaction in the steady-state. The adopted parameters are $\phi = 0$, $\chi_B = 10^{-4}$ and $z = 10$ pc.

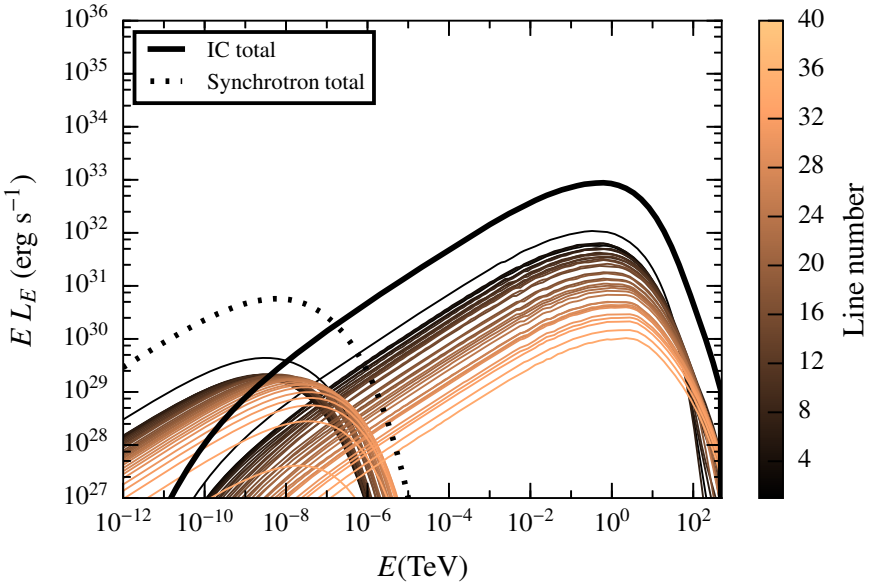

Figure 3.11: Synchrotron and IC SEDs for the different streamlines (thin brown lines), and the sum of all of them (thick black line, dotted for synchrotron) for the jet-star interaction in the steady-state and $z_{\rm int} = 10$ pc, $\chi_B = 10^{-4}$ and $\phi = 0°$.

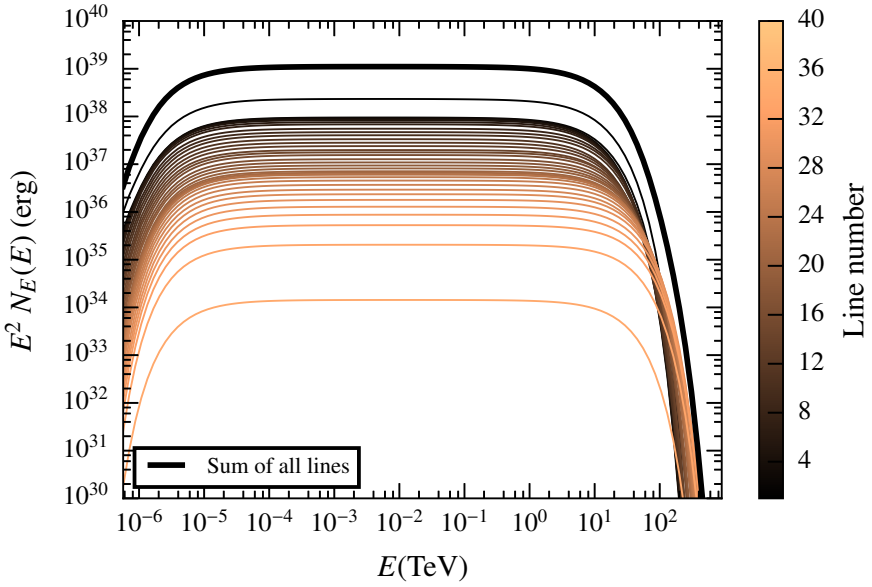

Figure 3.12: Particle energy distributions for the different streamlines (thin brown lines), and the sum of all of them (thick black line) for the jet-star interaction in the steady-state and $z_{\rm int} = 10$ pc, $\chi_B = 10^{-4}$.

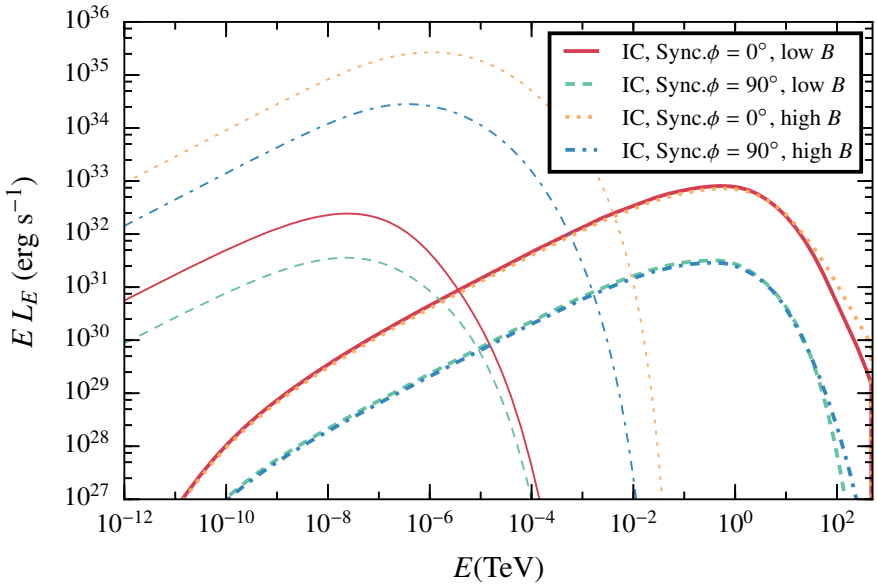

Figure 3.13: Synchrotron (thin) and IC (thick line) SEDs for the jet-star interaction in the perturbed state, taking $z_{\rm int} = 10$ pc, $\chi_B = 10^{-4} - 1$, and $\phi = 0° - 135°$.

plane of the bolometric luminosity per cell for both synchrotron and IC, taking $\chi_B = 10^{-4}$, $z_{\rm int} = 10$ pc, and $\phi = 0°$.

Figure 3.16 shows the synchrotron and IC SEDs for the two cases studied in this thesis, in the low- and high-magnetization case and for $\phi = 0°$ and $z_{\rm int} = 10$ pc. The figure shows that the synchrotron emission is significantly higher for the star-jet interaction in the perturbed state than in the steady state because a larger section of the jet is affected by the stellar wind, which is apparent from comparing the two pannels in Fig. 3.1 in Sect. 3.2. This implies that more jet energy is available for radiation. On the other hand, the IC radiation levels change very little when compared to the synchrotron levels because the target photon density significantly drops with distance from the star. In the high-magnetization case, the differences between the two studied cases are smaller than for a low magnetization, and the synchrotron SED of the perturbed case shows a softer spectrum at the highest energies. This is most likely related to the high magnetic field, which through severe synchrotron cooling prevents the most energetic electrons from reaching regions of higher Doppler-boosting. Otherwise, the radiation of these particles would have led to more flux at the higher synchrotron energies and thus to a harder spectrum.

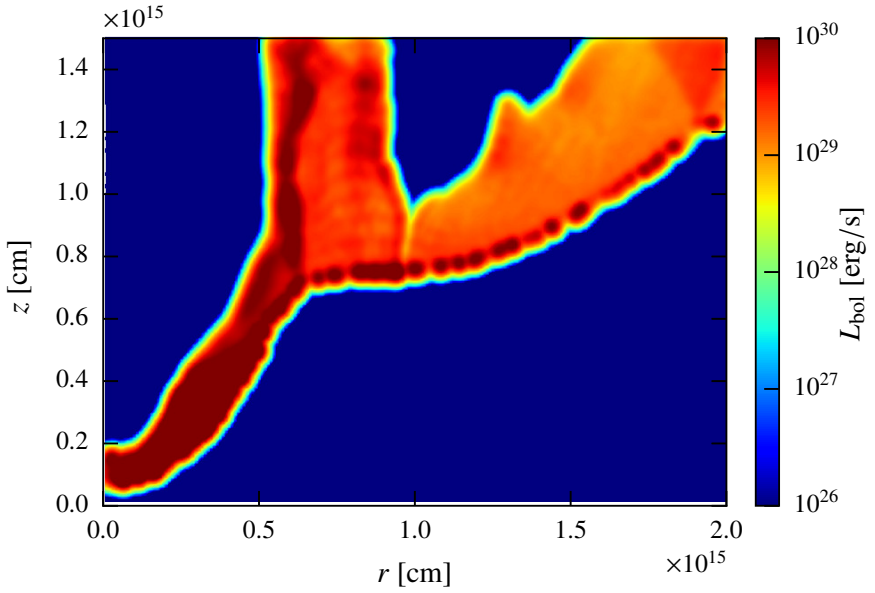

Figure 3.14: Map in the rz-plane of the distribution of IC, bolometric luminosity per cell for the jet-star interaction in the perturbed state. The adopted parameters are $\phi = 0$, $\chi_B = 10^{-4}$ and $z = 10$ pc.

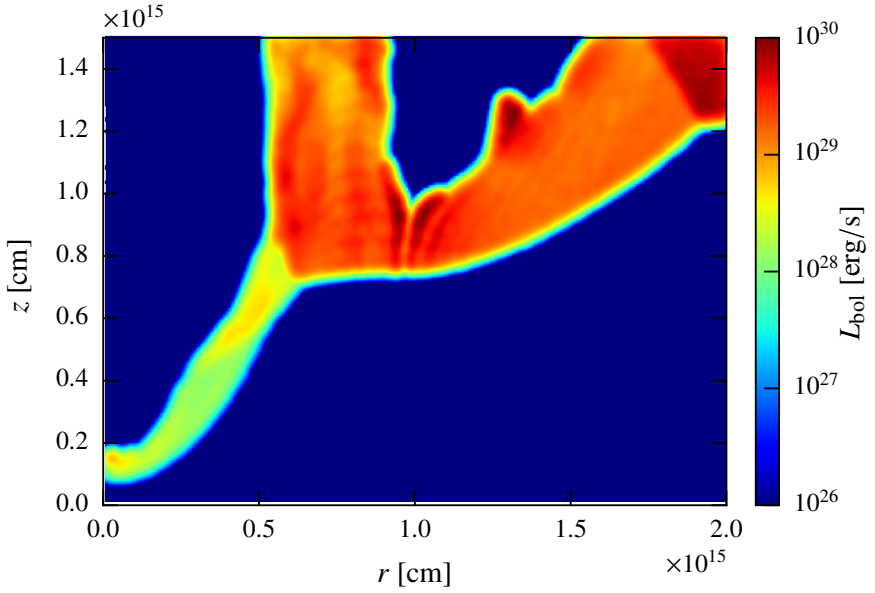

Figure 3.15: Map in the rz-plane of the distribution of synchrotron, bolometric luminosity per cell for the jet-star interaction in the perturbed state. The adopted parameters are $\phi = 0$, $\chi_B = 10^{-4}$ and $z = 10$ pc.

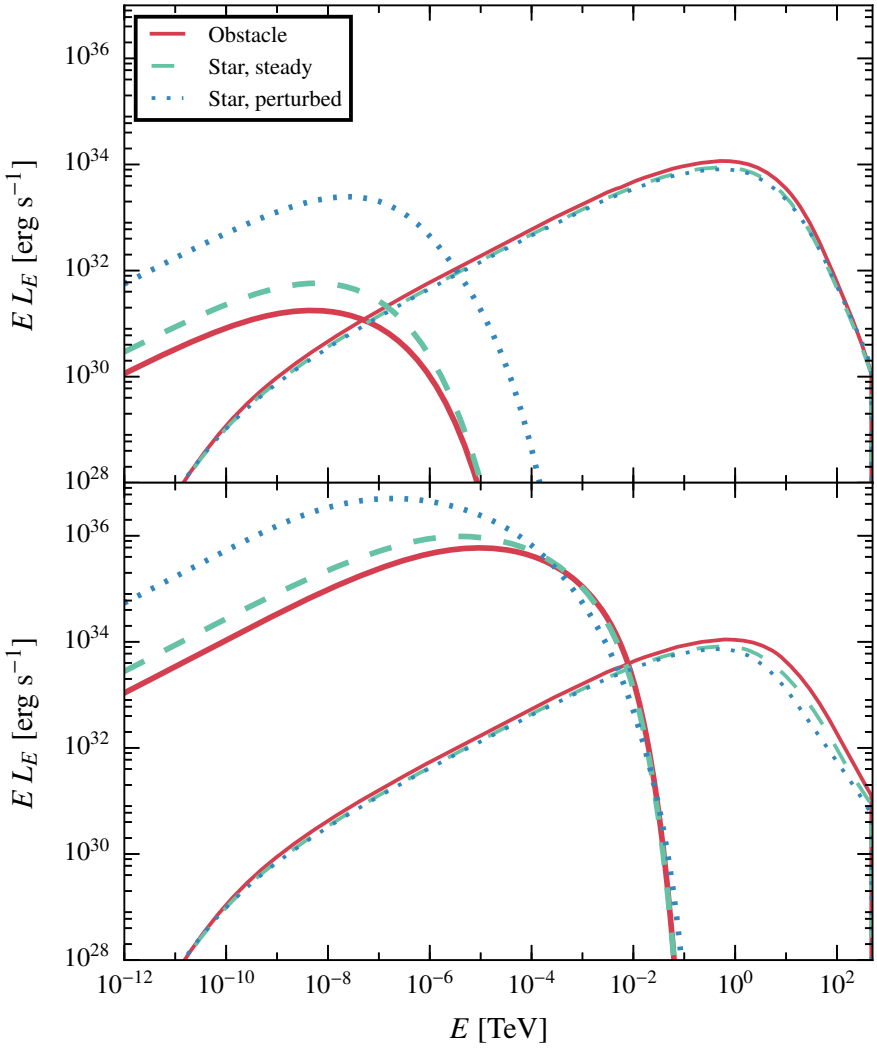

Figure 3.16: Synchrotron (thin) and IC (thick line) SEDs for the star-jet steady and perturbed state, taking $\phi = 0°$ and $z_{\rm int} = 10$ pc, for low magnetic field $\chi_B = 10^{-4}$ (upper pannel) and high magnetic field 10^{-1} (lower pannel).

3.4 CONCLUSIONS

The results of the radiation calculations carried out using hydrodynamical information are in the line of those presented in Bosch-Ramon, 2015. In that paper, it was noted that the effective size of the obstacle is much larger than the distance at which this and the jet flow collided —the stagnation radius (i). It was also pointed out that Doppler-boosting plays a significant role (ii). All this is confirmed here:

(i) For instance, for the jet-star interaction in the steady-state with $\phi = 0°$, $z_{\rm int} = 10$ pc, and $\chi_B = 10^{-4}$, the total observer luminosity is $\approx 3.5 \times 10^{31}$ and 5×10^{33} erg s^{-1} for the synchrotron and IC components, respectively, whereas the synchrotron and IC luminosities from a region with $r < R_{\rm CD}$ are $\approx 2 \times 10^{29}$ and 8×10^{31} erg s^{-1}, respectively, which is a factor ~ 100 smaller than for the whole grid.

(ii) In addition, the total synchrotron and IC luminosity in the FF are $\approx 1.3 \times 10^{30}$ and 2×10^{32} erg s^{-1}, respectively, which is a factor ~ 30 smaller than the observer values when Doppler-boosting is not accounted for. It is worth noting that jets on kpc and larger scales may be less relativistic, as considered in Bednarek and Banasiński, 2015, but closer to the galaxy centre, they are likely to have much higher Lorentz factors. Farther out, jet-boundary instabilities, shear-layer development, recollimation shocks, and mass-loss from stellar winds work together to decelerate the jets (see e.g. Perucho, 2014, 2015).

As expected from previous work (e.g. Araudo et al., 2013; Bednarek and Banasiński, 2015; Bosch-Ramon, 2015), we find that advection escape dominates radiation losses in the star-jet interactions studied, that is, for moderately powerful jets and stellar winds. Radiation peaks from X-rays to MeV energies depending on χ_B for synchrotron emission, and in the 100-1000 GeV range for IC, with the cooler, either older or less massive, stars yielding a higher IC SED peak energy (~ 1 TeV, as in the present work). A study of collective interactions of many stars with the jet (see Araudo et al., 2013, for massive stars) is under way to also account for other stellar populations such as evolved stars and for the increased effective section of the obstacles and relativistic effects. However, Bosch-Ramon, 2015 predicted significant collective emission, for which they took the stellar populations of the inner regions of the radio galaxy M 87 as a reference. These predictions receive further support here because we obtain similar IC fluxes and general behaviour for individual interactions, although we note that a more detailed prescription of the stars and their winds in the inner regions of AGN is required.

Instabilities might play an important role, and the shocked flow structure might be relatively unstable. This may enhance the emission for some individual jet-star interactions, although the collective emission would likely be at about steady-state radiation levels. Otherwise, for interactions taking place in the innermost jet regions and bright enough to be detectable by themselves, instability growth could temporary increase the emission levels and induce variability on scales $\gtrsim R_{\rm CD}/v_{\rm sw}$ in addition to other types of variability, such as that associated with jet crossing. It is worth noting that a longitudinal magnetic field in the jet would likely reduce the instability growth.

3.5 FINAL REMARKS

The question whether electrons or $e^{\pm}$-pairs are indeed accelerated in the jet shock is a key point. Bosch-Ramon, 2015 showed that for luminosities per interaction similar to those obtained by us and under the same interaction conditions, collective jet-star interactions could yield detectable levels of emission in M 87, for instance. Therefore, our results together with those from Bosch-Ramon, 2015 indicate that for acceleration efficiencies of $\chi_{\rm NT} \gtrsim 0.1$, collective star-jet interactions may be detectable in AGN in gamma rays unless (i) an AGN jet is a stronger emitter through a different mechanism, and/or (ii) the source is far and the jet seen off-axis, and/or (iii) the jet power is low. It is worth noting that the need of a relatively high $\chi_{\rm NT}$-value applies particularly to the low-B scenario, because for higher magnetizations the synchrotron component could overcome the IC in the 100 MeV region, which would weaken this requirement.

The limited size of the grid makes accounting for all the emission produced in the interaction region difficult, in particular for the synchrotron radiation. Bosch-Ramon, 2015 noted that non-negligible kinetic to internal energy transformation takes place far from the simulation axis, although with a weak r-dependence. However, Doppler-boosting effects are expected to be strong far from the obstacle, and synchrotron emission can come from farther regions than IC because the latter is affected by stellar field dilution with distance from the star. Larger grid simulations or jet-scale semi-analytic calculations are required to determine the emission contribution of these farther regions. As a reference, we point out that for the case with $\phi = 0°$, $z_{\rm int} = 10$ pc, and $\chi_B = 10^{-4}$, $\sim 10\%$ of the synchrotron and 30% of the IC total luminosity come from a distance $3 \times R_{\rm CD}$ from the simulation axis. Therefore, the trend of the IC emission

indicates convergence, but the synchrotron emission may be still far from that. This is linked to the fact that our simulations yield very low adiabatic cooling rates. The dominant source by far of non-thermal energy loss is advection escape from the grid. This is consistent with the modest density decrease with z in the shocked jet flow, as the density maps in Sect. 3.2.2 illustrate. Our results are complementary to those in Bednarek and Banasiński, 2015, where jet emission from particles accelerated in jet-obstacle interactions was computed by accounting for the jet B and photon fields that are relevant on larger spatial scales, such as the galaxy bulge or the CMB. A larger grid would also help to study more unstable configurations, such as adopting a higher density wind-jet contrast or increasing the resolution for a more realistic setup, although the computation time required would severely increase. Finally, 3D simulations that account for the star motion also need to be carried out.

Part III

GALACTIC SOURCES

This part of the thesis is the result of the work published in the article *Non-thermal radiation from a pulsar wind interacting with an inhomogeneous stellar wind*, V. M. de la Cita et *al.* A&A 598, A13 (2017), and the article *Gamma rays from clumpy wind-jet interactions in high-mass microquasars*, V. M. de la Cita et *al.* 2017, accepted for publication in A&A.

4

PULSAR WIND INTERACTING WITH A CLUMPY STELLAR WIND

4.1 INTRODUCTION

In binaries hosting a high-mass star and a young non-accreting pulsar, strong interaction between the relativistic pulsar wind and the stellar wind is expected, as it was stated in Chap. 1. In these wind collisions, efficient particle acceleration and non-thermal emission can take place (e. g. Maraschi and Treves, 1981; Tavani et al., 1994), which would be behind the emission observed from radio to gamma rays in some of these objects, like PSR B1259 – 63 (e.g. Aharonian et al., 2005; Chernyakova et al., 2014). Given that this emission, or at least a significant fraction of it, is expected to originate in the region where the winds collide, a proper characterization of the stellar and the pulsar wind is needed to understand the involved physical processes.

Density inhomogeneities, or clumps, are thought to be present in the stellar winds of early-type stars (Lucy and Solomon, 1970). The hydrodynamical and radiative consequences of the presence of clumps were studied analytically in Bosch-Ramon, 2013, and relativistic, axisymmetric, RHD simulations were carried out by Paredes-Fortuny et al., 2015

to study in more detail the impact of different types of clumps on the two-wind interaction region. It was found that clumps can noticeably affect the shape, size, and the stability of the interaction structure, and the variability patterns of the radiation coming from the structure. It was also proposed that wind inhomogeneities could be responsible of the GeV flare in PSR B1259 – 63 (Chernyakova et al., 2014), and may also play an important role in the X-ray activity of some binaries (see e.g. the discussion in Bosch-Ramon, 2013, and references therein). However, the impact of the presence of inhomogeneities in the stellar wind in the high-energy emission has not been accurately studied yet.

In this chaper we compute for the first time the synchrotron and IC emission produced by the interaction of an inhomogeneous stellar wind and a pulsar wind based on hydrodynamic simulations, obtaining the SEDs and maps of the emitting region. To characterize the impact of wind inhomogeneities on the non-thermal radiation, we have used the flow information obtained from the RHD simulations done by Paredes-Fortuny et al., 2015. From the flow hydrodynamical quantities, we have obtained a number of streamlines, characterizing the fluid of interest in the form of several 1D structures from which, following the method described in Chap. 2, we compute the synchrotron and the IC radiation. As the stellar photon field is very dense, gamma-ray absorption due to electron-positron pair creation has been taken into account.

A region of a size similar to the star-pulsar separation distance is considered. The reasons are threefold: (i) in this thesis, we are mostly concerned with the main radiation features resulting from the interaction of a clump with the two-wind collision structure; (ii) we are interested in the highest energies, which are expected to be produced on the binary scales (however, see Zabalza et al., 2013); (iii) for reasons explained in Paredes-Fortuny et al., 2015, simulation results were limited to these scales. Since radio emission is expected to be produced far from the binary system (e.g. Dubus, 2006b; Bosch-Ramon, 2011), the focus here is put on X-rays and gamma rays.

Regarding the most recent simulations of stellar and pulsar winds collisions, few important differences from our thesis are to be mentioned. The simulations in Dubus et al., 2015 are three-dimensional (3D), whereas here the hydrodynamical results are taken from the simulations of Paredes-Fortuny et al., 2015, carried out with axisymmetry (2D). In addition, the grid was significantly larger in Dubus et al., 2015 than in Paredes-Fortuny et al., 2015. Regarding Bosch-Ramon et al., 2015, the 3D simulations included orbital motion, which proved to be important beyond few star-

pulsar separation distances. That said, we note that the relatively small size of the computational grid in the present work allows orbital motion to be neglected, although instability development may be slower in our 2D simulations (see Sect. 4.2), and 3D calculations may yield remarkable quantitative differences in general. We note as well that the dynamical role of the magnetic field was not included in Paredes-Fortuny et al., 2015. So far, only Bogovalov et al., 2012 have included the magnetic field when computing the two-wind interaction structure in the context of binary systems, whereas several works have studied the magnetohydrodynamics in 1D, 2D and 3D, and in some cases the radiation for isolated pulsars interacting with the environment in the relativistic regime (e.g. Bucciantini et al., 2005; Volpi et al., 2008; Olmi et al., 2014; Porth et al., 2014; Morlino et al., 2015; Yoon and Heinz, 2016, and references therein).

4.2 HYDRODYNAMICS

Our work is based in the axisymmetric RHD simulations of the interaction of a relativistic pulsar wind and an inhomogeneous stellar wind performed by Paredes-Fortuny et al., 2015. We simulated first a stellar wind without clumps until a steady state of the two-wind interaction region was achieved. Then, a spherical inhomogeneity centred at the axis between the two stars was introduced.

The physical size of the domain is $r \in [0, l_r]$ with $l_r = 2.4 \times 10^{12}$ cm, and $z \in [0, l_z]$ with $l_z = 4.0 \times 10^{12}$ cm. The star is located outside the simulated grid at $(r_*, z_*) = (0, 4.8 \times 10^{12})$ cm, and its spherical wind is injected as a boundary condition at the top of the grid. The pulsar is placed inside the grid at $(r_p, z_p) = (0, 4 \times 10^{11})$ cm, and its spherical wind is injected at a radius of 2.4×10^{11} cm (15 cells). The star-pulsar separation is $d = 4.4 \times 10^{12}$ cm. The lower and right boundaries of the grid were set to outflow, whereas the left boundary was set to reflection. The selected physical parameters for the stellar wind at a distance $r = 8 \times 10^{10}$ cm with respect to the star centre were: the mass-loss rate $\dot{M} = 10^{-7}$ $M_\odot$ yr^{-1}, the stellar wind radial velocity $v_{sw} = 3000$ km s^{-1}, and the specific internal energy $\epsilon_{sw} = 1.8 \times 10^{15}$ erg g^{-1}; the derived stellar wind density is $\rho_{sw} = 2.68 \times 10^{-13}$ g cm^{-3}. Similarly, the chosen physical parameters for the pulsar wind at a distance $r = 8 \times 10^{10}$ cm with respect to the pulsar centre were: the pulsar wind Lorentz factor $\Gamma = 5$; the specific internal energy $\epsilon_{pw} = 9.0 \times 10^{19}$ erg g^{-1}; the density $\rho_{pw} = 2 \times 10^{-19}$ g cm^{-3}; the derived total pulsar wind luminosity is $L_p = 10^{37}$ erg s^{-1}, and the pulsar-

to-stellar wind momentum rate ratio $\eta \approx 0.2$. The two wind parameters are summarized in Table 4.1.

The simulation adopted resolution was modest, 150 and 250 cells in the radial and the vertical directions, respectively. This resolution is high enough to get the main dynamical features of the two-wind interaction structure, but low enough to avoid a too disruptive instability growth, as explained in Paredes-Fortuny et al., 2015 (see also Perucho et al., 2004). As noted in that work, the fast instability growth in the two-wind collision region is physical (see also Bosch-Ramon et al., 2012b, 2015), although the presence of a singularity in the radial coordinate may introduce additional numerical perturbations to the colliding structure. A much larger grid should have allowed the growing instabilities to leave the computational domain without disrupting the simulation, although some trials have indicated that even under the same resolution, grids that are two to three times larger eventually also led to simulation disruption, filling the whole grid with shocked flow. Therefore, being the goal in Paredes-Fortuny et al., 2015 (and here) to carry out a preliminary analysis of the problem, the choices adopted were a modest resolution (to keep perturbation growth under control) and a relatively small grid size, which both allow the simulation to reach a quasi-steady state solution for the case of the pulsar-star wind interaction without clumps.

Once the (quasi)-steady state was reached, an inhomogeneity was introduced to the stellar wind. The inhomogeneous wind was thus characterized by a single clump placed at $(r,z) = (0, 2.6{\times}10^{12})$ cm parametrized by its radius R_c and its density contrast χ with respect to the density value at the location where the clump was introduced. A thorough description of the simulations and their results is given in Paredes-Fortuny et al., 2015. Here, two cases among those considered in that work are studied: (i) a clump with $\chi = 10$ and $R_c = 8 \times 10^{10}$ cm; and (ii) a clump with $\chi = 10$ and $R_c = 4 \times 10^{11}$ cm.

After obtaining the hydrodynamical information, and prior to the radiative calculations, the streamlines of the pulsar wind have to be computed, as it was detailed in Sec. 2.1.1. We computed the streamlines starting from a distance 2.4×10^{11} cm from the pulsar centre. The magnetic field, is computed as stated in Sec. 2.1.2.

The left panel of Fig. 4.1 shows the computed streamlines superimposed on the density map for the simulation steady state. The centre panel of Fig. 4.1 illustrates the re-acceleration of the shocked pulsar wind as it is advected along the shock. The right panel of Fig. 4.1 shows the effect of Doppler boosting quantified by a factor δ^4 for the viewing an-

Parameter	Stellar wind	Pulsar wind
v	3×10^{8} cm s^{-1}	2.94×10^{10} cm s^{-1}
ϵ	1.8×10^{15} erg g^{-1}	9×10^{19} erg g^{-1}
ρ	2.68×10^{-13} g cm^{-3}	2×10^{-19} g cm^{-3}
$(r_{*/\mathrm{p}}, z_{*/\mathrm{p}})$	$(0, 4.8\times10^{12}$ cm$)$	$(0, 4\times10^{11}$ cm$)$

Table 4.1: Stellar and pulsar parameters. Wind velocity v, specific internal energy ϵ, and density ρ at a distance $r = 8\times10^{10}$ cm with respect to the star/pulsar centres, located at $(r_{*/\mathrm{p}}, z_{*/\mathrm{p}})$.

gles with respect to the pulsar-star axis $\phi = 45°$ and $135°$[1]. The same is shown for the two cases with different wind inhomogeneity: Fig. 4.2 for the clump with $\chi = 10$ and $R_{\mathrm{c}} = 8\times10^{10}$ cm and Fig. 4.3 for the clump with $\chi = 10$ and $R_{\mathrm{c}} = 4\times10^{11}$ cm.

1 An observer with $\phi = 0°$ would be looking along the star-pulsar axis.

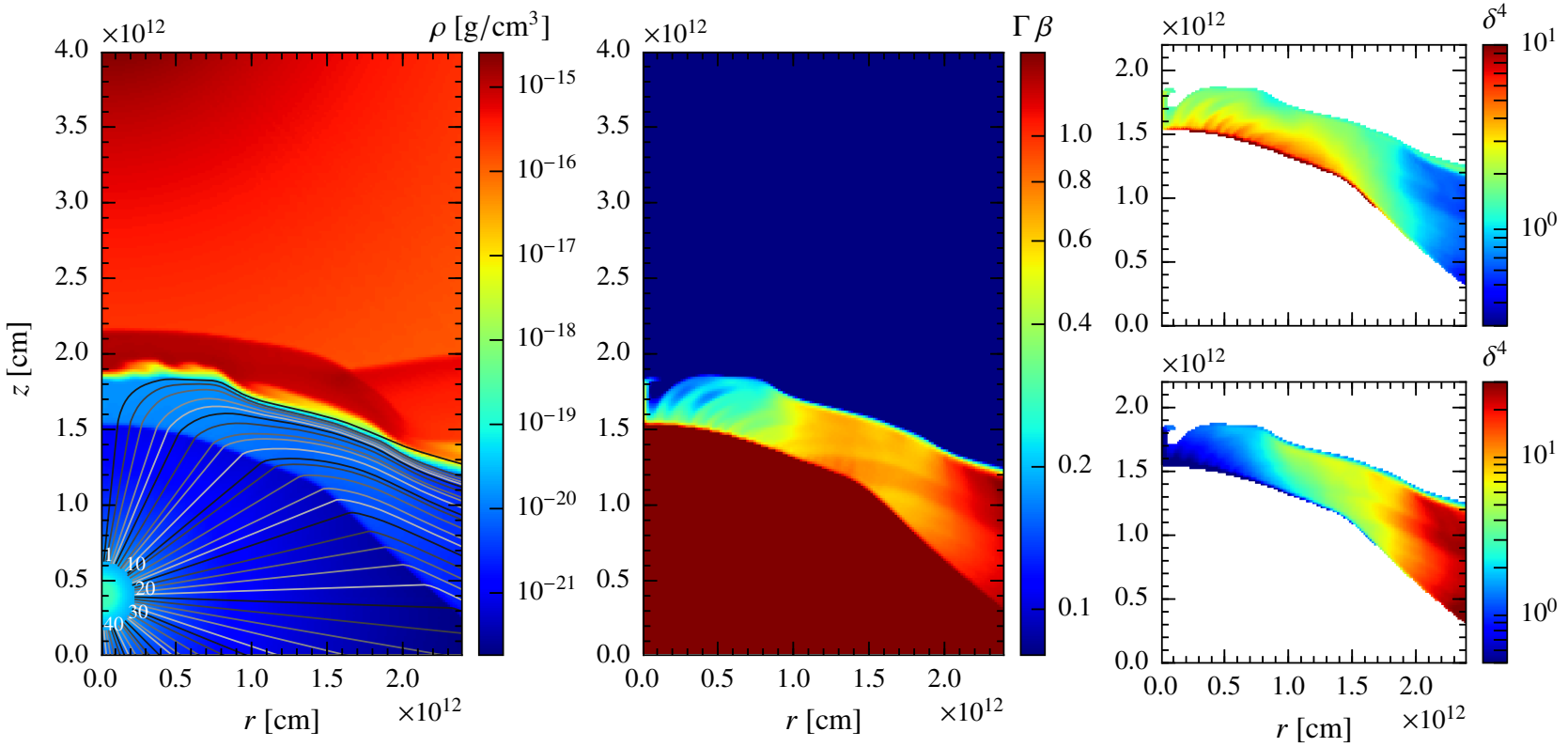

Figure 4.1: Left panel: Density distribution by colour at time $t = 5.8 \times 10^4$ s in the (quasi)-steady state. The star is located at $(r_*, z_*) = (0, 4.8 \times 10^{12})$ cm and the pulsar wind is injected at a distance of 2.4×10^{11} cm with respect to the pulsar centre at $(r_p, z_p) = (0, 4 \times 10^{11})$ cm. The grey lines show the obtained streamlines describing the trajectories of the pulsar wind fluid cells; the grey scale and the numbers are only for visualization purposes. Centre panel: Distribution by colour of the module of the 4-velocity at time $t = 5.8 \times 10^4$ s in the (quasi)-steady state. Right panel: Distribution by colour of the Doppler boosting enhancement (δ^4) for the emission produced in the shocked pulsar wind, as seen from 45° (top) and 135° (bottom) from the pulsar-star axis, at time $t = 5.8 \times 10^4$ s in the (quasi)-steady state.

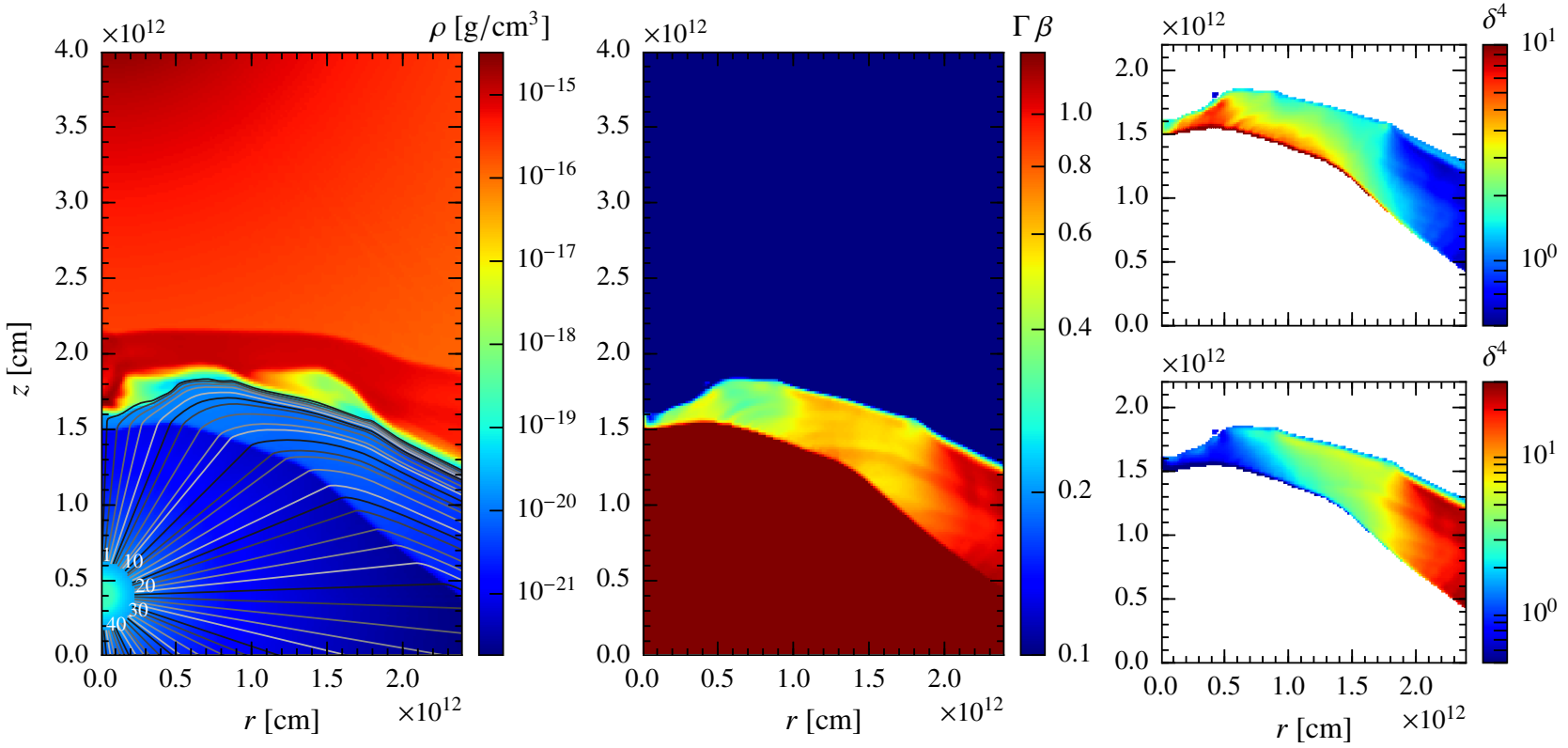

Figure 4.2: Left panel: Density distribution by colour at time $t = 0.4 \times 10^4$ s (measured from the steady case) considering an inhomogeneous stellar wind with $\chi = 10$ and $R_c = 8 \times 10^{10}$ cm. The remaining plot properties are the same as those in Fig. 4.1. Centre panel: Module of the 4-velocity. Right panel: Doppler boosting enhancement as seen from 45° (top) and 135° (bottom)

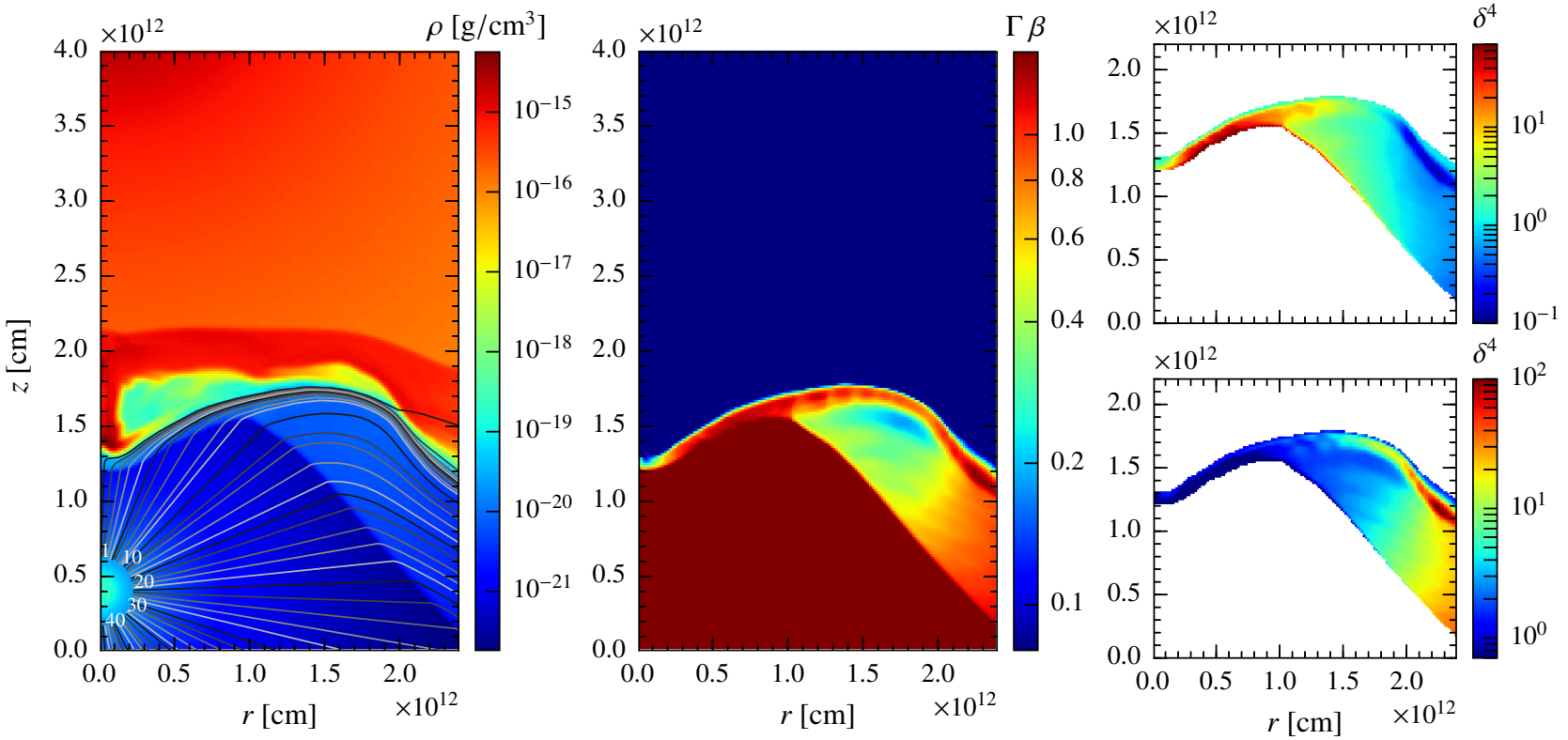

Figure 4.3: Left panel: Density distribution by colour at time $t = 1.1 \times 10^4$ s (measured from the steady case) considering an inhomogeneous stellar wind with $\chi = 10$ and $R_c = 4 \times 10^{11}$ cm. The remaining plot properties are the same as those in Fig. 4.1. Centre panel: Module of the 4-velocity. Right panel: Doppler boosting enhancement as seen from 45° (top) and 135° (bottom)

4.3 RADIATION

4.3.1 *Non-thermal emitter*

In this work, we consider that the non-thermal emitter is restricted to the shocked pulsar wind, i.e., particles are accelerated at the pulsar wind termination shock, although the unshocked pulsar wind may also be an efficient gamma-ray emitter for certain values of the wind Lorentz factor (e.g. Aharonian and Bogovalov, 2003; Khangulyan et al., 2007).

Particle acceleration in pulsar wind termination shocks is not yet well understood. Our main aim here, however, is just to show general trends in the radiation due to the presence of clumps. Therefore, we follow the phenomenological approach described in 2.2. A value for the fraction $\eta_{\rm NT}$ of 0.1 is taken, but all the results scale linearly; currently, this quantity cannot be derived from first principles.

Once the injection of non-thermal particles is characterized, we compute the energy evolution and spatial propagation of particles along the streamlines until they leave the grid, which eventually leads to a steady state. Then, the synchrotron and IC emission for each cell, for all the streamlines, are computed in the FF, and appropriately transformed afterwards to the observer frame, as described already in Sec. 2.4. In the present scenario, the gamma-ray absorption due to electron-positron pair creation in the stellar photon field cannot be neglected and is taken into account.

To keep the calculations manageable, emission of secondary particles from gamma-ray absorption (i) and IC cascading (ii) has not been considered, but these processes could indeed be important in close binaries, mainly increasing the X-ray fluxes (i; high ambient magnetic field), or enhancing the effective transparency of the system (ii; low ambient magnetic field) (e.g. Sierpowska and Bednarek, 2005; Aharonian et al., 2006b; Sierpowska-Bartosik and Torres, 2007; Bosch-Ramon et al., 2008; Cerutti et al., 2010; Bosch-Ramon and Khangulyan, 2011).

The companion star is by far the dominant source of target IC photons. The stellar spectrum has been assumed to be typical for an O-type star: a black body with a temperature and luminosity of $T_\star = 4\times10^4$ K and $L_\star = 10^{39}$ erg s^{-1}, respectively. The high stellar luminosity allows us to neglect the radiation field produced in the emitter itself, in particular the role of synchrotron self-Compton radiation, which is a safe assumption as long as $L_\star \gg L_{\rm p}/\eta$. The magnetic field is set as specified in Eq. (2.5) using two values for χ_B, 10^{-3} and 0.1, illustrative of a low and a high magnetic

Parameter	Set of values
Observation angle ϕ	45, 90, 135°
Fraction χ_B	10^{-3}, 0.1

Table 4.2: Set of parameters for the three scenarios considered.

field case, respectively. Typically, pulsar winds at termination are thought to be strongly dominated by their kinetic energy (e.g. Kennel and Coroniti, 1984; Bogovalov et al., 2012; Aharonian et al., 2012), although some models predict a high magnetization up to the termination shock, where the magnetic field would efficiently dissipate (e.g. Lyubarsky and Kirk, 2001). We note that for $\chi_B = 0.1$ the condition of a negligible magnetic field becomes only marginally fulfilled.

4.3.2 *Results*

The non-thermal emission was computed for three different stellar wind scenarios: the steady state of the two-wind interaction structure with no clump, the case with a small clump ($\chi = 10$, $R_c = 8 \times 10^{10}$ cm), and the case with a large clump ($\chi = 10$, $R_c = 4 \times 10^{11}$ cm). In addition to considering two magnetic field cases ($\chi_B = 10^{-3}$ and 0.1), three representative viewing angles were also considered: $\phi = 45°$, 90°, and 135°. The first angle corresponds for instance to the superior conjunction (SUPC) of the compact object and a system inclination of 45°, the second to an intermediate orbital phase, and the third might represent the inferior conjunction (INFC) for the same inclination; the parameter values are listed in Table 4.2.

The simulation times adopted for the emission calculations, of the cases including a clump, were chosen such that the clump was at its closest point from the pulsar; the state of the emitting flow can be considered steady given the short time needed for the particles to leave the grid. For each of these scenarios, we obtained the corresponding synchrotron and IC SEDs. These SEDs are presented in Figs. 4.4–4.9, the last of which shows the contribution from each streamline. Figure 4.10 shows the particle energy distribution in the LF for each streamline, and the summation of all of them. Maps were also computed to show how the emission is distributed in the *rz*-plane in the shocked pulsar wind region. These maps are presented in Figs. 4.11 and 4.12. Figure 4.13 illustrates the importance of the extended nature of the emitter comparing two SEDs:

those obtained for the computed emitter geometry, and those computed assuming that all the emitting cells have the pulsar location (keeping, nonetheless, the particle distributions of the extended emitter). The extended emitter on the scales studied has a minor effect on IC, but a major one in gamma-ray absorption for the represented case with $\phi = 45°$.

The impact of energy losses on the non-thermal particles can be seen by comparing the injected non-thermal luminosities with the energy leaving the computational domain per time unit in the LF. Particles lose 1.6×10^{35} erg s^{-1} through radiative losses, or a $\approx 23\%$ of the injected non-thermal luminosity in the no clump case; instead, in the large clump case 1.8×10^{35} erg s^{-1} is radiated, or $\approx 20\%$. The adiabatic losses have more impact, around 49% of the injected non-thermal luminosity for both no clump and large clump cases. The total injected non-thermal luminosities would be 7.1×10^{35} and 9.1×10^{35} erg s^{-1} for the cases without a clump and with a large clump, respectively. Doppler boosting shows up by comparing the synchrotron+IC total luminosity in the observer frame for the case without clump, $\phi = 90°$ and $\chi_B = 10^{-3}$, of 2.75×10^{35} erg s^{-1}, with the same quantity in the fluid frame, of 1.2×10^{35} erg s^{-1}, where there is an increase of a factor between 2 and 3 in the emission.

For informative purposes and completeness, we provide in Table 5.1 the luminosities in the energy bands 1–10 keV, 10–100 keV, 0.1–100 MeV, 0.1 – 100 GeV, and 0.1 – 100 TeV for the cases without and with clump, focusing on the low magnetic field case ($\chi_B = 10^{-3}$), which can be considered the more realistic one (see Sect. 4.3.1). It is clear that in the system considered, whose properties are representative (Dubus, 2013), the radiative cooling represents $\sim 1/4$ of the injected non-thermal luminosity, and for $\eta_{\rm NT} = 0.1$, a small percentage of $L_{\rm p}$. In the large clump case, adiabatic losses get enhanced with respect to the no-clump case because of the shrinking of the two-wind interaction region, a tendency previously suggested in Bosch-Ramon, 2013. This effect can be seen as a suppression of the lower energy part (where adiabatic losses are important) of the IC spectra in Fig. 4.7.

Scenario	ϕ	1 – 10 keV	diff., %	10 – 100 keV	diff., %	0.1 – 100 MeV	diff., %	0.1 – 100 GeV	diff., %	0.1 – 100 TeV	diff., %
No-Clump	45	1.25×10^{33}		4.51×10^{33}		6.13×10^{34}		1.43×10^{35}		2.06×10^{34}	
	90	1.66×10^{33}		5.97×10^{33}		6.42×10^{34}		1.54×10^{35}		4.91×10^{34}	
	135	1.15×10^{33}		3.88×10^{33}		1.92×10^{34}		1.50×10^{34}		1.41×10^{34}	
Small Clump	45	1.27×10^{33}	1.6	4.60×10^{33}	2.0	6.92×10^{34}	12.9	2.38×10^{35}	66.4	3.24×10^{34}	57.3
	90	1.75×10^{33}	5.4	6.10×10^{33}	2.2	5.53×10^{34}	-13.9	1.57×10^{35}	1.9	4.66×10^{34}	-5.1
	135	1.98×10^{33}	72.2	6.73×10^{33}	73.5	3.14×10^{34}	63.5	2.86×10^{34}	90.7	2.32×10^{34}	64.5
Big Clump	45	2.05×10^{33}	64.0	6.38×10^{33}	41.5	5.49×10^{34}	-10.4	1.35×10^{35}	-72.0	1.52×10^{34}	-83.5
	90	3.25×10^{33}	90.4	1.01×10^{34}	69.2	7.43×10^{34}	15.7	1.71×10^{35}	9.1	3.80×10^{34}	-17.5
	135	4.07×10^{33}	253.9	1.21×10^{34}	211.9	5.24×10^{34}	172.9	6.05×10^{34}	303.3	5.16×10^{34}	266.0

Table 4.3: Values of the integrated emission in different bands for the case of weak magnetization, $\chi_B = 10^{-3}$, given in erg s^{-1}; and the difference imposed by clumps to the homogeneous case, given in per cent.

4.3.3 *Applications to PSR B1259 – 63*

The binary pulsar system PSR B1259 – 63 consists of a 47.7 ms radio pulsar (Johnston et al., 1992; Kijak et al., 2011) on an eccentric orbit around a luminous O8.5 Ve star (Negueruela et al., 2011). The pulsar orbits are characterized by the following orbital parameters: eccentricity $e = 0.87$, period $P_{\rm orb} = 3.5$ yr, and semi-major axis $a_2 = 6.9\,{\rm AU}$ (see Negueruela et al., 2011, and references therein). The stellar companion in the system is thought to rapidly rotate (Negueruela et al., 2011). The rotation results in a strong surface temperature gradient ($T_{\rm pole} = 3.4 \times 10^4$ K and $T_{\rm eq} = 2.75{\times}10^4$ K), and in the formation of a circumstellar disc. The plane of the orbit and the disc plane are expected to be misaligned. Negueruela et al. (2011) derived the orbital inclination of $i_{\rm orb} \approx 23^\circ$ and suggested that the star rotation axis is inclined with respect to the line of sight by 32° (i.e., the star is mostly seen from the pole). Accounting for the uncertainty of the star orientation, the IC emission/loss process can be well approximated by a black body with temperature $T_* = 3{\times}10^4$ K (Khangulyan et al., 2011).

The temperature and luminosity of the UV companion correspond to a late O star, but because of the fast rotation a Be star-type disc is formed. Thus the stellar wind in PSR B1259 – 63 should consist of two distinct regions: a dense Keplerian disc, which is crossed by the pulsar approximately −16 and +18 days to periastron passage and a fast low-density polar wind. The mass-loss rate and density of the discs around Be stars can vary significantly, but the density should be significantly higher than in the polar wind, and the azimuthal velocity should be Keplerian, i.e., $v_{\rm d} \sim 2 \times 10^2\,{\rm km\,s^{-1}}$ (at a distance of $10^{13}\,{\rm cm}$ from the star). Based on the shape of the X-ray light curve, Takata et al. (2012) predicted that the density of the disc base in PSR B1259−63 might be very high $\rho_0 \sim 10^{-9}\,{\rm g\,cm^{-3}}$, but this conclusion is likely affected by large uncertainties. The polar wind should be similar to a wind from a O-type star, $v_{\rm w} \sim 2 \times 10^3\,{\rm km\,s^{-1}}$. Both these winds might be inhomogeneous, but the disc clumps can be significantly more massive, so in what follows we consider the possible impact of a disc clump on the non-thermal emission in the system.

The system displays variable broadband non-thermal radio, X-ray, and TeV gamma-ray emission close to periastron passage (Grove et al., 1995; Johnston et al., 2005; Chernyakova et al., 2006; Aharonian et al., 2005, 2009; Uchiyama et al., 2009; H.E.S.S. Collaboration et al., 2013; Chernyakova et al., 2014, 2015; Caliandro et al., 2015; Romoli et al., 2015). Although the light curves of the non-thermal emission clearly diverge in different

energy bands, the general tendency is similar. Approximately 30 days to periastron passage the flux starts to increase and reaches its maximum around 20-10 days before periastron passage (depending on the energy band). When the pulsar approaches periastron, a decreasing tendency in the flux level is apparent. In the post-periastron epoch the flux increases again, and then gradually decreases. This two-hump structure is less pronounced in the radio band, probably because of the long cooling time of the radio-emitting electrons, and in TeV gamma rays, possibly because of larger data uncertainties. The X-ray light curve displays quite stable orbit-to-orbit behaviour with two clear maxima. The pre- and post-periastron maxima of the X-ray light curve are characterized by similar patterns: a sharp increase and a slower decay, with a larger maximum flux level in the post-periastron epoch (Chernyakova et al., 2015). The X-ray peaking fluxes are reached close to the epochs when the pulsed radio emission disappears. The weakening of the pulsed emission is conventionally associated with the pulsar eclipse by the circumstellar disc approximately during the epoch $(-16, +18)$ days to periastron passage. The location of the light curve maxima suggests that the circumstellar disc may play an important role in the formation of the non-thermal emission. In turn, as indicated by the change of the equivalent width of Hα (Chernyakova et al., 2015), the pulsar also affects the disc. This complex interplay makes modelling the emission in this system a very challenging task, thus a consistent multi-wavelength interpretation is currently missing (however, see Takata et al., 2012).

In addition to TeV gamma rays, bight GeV flares have been detected from the system with Fermi in 2011 January and 2014 May (see Caliandro et al., 2015, and references therein). In both epochs the onset of the flares occurred approximately one month after periastron passage. During the flare summit the measured GeV luminosity in 2011 was a factor of ~ 1.5 higher than, but the flare duration was similar to, that in 2014 (see e.g. Romoli et al., 2015). The typical flare flux is $\sim 10^{-6}\,\mathrm{ph\,cm^{-2}s^{-1}}$, which means a GeV output $\sim 10\%$ of the pulsar spin-down luminosity ($L_\mathrm{p} \approx 8 \times 10^{35}$ erg s^{-1}, Johnston et al. 1992) for the distance to the system of 2.3 pc (Negueruela et al., 2011). No detectable change in the TeV emission was observed during the onset of the GeV flare in 2011 (H.E.S.S. Collaboration et al., 2013). Hard X-ray emission detected with during the GeV flare suggests that the GeV emission might be generated by the same radiation mechanism as the multi-keV X-ray emission, namely through the synchrotron channel (Tam et al., 2015; Chernyakova et al., 2015).

In what follows we qualitatively consider the possible contribution of the emission generated by the interaction of stellar wind clumps with the pulsar wind to the radiation detected from PSR B1259 – 63, for the GeV flare, and the disc crossing in TeV.

4.3.3.1 *GeV flare*

As discussed in Paredes-Fortuny et al., 2015, the GeV flare detected from PSR B1259 – 63 by Fermi could be related to the impact of a dense, large clump of material, probably associated with the decretion disc of the Be star (Chernyakova et al., 2014). This GeV flare seems to follow a repetitive pattern (e.g. Caliandro et al., 2015; Chernyakova et al., 2015), which in the scenario just sketched would imply that the disc is similarly affected orbit to orbit, and parts of it are torn apart and directed towards the pulsar. The ram pressure of such a piece of circumstellar disc could have a strong impact on the two-wind interaction structure. As shown by Paredes-Fortuny et al., 2015, just a small fraction of the disc mass in the form of a clump of matter would be enough to strongly reduce the size of the interaction region. As was outlined above, the flare onset occurs approximately two weeks after the reappearance of the pulsed radio signal, and thus the pulsar has moved relatively far from the disc. We nevertheless assume that a dense cloud can still collide with the pulsar wind at this epoch.

The arrival of a large, dense piece of disc could potentially enhance, by compressing the emitting region, the energy density of the local radiation field (e.g. X-rays from the collision region, Dubus and Cerutti 2013; see also Khangulyan et al. 2012 for a related scenario based on IR target photons) to a point when synchrotron self-Compton (SSC) becomes dominant over external IC. This process seems nevertheless unlikely in PSR B1259 – 63. Given the pulsar spin-down and the stellar luminosities ($L_* \approx 3 \times 10^{38}$ erg s^{-1},Negueruela et al. 2011), even optimistically assuming that most of L_p goes to the target photons for SSC, adopting the Thomson approximation for IC, and neglecting IC angular effects, to increase the local photon energy density above the stellar level, the two-wind interaction region should become $\lesssim 1/40$ times the size typically considered. This is $\sim 10\%$ of the pulsar-star separation distance (Dubus and Cerutti 2013 obtained a similarly small emitting region). Although a detailed account of this possibility is still not available, such a huge reduction in size requires an increase in stellar material ram pressure by several orders of magnitude and does not seem plausible.

The arrival of a clump may by itself be enough to substantially enhance the IC emission for a combination of Doppler boosting, pulsar wind shock obliqueness, etc. To check this possibility, we computed the emission of the steady and the large clump cases adopting the parameters of PSR B1259 – 63 at the time of the flare in GeV (not shown here). We took the orbital phase to be around the inferior conjunction of the compact object, an inclination of 23°, and scaled the hydrodynamic solution (Paredes-Fortuny et al., 2015) to a star-pulsar separation distance in accordance with the source properties. This scaling yields a clump mass $\sim 10^{21}$ g, and a clump destruction time of about a week (the actual flare lasted for a few weeks). For instance, in the low B case, a jump in gamma-ray luminosity by a factor of ~ 2 was obtained, not far from the difference between the flare and the periastron Fermi luminosity in PSR B1259 – 63 (e.g. Caliandro et al., 2015). Unfortunately, the energetics in our case was short by about two orders of magnitude, even when adopting $\chi_{\rm NT} = 1$. Therefore, the simulated scenario is, in its present form, far from being able to explain the GeV flare in PSR B1259 – 63.

4.3.3.2 *Disc crossing and TeV emission*

We also studied the interaction of the pulsar wind with the Be star disc assuming that this may be roughly approximated as the encounter between the pulsar wind and a large inhomogeneity. From a hydrodynamical point of view, as shown in Okazaki et al., 2011, the disc may be of great dynamical importance for the geometry of the pulsar wind termination shock, and thus in the overall non-thermal emitting region (see Takata et al., 2012, for non-relativistic calculations without particle energy losses). The effects of the disc in the non-thermal emission in PSR B1259 – 63has already been discussed, for instance in Khangulyan et al., 2007 (see also Chernyakova et al. 2006).

We computed the SED for both the steady and the large clump cases when the pulsar is supposed to cross the Be disc after periastron passage. Assuming that the beginning of the disc crossing could be roughly modelled by the encounter with a large clump, we tried to semi-quantitatively reproduce the energetics and increase in flux above 100 GeV observed around those orbital phases. As the results were slightly improved, and given the inclination uncertainty, we adopted $i = 30°$ instead of 23°. As shown in Fig. 4.14, with minor changes in the calculation set-up and a little parameter tuning ($\eta_{\rm NT} = 1$; $\chi_B = 10^{-3}$)[2], similar flux levels and evolu-

2 Nontheless, we want to point out the high non-thermal efficiency needed.

tion (a rise by a factor of several) are obtained, although with a somewhat steeper spectrum than the average one given in Romoli et al., 2015.

4.4 CONCLUSIONS

The results shown in Figs. 4.4–4.10 are partially determined by several well-known effects. First, there is a competition between synchrotron and IC losses at particle energies high enough for radiation cooling to dominate over adiabatic losses. Different magnetic-to-target radiation energy density ratios yield different synchrotron-to-IC luminosity ratios. Dominant synchrotron or IC in the Thomson regime (for IC photons $\lesssim 10$ GeV) lead to a spectral softening, whereas dominant IC in Klein Nishina (for IC photons $\gtrsim 10$ GeV) leads to a spectral hardening (e.g. Khangulyan and Aharonian, 2005). Second, an important factor is IC scattering on an anisotropic target photon field, which softens and boosts the gamma-ray emission for close to head-on collisions (around SUPC), and hardens and reduces the gamma-ray emission for small scattering angles (around INFC) (e.g. Khangulyan et al., 2008; Dubus et al., 2008). Third, at the highest energies there is absorption through pair creation in the anisotropic photon field of the star. This process has its minimum threshold energy of the absorbed gamma rays ($\sim m_e^2 c^4 / 2.7\, kT_\star \approx 30$ GeV), and the strongest attenuation, for close to head-on collisions (around SUPC), whereas it presents a high absorption threshold, and weak attenuation, for small photon-photon interaction angles (around INFC) (e.g. Böttcher and Dermer, 2005; Dubus, 2006a; Khangulyan et al., 2008). For the adopted stellar luminosity and orbital separation distance, gamma-ray absorption around 1 TeV is very strong for $\phi < 90°$. This suggests that the bright TeV emission detected from several close binary systems, e.g. LS 5039 (Aharonian et al., 2006a), cannot be entirely generated in the inner part of the colliding wind structure, and some additional production sites should be considered (e. g. Zabalza et al., 2013).

The importance of synchrotron losses was discussed in Bosch-Ramon, 2013 in the context of a clump large enough to significantly reduce the size of the two-wind interaction region, which is expected to enhance the magnetic field in the shocked pulsar wind. This effect is seen in our results (see Table 5.1) when comparing the synchrotron and IC luminosities in different energy bands, and in the absence or presence of clumps. Adiabatic losses are also increased by the reduction of the two-wind interaction region, as noted in Sect. 4.3.2.

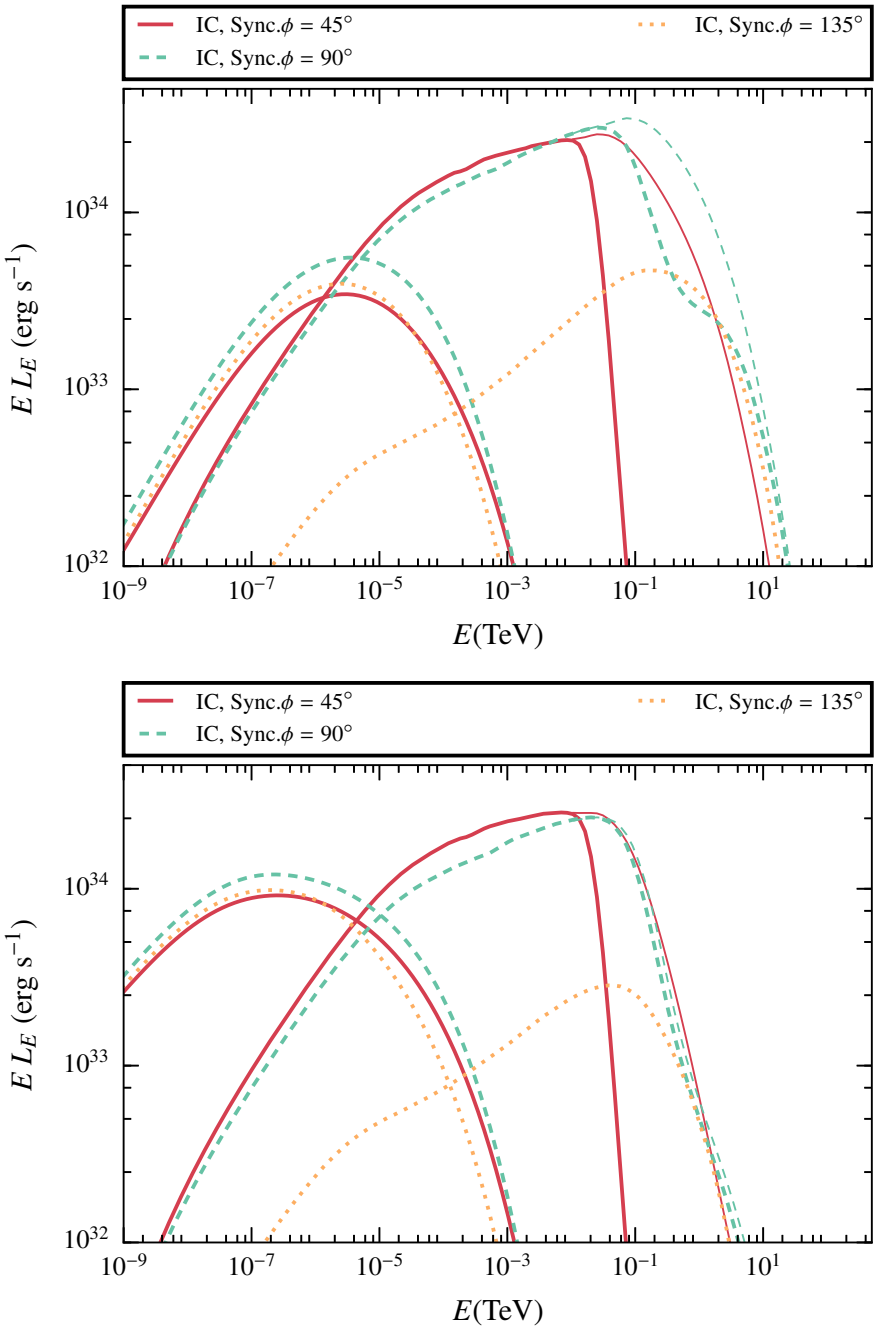

Figure 4.4: Spectral energy distribution of synchrotron and IC for the no clump scenario, in the low ($\chi_B = 10^{-3}$) and high ($\chi_B = 0.1$) magnetic field cases (top and bottom pannels, respectively). We note that the unabsorbed (thin lines) and the absorbed (thick lines) IC emission are distinguishable only for $\phi = 45°$ and 90°.

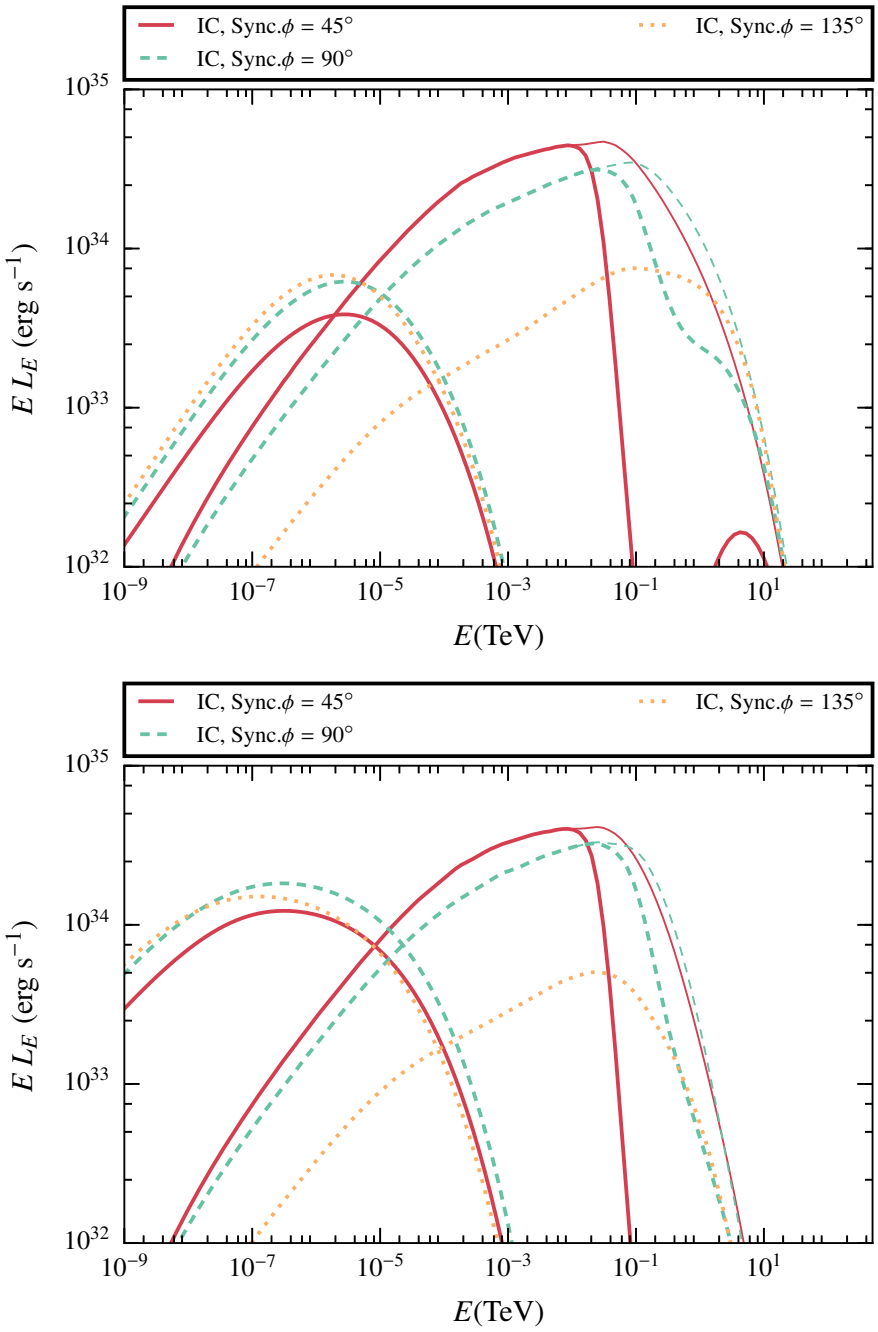

Figure 4.5: Same as Fig. 4.4, but for the small clump scenario ($\chi = 10$, $R_c = 8 \times 10^{10}$ cm).

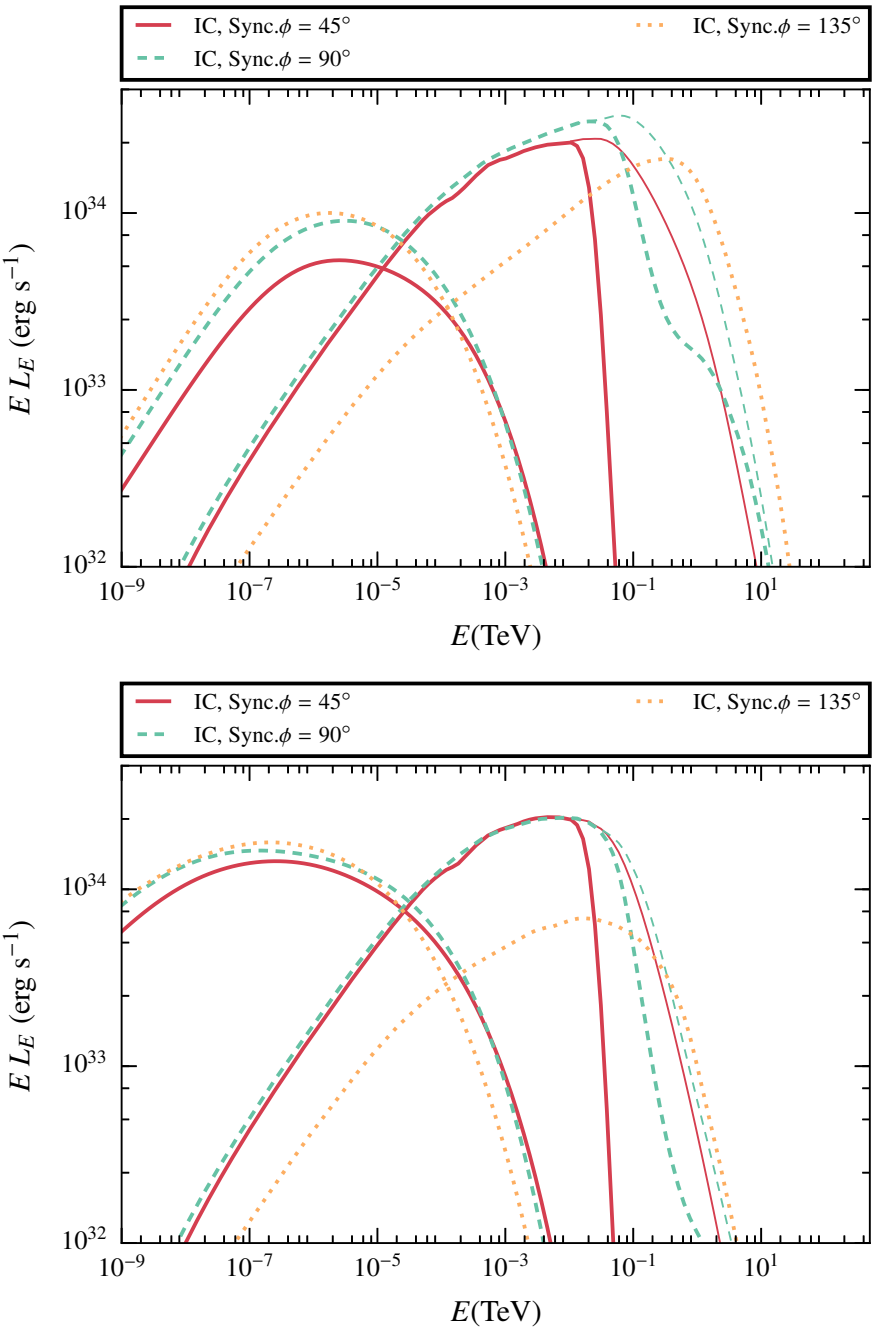

Figure 4.6: Same as Fig. 4.4, but for the large clump scenario ($\chi = 10$, $R_c = 4 \times 10^{11}$ cm).

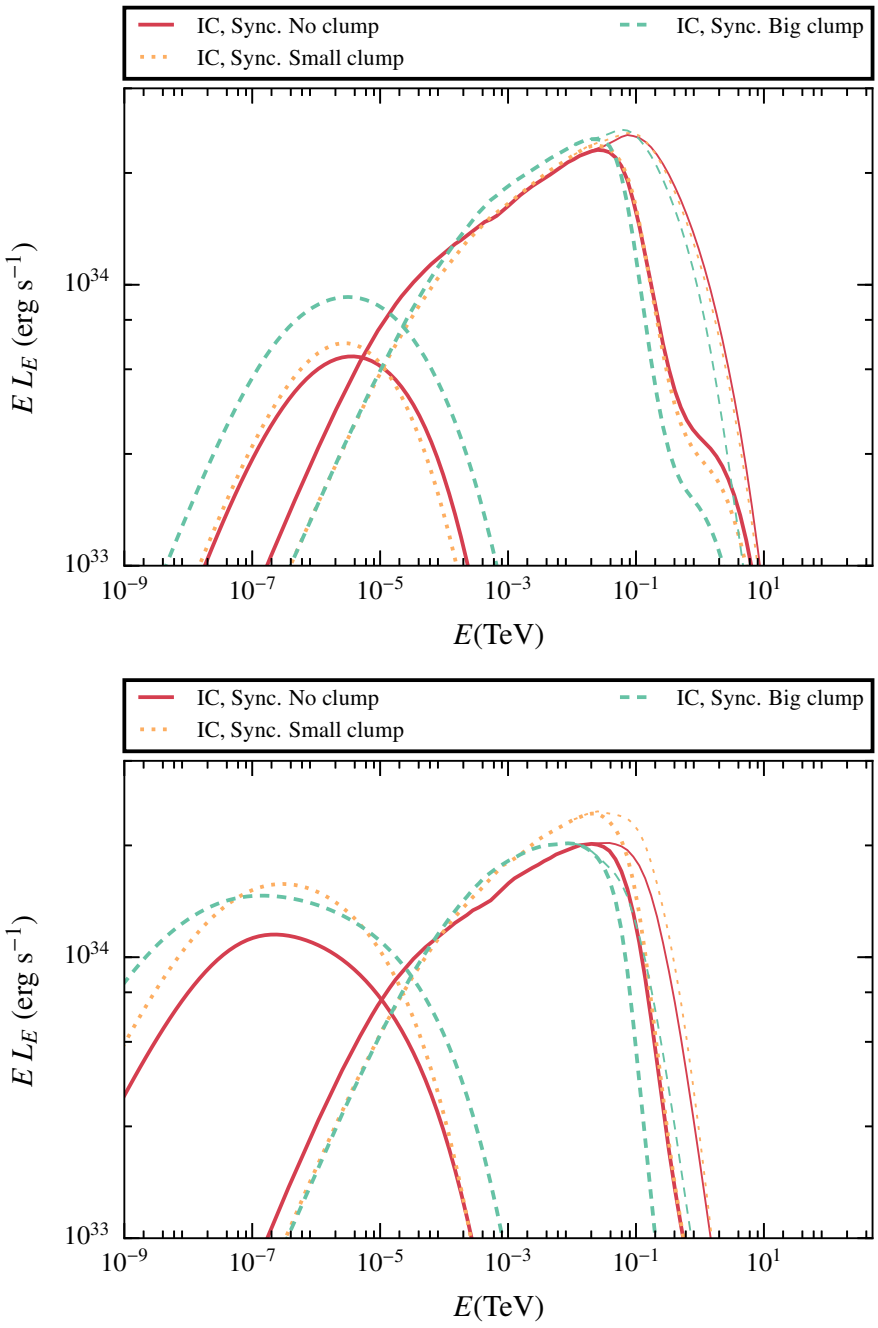

Figure 4.7: Spectral energy distribution of synchrotron and IC for $\phi = 90°$, in the low ($\chi_B = 10^{-3}$) and high ($\chi_B = 0.1$) magnetic field cases (top and bottom pannels, respectively).

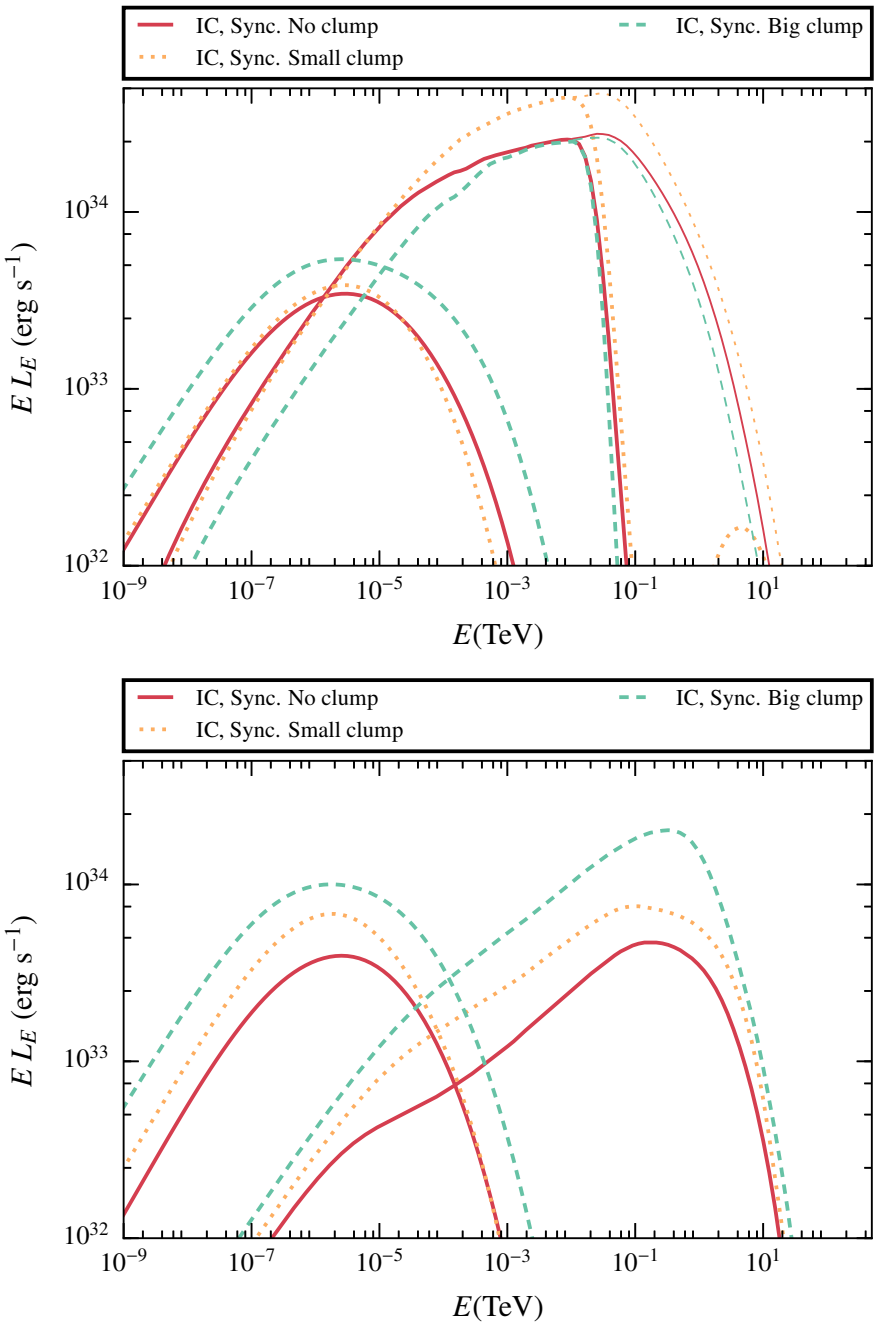

Figure 4.8: Spectral energy distribution of synchrotron and IC for a fixed magnetic field (low case, $\chi_B = 10^{-3}$) and different ϕ-values: 45 and 135° (top and bottom pannels, respectively).

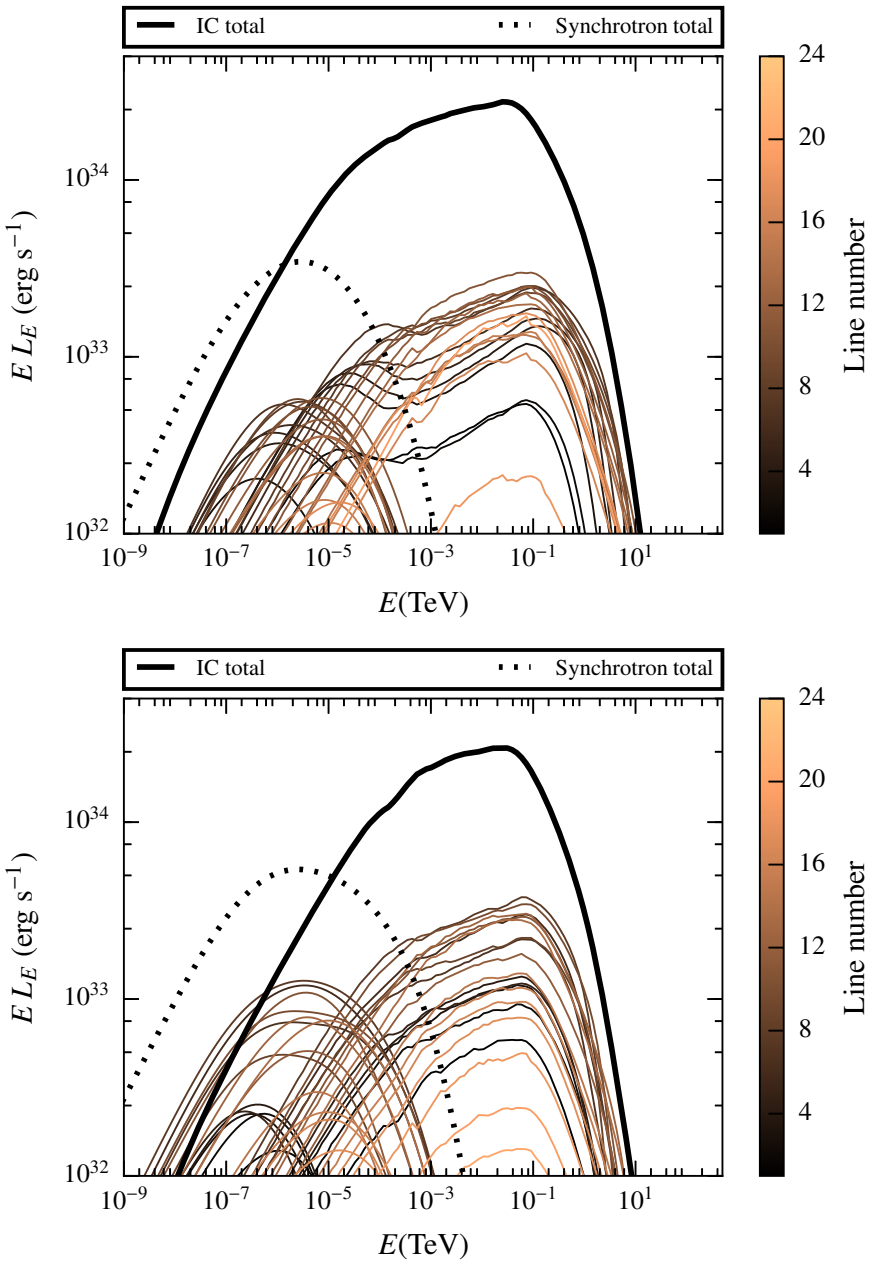

Figure 4.9: Contribution of each streamline (numbered as in top panel of Fig. 4.1) to the overall synchrotron (dotted line) and IC (solid line) SED. The no clump (top) and the large clump (bottom) scenarios are both computed for a low magnetic field ($\chi_B = 10^{-3}$) and $\phi = 90°$.

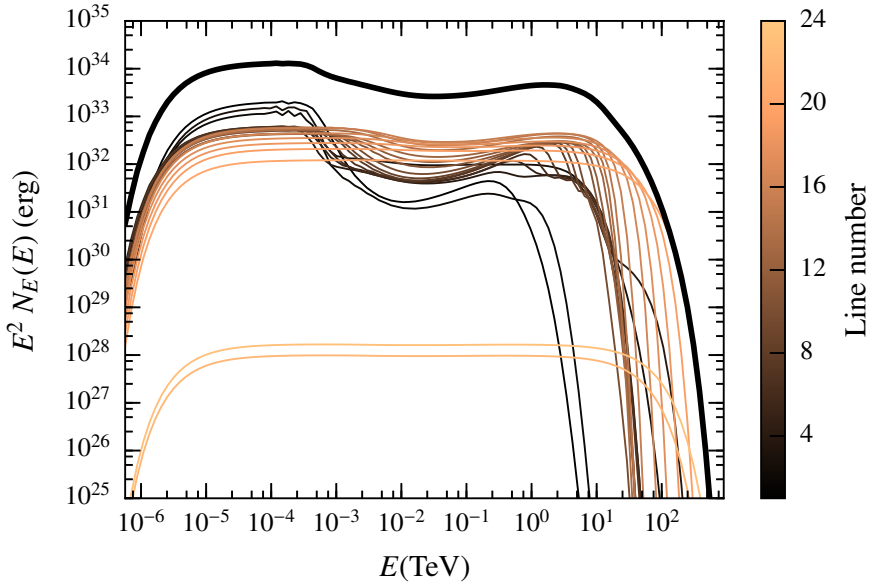

Figure 4.10: Particle energy distributions for the different streamlines (thin lines) and the sum of all of them (thick black line) in the LF, for the low magnetic field ($\chi_B = 10^{-3}$) no clump scenario.

Doppler boosting is a very important factor characterizing the observer synchrotron and IC luminosities (by δ^4), and to a lesser extent spectra through photon energy boosting (by δ), in the scenario studied here. Doppler boosting has been already discussed (e.g. Khangulyan et al., 2008; Dubus et al., 2010a; Kong et al., 2012; Khangulyan et al., 2014a; del Palacio et al., 2015; Dubus et al., 2015) in the framework of a homogeneous stellar wind; in this context we obtain similar results, as Doppler boosting induces luminosity variations of up to a factor of a few by comparing different viewing angles in certain bands (see Table 5.1, no clump scenario). Radiation enhancement in the cases computed here is well illustrated by the maps presented in the right panels of Figs. 4.1, 4.2, and 4.3. For comparison, the impact of clump absence/presence is also shown in the left panel of Figs. 4.1, 4.2, and 4.3 for the general direction of the streamlines. for the shocked pulsar wind speed distribution. The effects on radiation are seen in the SEDs and maps shown in Figs. 4.11 and 4.12 (and again in Table 5.1, comparing the same energy bands and ϕ values for the three cases).

If the stellar wind is homogeneous, the two-wind interaction structure is already prone to suffer hydrodynamical instabilities (e.g. Bosch-Ramon et al., 2012b; Lamberts et al., 2013; Paredes-Fortuny et al., 2015; Bosch-Ramon et al., 2015), i.e. the tinniest irregularities in the wind act as inho-

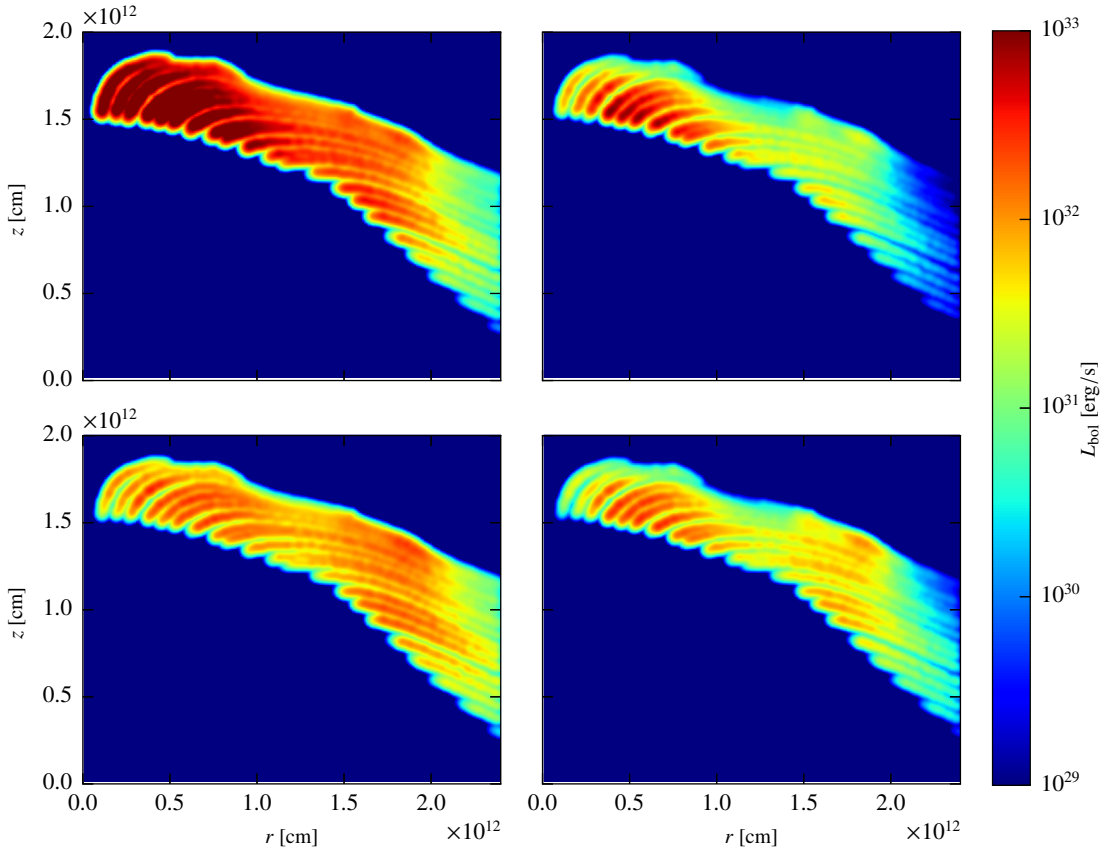

Figure 4.11: Maps of the bolometric luminosity per cell for the no clump scenario, taking a low magnetic field $\chi_B = 10^{-3}$. Top panels: Map in the rz-plane of the distribution of IC (left) and synchrotron (right) for $\phi = 45°$. Bottom panels: Same as the top panels, but for $\phi = 135°$.

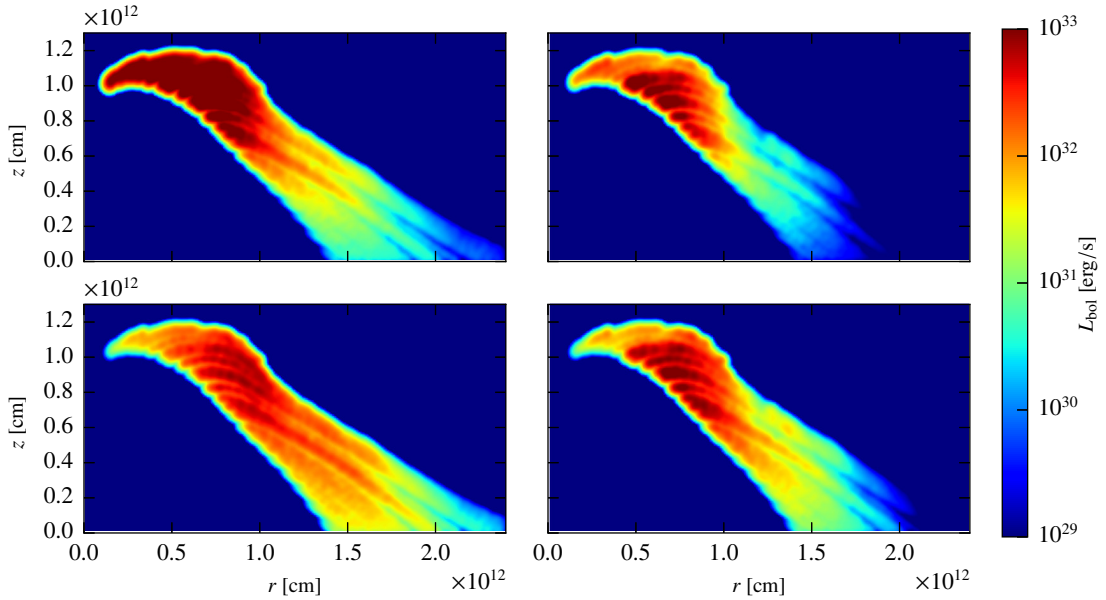

Figure 4.12: Maps of the bolometric luminosity per cell, for the large clump scenario, taking a low magnetic field $\chi_B = 10^{-3}$. Top panels: IC (left) and synchrotron radiation (right) for $\phi = 45°$. Bottom panels: Same as the top panels, but for $\phi = 135°$.

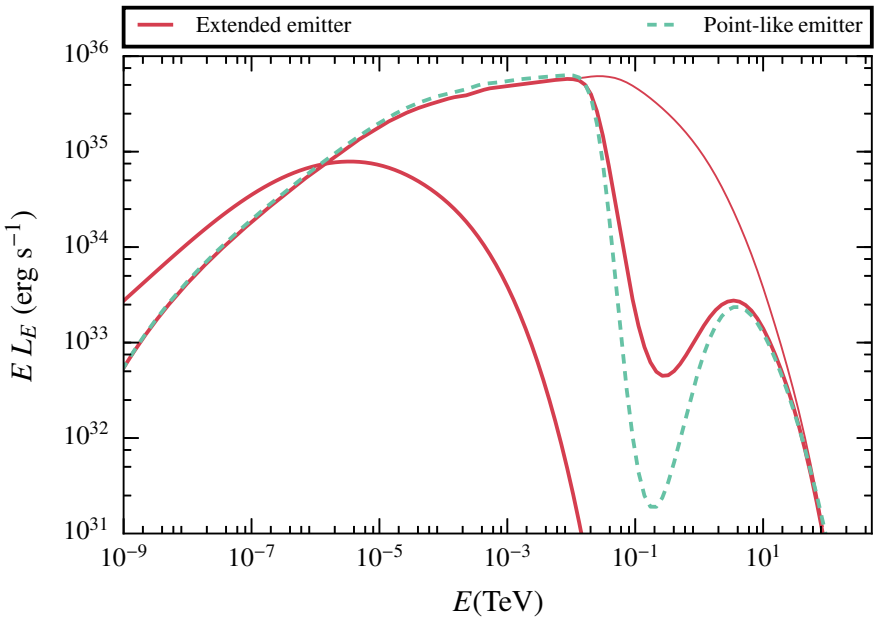

Figure 4.13: Spectral energy distribution of the synchrotron and IC emission in the no clump scenario, with $\phi = 45°$ and $\chi_B = 10^{-3}$. The emission for the computed emitter geometry (solid line) and that obtained assuming that the emitter is point-like (dashed line) are shown. The lower energy component corresponds to synchrotron emission.

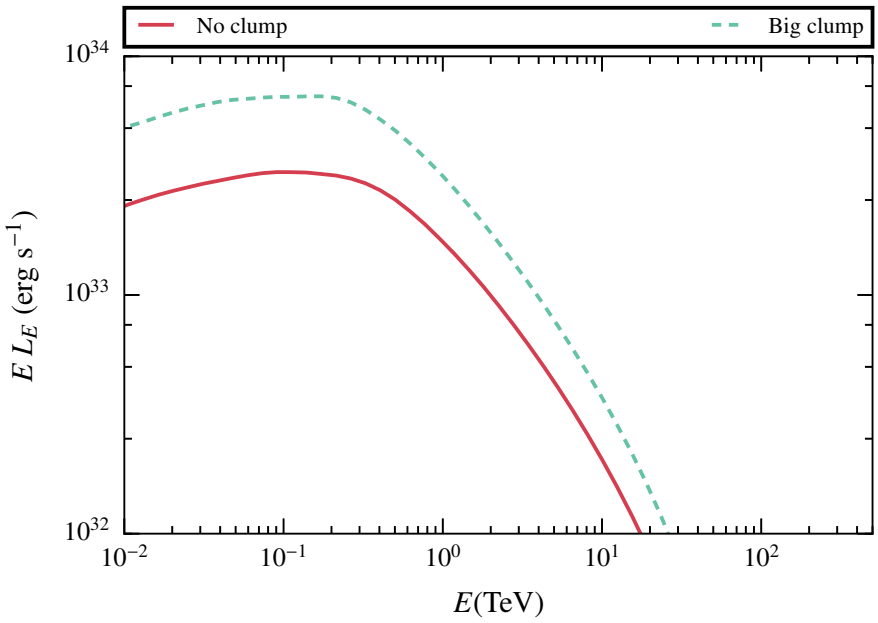

Figure 4.14: Comparison of the spectral energy distribution for the steady and the large clump case adapting the hydrodynamical results to the case of PSR B1259 – 63around 20 days after periastron, roughly at the second disc passage.

mogeneity seeds. The corresponding dispersion in the velocity field coupled with Doppler boosting can thus introduce a chaotic variability component to the emission even in the absence of clumps. Therefore, even rather small clumps enhance instability formation and growth, making the emission variability more complex.

It is interesting to compare the cases without and with a small clump in Table 5.1 for the same viewing angle. In these two cases, the overall two-wind interaction structure does not change significantly, and the flux difference is determined by the perturbations in the flow velocity. This already leads to luminosity variations of almost a factor of ~ 2 in certain bands. Large clumps add perturbations to the shocked flow structure, and also change the overall distribution of the streamline directions as the shock approaches the pulsar significantly. This induces a characteristic pattern, with its evolution determined by the shocked clump dynamics. We note that in the more realistic case of using a 3D simulation to compute the emission, the lack of symmetry in the azimuthal direction with respect to the pulsar-star axis would likely lead to an even more chaotic velocity field, and thus to stronger differences between clump scenarios.

It is worth noting that the shock becomes more perpendicular when approaching the pulsar in the large clump case. Therefore, the transfer of energy to non-thermal particles is increased, and thus the clump presence enhances particle acceleration at the pulsar wind shock, as shown by the injected luminosity into non-thermal particles, which in the large clump case is $\sim 50\%$ larger than without a clump (see Sect. 4.3.2). However, this effect may be difficult to disentangle from Doppler boosting in the radiation results. Also, if magnetic field reconnection plays a sensible role in particle acceleration, chaotic perturbations of the magnetic field structure induced by clumps may have a strong impact on the particle acceleration (Sironi and Spitkovsky, 2011).

From a direct application of our radiation calculations using hydrodynamical information about the post-periastron GeV flare, and the post-periastron disc crossing in TeV, in PSR B1259 – 63, twe see that the former is hard to reproduce in our simplified scenario, whereas the second semi-quantitatively agrees with our results.

4.5 FINAL REMARKS

This chapter provides some illustrative examples of how different types of clumps can affect the emitting region and the radiation itself in the case of an inhomogeneous stellar wind interacting with a pulsar wind. The studied effects (clump presence, velocity field dispersion, Doppler boosting for a given observer, instability development, magnetic field increase, and closing of the pulsar wind shock) acting together can either cancel out to some extent or combine rather unpredictably. There are also many different timescales, as instability growth, region shrinking, and magnetic field growth depend on the clump evolution timescale, which itself depends to first order on the clump size and density. On the other hand, the shocked pulsar wind flow can change direction much more quickly, and the rapidly changing, non-uniform, beaming of radiation in the emitting region is an important factor shaping variability. One can thus conclude that flares could occasionally be seen in some or all bands of the spectrum, with their duration determined by the dominant variability origin, whereas in general emission may vary more smoothly. There are periodic emission features in the systems studied that originate in repetitive physical phenomena (e.g. orbit-related IC, orbit-related Doppler boosting, pair creation angular effects, changes in radiative and non-radiative cooling along the orbit, etc.), but non-periodic variability originates from a com-

bination of different, equally important, factors, and they can be hard to disentangle. A study of the X-ray light curve can provide information on the different processes shaping the non-thermal emission. We note that Kishishita et al., 2009 have found that the X-ray light curve of the pulsar binary candidate LS 5039 in the years 1999–2007 was rather stable, with even fine structures such as spikes and dips similar from one orbit to another. This non-chaotic behaviour, if confirmed, would not be explained by the processes discussed in this thesis.

A quantitative assessment of the importance of the different factors in the clump wind scenario is the next step to be carried out. The reason is that the shocked pulsar wind accelerates as it propagates (e.g. Bogovalov et al., 2008), and it does so in parallel with instability growth. Therefore, a quantitative prediction of the impact of instability growth on the emission, induced either by small perturbations or large clumps, requires a larger computational grid to properly capture all these processes. Multiple clump interactions should be also simulated. In this regard, a stellar wind with a distribution of clump properties (e.g. Moffat, 2008) is likely to be an additional variability source affecting the non-linear hydrodynamical processes occurring in the two-wind interaction structure. Finally, the dynamical role of the magnetic field cannot be forgotten if the pulsar wind is weakly magnetized, as the flow magnetization may significantly grow in specific regions of the shocked pulsar wind (see e.g. Fig. 6 in Bogovalov et al., 2012)[3]. This growth can be important enough to moderate the development of hydrodynamical instabilities, or induce anisotropy and thus further complexity to their development.

If non-thermal radiation losses were to be accounted for (say $\eta_{\rm NT} \lesssim 1$) when modelling the properties of the shocked pulsar wind, full radiation-(magneto)hydrodynamic simulations should be carried out. We must point out though that, in addition to this effect, it is also necessary to account for the fact that IC emission on stellar photons is already anisotropic in the FF. This anisotropy in the FF implies that there will be momentum lost in the direction of the star, a form of Compton rocket (e.g. Odell, 1981). Thus, if IC radiation is important for the flow internal (non-thermal) energy losses, its dynamical impact will also be important for the emitting flow through the loss of momentum in specific directions. Synchrotron emission may also be anisotropic if the magnetic field is ordered, but unless the field presents a strong gradient emission by particles moving in

3 Although the general impact for a moderate magnetization value was found to be negligible in that work.

opposite directions along the field lines would effectively cancel the momentum loss out.

5

CLUMPY WIND-JET INTERACTIONS IN HIGH-MASS MICROQUASARS

5.1 INTRODUCTION

High-mass microquasars (HMMQs) are binary systems hosting a massive star, and a compact object able to produce jets in which HE processes can take place (see, e.g., Bosch-Ramon and Khangulyan, 2009; Dubus, 2013; Bednarek, 2013, and references therein). To date, gamma rays have been robustly detected from two HMMQs, Cyg X-3 and Cyg X-1 (Tavani et al., 2009; Zanin et al., 2016, respectively). Variability of the detected emission indicates that the high-energy source should be located relatively close to the compact object, at a distance comparable to the binary separation distance (Dubus et al., 2010b; Zanin et al., 2016). There is a tentative detection of another HMMQ, SS 433, although in this case the emission would be likely coming from the jet-termination region (Bordas et al., 2015).

The energies at which Cyg X-1 and Cyg X-3 were detected are in the GeV range, except for a flare-like detection of Cyg X-1 with the Major Atmospheric Gamma Imaging Cherenkov Telescopes (MAGIC) Cherenkov telescope in the TeV range with post-trial significance of 4.1σ (Albert et

al., 2007). Both sources present long-term gamma-ray emission, overlapping with possible day-scale flares, all associated with jet activity (Albert et al., 2007; Tavani et al., 2009; Fermi LAT Collaboration et al., 2009; Sabatini et al., 2010; Malyshev et al., 2013; Bodaghee et al., 2013; Zanin et al., 2016; Zdziarski et al., 2016b,a). In what follows, we will carry a mixed approach considering HMMQs in general, while adopting Cyg X-1 and Cyg X-3 as reference sources to check our results in the context of real objects.

Massive stars produce dense and fast winds that are thought to be inhomogeneous (e.g. Runacres and Owocki, 2002; Moffat, 2008; Puls et al., 2008, and references therein). The specific properties of these inhomogeneous winds may depend on the stellar type and evolutionary phase, but in general they can be described in terms of dense clumps in a dilute medium. In particular, Cyg X-1 hosts a black hole and an O-type supergiant, and Cyg X-3 either a neutron star or a black hole, and a Wolf-Rayet star, and clumpy winds have been suggested to be present in both systems (see, e.g. Szostek and Zdziarski, 2008; Rahoui et al., 2011; Miškovičová et al., 2016).

Detection of gamma-ray emission from galactic jet sources requires efficient particle acceleration, which is conventionally associated with shocks. The propagation of a jet through the binary system environment may come along with the formation of shocks at binary scales in addition to the jet termination shock. For example, internal shocks form when portions of jet material, moving with different velocities, collide to each other (e.g. Bosch-Ramon et al., 2006). Furthermore, the stellar wind lateral impact should produce asymmetric recollimation shocks and induce non-thermal emission (e.g. Romero et al., 2003; Perucho and Bosch-Ramon, 2008; Dubus et al., 2010a; Yoon et al., 2016). But it cannot be neglected that when wind density inhomogeneities or clumps penetrate inside the jets, they should trigger strong shocks as well. Thus, the wind clumps in HMMQs may have a significant influence on the jet dynamics (Perucho and Bosch-Ramon, 2012) and on the non-thermal HE processes occurring on the scales of the binary system (Owocki et al., 2009; Araudo et al., 2009; Romero et al., 2010). Therefore, despite all these shocks can be sites of efficient particle acceleration and HE emission, one expects the strongest kinetic-to-internal energy conversion for shocks associated with wind clumps present inside the jet (Bosch-Ramon, 2015). Moreover, besides this high-conversion efficiency, the Doppler boosting of the non-thermal emission associated with wind clumps, in addition to being important, might be also favourable for relatively off-axis observers.

In this chapter, we present numerical calculations of the HE emission produced by a clump-jet interaction in a HMMQ using the hydrodynamical information obtained from a simplified relativistic, hydrodynamical (RHD) axi-symmetric simulation of such an interaction. Particle acceleration is assumed to occur in the jet shock, as this is much more energetic than the one initially crossing the clump. The parameters adopted have been chosen such that the simulation can be taken as a reference case, i.e. a clump of realistic parameters being inside the jet at a typical interaction jet height, similar to the binary size. Interactions taking place significantly closer, or farther, from the jet base, would be either very unlikely, or too oblique for the clump to penetrate into the jet (see Eq. 5.1). Therefore, the calculations performed can be used as a reference to establish the typical radiation outcome from one interaction, choosing also suitably the orbital phase, although some of the results have been checked for different orbital phases. The radiation results can be then generalized to the realistic case of multiple wind clumps interacting with the jet, adopting a phenomenological prescription for the inhomogeneous wind properties, similarly to what was done in Bosch-Ramon, 2013 in the context of a high-mass binary hosting a young pulsar.

5.2 CLUMP-JET INTERACTION: BASIC ESTIMATES

In this section we present the analytical study of the main characteristics of a clump-jet interaction, and show that even for conservative assumptions it is likely that clumps penetrate the jet. This part of the work was done by our collaborators, but is presented here to give context to the NT calculations. The following quantities are required for the analysis: (i) the stellar mass-loss rate ($\dot{M}_{\rm w}$), wind velocity ($v_{\rm w}$), and wind density ($\rho_{\rm w}$); (ii) the jet luminosity (without accounting for the rest-mass energy; $L_{\rm j}$), velocity ($v_{\rm j}$, or Lorentz factor $\Gamma_{\rm j}$), radius ($R_{\rm j}$), height ($z_{\rm j}$), density ($\rho_{\rm j}$), and jet half opening angle ($\theta_{\rm j} = R_{\rm j}/z_{\rm j}$); (iii) the clump characteristic radius ($R_{\rm c}$), and density ($\rho_{\rm c}$) (assuming spherical uniform clumps), which relates to the average wind density through the density contrast or clumping factor ($\chi = \rho_{\rm c}/\rho_{\rm w} > 1$); and finally (iv) the distance between the star and the base of the jet, or orbital separation distance ($R_{\rm orb}$). In this work, the jet is assumed to be perpendicular to the orbital plane. We also consider a mildly relativistic jet (see Sect. 2 in Bosch-Ramon and Barkov 2016), with $\Gamma_{\rm j} = 2$. The hydrodynamic approximation for the clump-jet interaction is

adopted, as the gyroradii of the particles involved are much smaller than the typical size of the interacting structures.

We consider the emission of a clump interacting with the jet at a distance from the jet base similar to $R_{\rm orb}$. On these scales, clump-jet interactions are more numerous because the jet is thicker; the jet is also more dilute than further upstream, and the clump velocity is still rather perpendicular to the jet, favouring jet penetration. Moreover, at smaller distances from the compact object, the jet ram pressure is too strong for the clumps to survive penetration. For high density contrast values, i.e. $\chi \gg 1$, wind-jet interactions may occur just through clumps entering into the jet. In that case, the clumps would be surrounded by a very dilute, hot medium of little dynamical impact either for the jet, or the clumps. We adopt here however the more conservative assumption that, even if $\chi \sim 10$, the wind interacts with the jet forming a relatively smooth region of shocked material that circumvents the jet (see Perucho and Bosch-Ramon 2012; see also Pittard 2007 in the context of colliding wind binaries). This shocked wind can prevent small clumps from reaching the jet, which sets the first condition for clump-jet interaction to occur. Moreover, the impact of the jet in a clump generates a shock that propagates in the latter, eventually destroying it. Therefore, a second condition is that the forward shock in the clump is slower than the clump velocity perpendicular to the jet, to allow the clump to enter deep enough into the jet before its destruction (see, e.g. Araudo et al., 2009).

To formalize the first condition, let us consider a clump that travels with velocity $\sim v_{\rm w}$ perpendicular to the jet and reaches the region where the wind interacts with the jet boundary. To successfully penetrate the jet, the clump has to go through the shocked wind, with respect to which the clump is moving also at $\sim v_{\rm w}$, without significantly slowing down. Such a region has a thickness $\sim R_{\rm j}$ and exerts a drag on the clump that can be quantified through a ram pressure $P_{\rm w} \sim \rho_{\rm w} v_{\rm w}^2$. The acceleration exerted on the clump, which has a characteristic surface $s_{\rm c} \sim \pi R_{\rm c}^2$ and volume $V_{\rm c} \sim 4/3\, s_{\rm c} R_{\rm c} \sim s_{\rm c} R_{\rm c}$, by this pressure is $a_{\rm acc} \sim s_{\rm c} P_{\rm w}/m_{\rm c}$. Using that $m_{\rm c} = V_{\rm c}\rho_{\rm c}$, $V_{\rm c}/s_{\rm c} \sim R_{\rm c}$, and $\rho_{\rm c} = \chi\rho_{\rm w}$, one can obtain the expression: $a_{\rm acc} \sim P_{\rm w}/(\chi\rho_{\rm w}R_{\rm c})$. Therefore, the typical distance required to significantly slow down the clump in the shocked wind surrounding the jet is $l \sim v_{\rm w}^2/a_{\rm acc} \sim \chi R_{\rm c}$, which as noted above should be $l \gtrsim R_{\rm j}$, and therefore $R_{\rm c} \gtrsim R_{\rm j}/\chi$, setting a lower limit on the clump size:

$$R_{\rm c} > R_0 = 3\times10^{10}\left(\frac{\theta_{\rm j}}{0.1}\right)\left(\frac{10}{\chi}\right)\left(\frac{R_{\rm orb}}{3\times10^{12}\,{\rm cm}}\right){\rm cm}. \quad (5.1)$$

The second condition for clumps to fully penetrate into the jet at $z_j \lesssim R_{orb}$ is $v_{sh} \lesssim v_w$ [1], where v_{sh} is the velocity of the shock produced within the clump by the jet impact. For a cold jet, its pressure P_j is dominated by the kinetic component of the momentum flux, i.e. $P_j \sim \Gamma_j^2 \rho_j v_j^2$. Assuming equilibrium between the jet ram pressure and shocked clump pressure, we obtain $v_{sh} \sim (P_j/\rho_c)^{1/2} \sim \Gamma_j (\rho_j/\rho_c)^{1/2} v_j$. Considering that

$$\rho_j = \frac{L_j}{\pi R_j^2 \Gamma_j (\Gamma_j - 1) v_j c^2}, \tag{5.2}$$

$$\rho_c \sim \frac{\chi \dot{M}_w}{4\pi R_{orb}^2 v_w}, \tag{5.3}$$

and fixing $z_j \sim R_{orb}$, i. e. $R_j \sim \theta_j R_{orb}$, one gets the following limitation for the jet power:

$$L_j \lesssim 1.4 \times 10^{37} \left(\frac{\Gamma_j - 1}{\Gamma_j}\right)\left(\frac{\chi}{10}\right)\left(\frac{\dot{M}_w}{3 \times 10^{-6} M_\odot \mathrm{yr}^{-1}}\right) \left(\frac{\theta_j}{0.1}\right)^2 \left(\frac{v_w}{10^8 \mathrm{cm\,s^{-1}}}\right)\left(\frac{v_j}{c}\right)^{-1} \mathrm{erg\,s^{-1}}. \tag{5.4}$$

For a hot jet, the specific enthalpy should be included to derive P_j.

For the typical parameters of Cyg X-3 and Cyg X-1 (see Yoon et al., 2016; Bosch-Ramon and Barkov, 2016, and references therein), and adopting $\chi \sim 10$ and $\Gamma_j \sim 2$, clumps will be able to penetrate into the jets of these HMMQ for $R_c \sim 3 \times 10^9$ and 3×10^{10} cm, and $L_j \lesssim 10^{38}$ and 10^{37} erg s^{-1}, respectively. These jet powers are actually similar to the values estimated for these sources, although the uncertainties in the clumpy wind and the jet properties are large.

5.3 CLUMP-JET INTERACTION: NUMERICAL CALCULATIONS

5.3.1 *Hydrodynamics*

The clump-jet interaction was simulated in two dimensions (2D) assuming axisymmetry, i.e. neglecting the clump motion with respect to, say, the compact object frame, and a dynamically negligible magnetic field. In this case the code is the same as the one used in Bosch-Ramon, 2015, but the

1 A more precise relation is $v_{sh} < v_{w\perp}$, but for simplicity in this analysis we assume that $v_{w\perp} \sim v_w$ in the regions of interest.

spatial reconstruction scheme has been improved from 2nd to 3rd order applying the piecewise parabolic method reconstruction scheme (Colella and Woodward, 1984; Martí and Müller, 1996; Mignone et al., 2005).

The resolution of the calculations is 300 cells in the vertical direction, the z-axis, and 150 in the radial direction, the r-axis, and the physical size is $z_{\rm grid}^{\rm max} = 9\times10^{11}$ cm in the z-direction, and $r_{\rm grid}^{\rm max} = 4.5\times10^{11}$ cm in the r-direction. The resolution was chosen such that no significant differences could be seen in the hydrodynamical results when going to higher resolution simulations. Inflow conditions (the jet) are imposed at the bottom of the grid, reflection at the axis, and outflow in the remaining grid boundaries. On the scales of the grid, for simplicity we approximate the jet streamlines at injection as oriented along the z-direction despite the jet is actually assumed to be conical.

The injected jet power without accounting for the jet rest-mass energy is $\approx 2.3\times10^{37}$ erg s^{-1} for the whole grid, up to $r_{\rm grid}^{\rm max}$, with a Lorentz factor $\Gamma_{\rm j} = 2$. The initial clump radius is $R_{\rm c} = 3\times10^{10}$ cm, and its density, $\rho_{\rm c} \approx 5\times10^{-14}$ g cm^{-3}. This density would correspond to that of a clump located at $z_{\rm j} \approx 3\times10^{12}$ cm, for a stellar wind with $\dot{M} \approx 3\times10^{-6}$ M$_\odot$ yr^{-1}, $v_{\rm w} \approx 2\times10^{8}$ cm s^{-1}, and $\chi \approx 10$ (plus $R_{\rm orb} = 3\times10^{12}$ cm). The initial clump location in the grid is $(0, 10^{11}\,{\rm cm})$.

With the jet impact, the clump gets shocked, expands, disrupts, and eventually leaves the grid (see, e.g., Bosch-Ramon, 2012, in the context of extragalactic jets). The whole duration of the simulation was ≈ 820 s. Five snapshots of the density distribution, illustrating the clump evolution after ≈ 73, 521, 596, 708, and 822 s, are presented in Fig. 5.1. The shocked jet material is seen in light blue, forming a sort of cometary tail pointing upwards and surrounding the clump shocked material, red with green borders.

The grid size has been chosen such that the simulation captures the first stages of the clump-jet interaction. This is enough to compute the non-thermal emission for two typical instances of the shocked clump evolution: (i) a quasi-stationary shock in the jet flow is present, but the clump has not expanded, nor it has been displaced, due to the jet impact; (ii) the clump has already expanded, disrupted, and moved along the jet axis. A simulation with a significantly larger computational grid, and a much longer simulated time, is required for an accurate description of the clump-jet interaction until the clump has reached an asymptotic speed (and probably fully fragmented and spread in the jet), i.e. when no shock is present in the jet flow or it is much weaker. This should not

affect qualitatively the high-energy emission predictions, but quantitative differences are expected. An accurate study of this (clump-jet mixing, lightcurves, etc.) is left for future work. The presence of the magnetic field, or 3D calculations, are likely to introduce further complexity to the problem through effects such as suppression, anisotropy, or enhancement, of the growth of instabilities. These effects should be thoroughly studied through devoted simulations, although such an investigation is out of the scope of the present thesis and left for the future. Other effects may be included also for accuracy, as a more realistic equation of state, or the back-reaction effects of non-thermal processes in the (magneto)hydrodynamics.

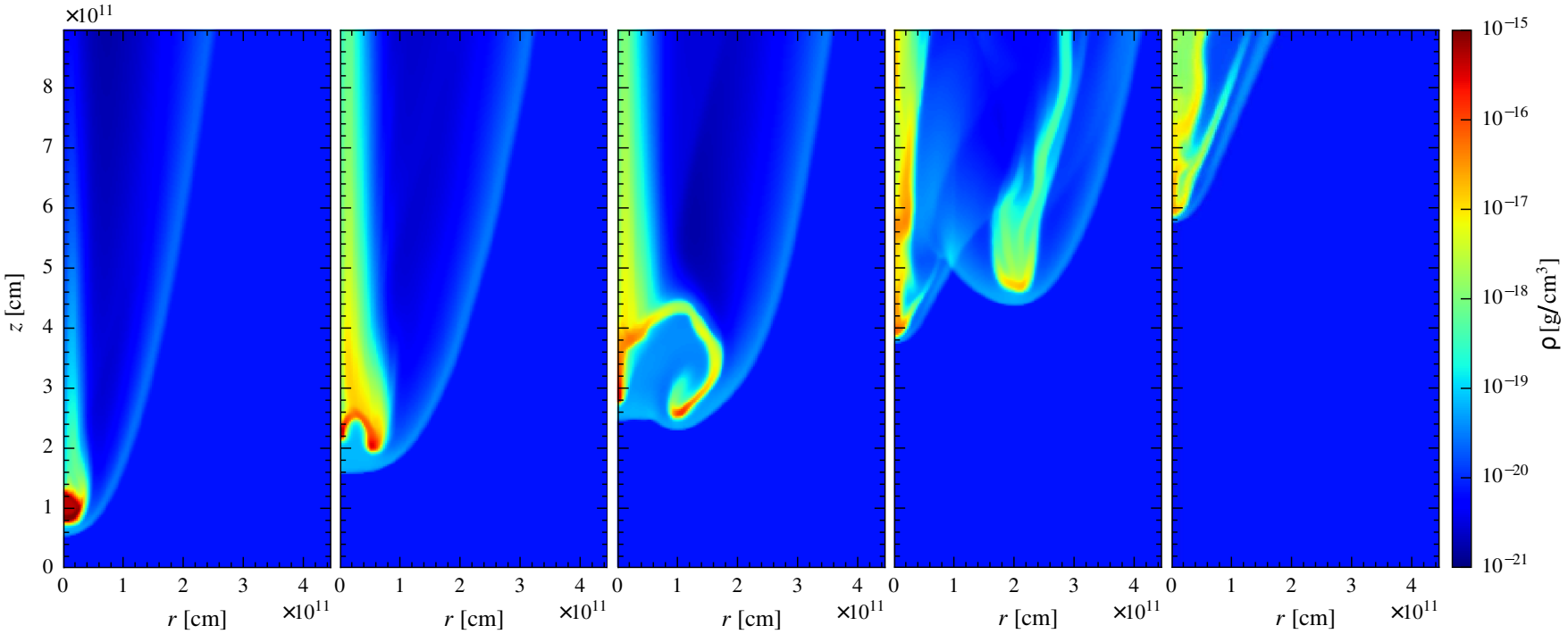

Figure 5.1: Density maps of the clump-jet interaction simulation that illustrate the clump evolution after ≈ 73, 521, 596, 708, and 822 s (or, equivalently, to ≈ 0.5, 3.5, 4.1, 4.8, and 5.6 in R_c/v_{sh} units).

5.3.2 *Radiation results*

To compute the injection, evolution and radiation of the non-thermal particles, we need to model the shocked jet flow as a set of streamlines, as described in Sect. 2.1.1. With this information we can compute the evolution of the NT particles, adopting two different values for the ratio of Poynting-to-matter energy flux $\chi_B = 10^{-3}$ and 1 (see Eq. 2.5). Note that the latter value is formally inconsistent with the hydrodynamical assumption of the simulations, but we still consider this case useful, as it approximately sets a lower limit on the IC with respect to the synchrotron emission.

For simplicity, we consider in what follows the radiation results for a typical orbital phase: assuming a circular orbit, we considered an orbital phase right in the middle between inferior and superior conjunction, i.e., the compact object is in the plane of the sky. This provides a sort of typical high-energy SED. A more detailed analysis of the overall spectra in the different explored cases, and for different orbital phases, is out of the scope of this thesis and left for future work, as we are interested here in the average behavior when the jet is present. We are also mostly interested in the 0.1–100 GeV band luminosity because this band is not strongly sensitive to parameters such as the maximum particle energy, and reacts smoothly to magnetic field and system-observer orientation changes, whereas the TeV band is very sensitive to all these factors through IC effects and gamma-ray absorption (e.g. Bosch-Ramon and Khangulyan, 2009, gamma-ray absorption is included in the present work). The GeV luminosity is also available for Cyg X-1 and Cyg X-3, as these sources have been detected in this energy band. For low-to-moderate B-values, this band is also a good proxy for the source energetics and, unlike X-rays, is certainly of non-thermal nature.

Two illustrative stages of the clump evolution are considered when presenting the results of our computations: (i) the first stage, when the clump is compressed by the jet ram pressure (hereafter called compression phase), the longest and more stable phase of the clump evolution; and (ii) a later, shorter stage when the clump is disrupted (hereafter called disruption phase), presenting a larger shock and therefore higher non-thermal emission; both stages are shown in Fig. 5.1, first and third panels starting from the left. We also present in Fig. 5.4 the SEDs of all 5 snapshots of the hydrodynamical flow shown in Fig. 5.1. This illustrates how the high-energy emission varies with the clump evolution. The disruption phase is chosen as the maximum luminosity snapshot among those

computed (i.e. number 3). From the point of view of the hydrodynamics, snapshot number 4 is characterized by a largest cross-section of the shocked jet, but the apparent non-thermal luminosity is higher for the hydrodynamic configuration shown in snapshot 3. This is likely related to a reduced Doppler boosting caused by streamline stronger deflection in 4; also, some additional weakening of the emission can be caused by the limited grid size.

In the three panels of Fig. 5.6, we first focus on the compression phase and vary B, and then we compare the compression and disruption phases. It can be seen that, in the case of a weak magnetic field, the transition from the compression to the disruption phase is accompanied by a flux increase by a factor of ~ 5. In the high B case, the emission enhancement is modest, within a factor of two.

To illustrate the importance of the radiation losses, we can compare the energy injected per time unit in the form of non-thermal particles with that leaving the computational grid, after suffering energy losses, in the laboratory frame. For the compression phase, the total injected luminosity is $\approx 1.6\times10^{35}\,(\eta_{\rm NT}/0.1)$ erg s^{-1} and about 33% of the energy is kept by the particles when leaving the grid in the low B case, being this percentage smaller ($\approx 15\%$) for the high B case. In that stage, particles lose a $\approx 49\%$ of the injected energy through adiabatic losses, which means $\approx 7.7\times10^{34}$ erg s^{-1}; the synchrotron+IC losses are $\approx 19\%$ of the injected energy in the low B case, which means $\approx 3\times10^{34}$ erg s^{-1} ($\approx 36\%$ and $\approx 5.8\times10^{34}$ erg s^{-1} in the high B case). In the disruption phase, the total injected luminosity is $\approx 10^{36}\,(\eta_{\rm NT}/0.1)$ erg s^{-1}. In that stage, particles actually gain energy through adiabatic heating as in some streamlines the flow is compressed, approximately $\approx 2\times10^{35}$ erg s^{-1} ($\approx 20\%$ of the injected energy); the synchrotron+IC losses are $\approx 50\%$ of the injected energy in the low B case, which means $\approx 5\times10^{35}$ erg s^{-1} ($\approx 95\%$ and $\approx 9.5\times10^{35}$ erg s^{-1} in the high B case). For the sake of discussion (see Sect. 5.5), we provide in Table 5.1 the integrated luminosity in the range 0.1–100 GeV for the different cases studied here: the compression and disruption phases, for the low and the high B cases, and $\phi_{\rm obs} = 30°$, given that this observing angle may be representative of both Cyg X-1 and Cyg X-3.

5.4 COLLECTIVE EFFECTS OF A CLUMPY WIND

Clumping is universal in massive star winds: these winds are stochastically inhomogeneous, believed to be composed by a hierarchy of clumps,

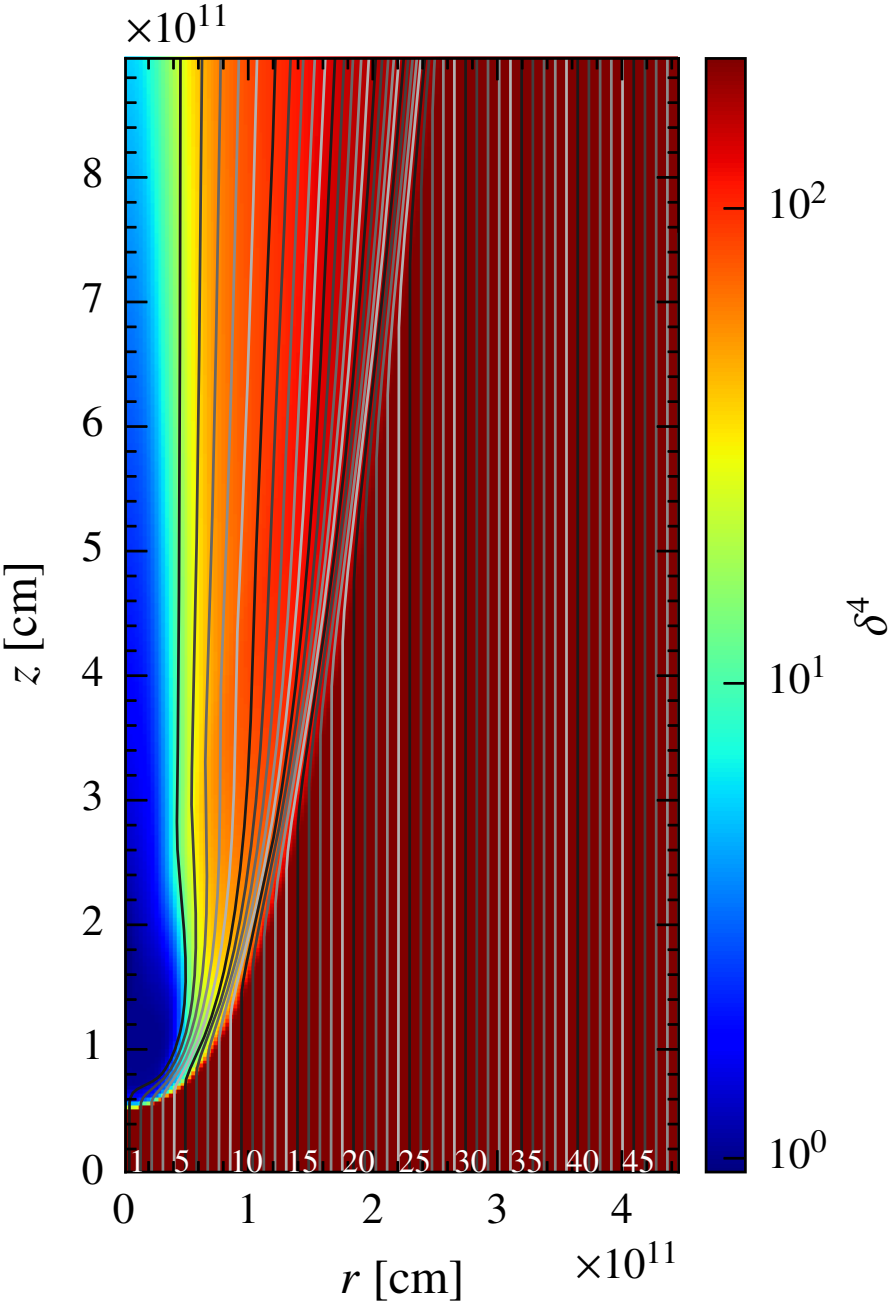

Figure 5.2: Doppler boosting factor for $\phi_{\rm obs} = 0°$. The grey lines represent the computed streamlines, which are numbered.

Stage	Low B ($\chi_B = 10^{-3}$)	High B ($\chi_B = 1$)
Compression phase	1.30×10^{35}	2.15×10^{34}
Disruption phase	1.12×10^{36}	4.71×10^{34}

Table 5.1: Values of the integrated emission in the 0.1–100 GeV band, given in erg s^{-1}, considering an observer angle of $\phi_{\rm obs} = 30°$. The compression and disruption states are computed based on the first and third snapshots in Fig. 5.1, respectively.

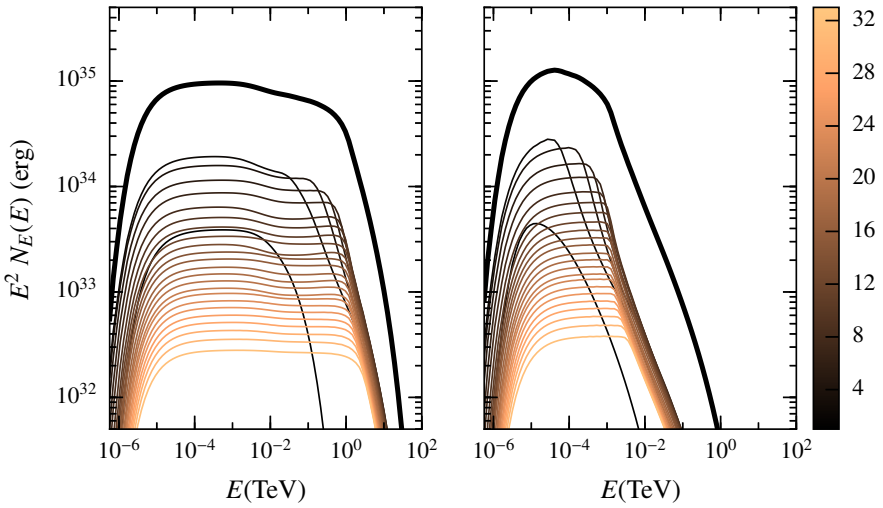

Figure 5.3: Compression-phase electron energy distribution for the individual streamlines (thin lines), and the total electron distribution (thick lines). The left panel corresponds to the low magnetic field case ($\chi_B = 10^{-3}$), and the right panel to the high magnetic field case ($\chi_B = 1$).

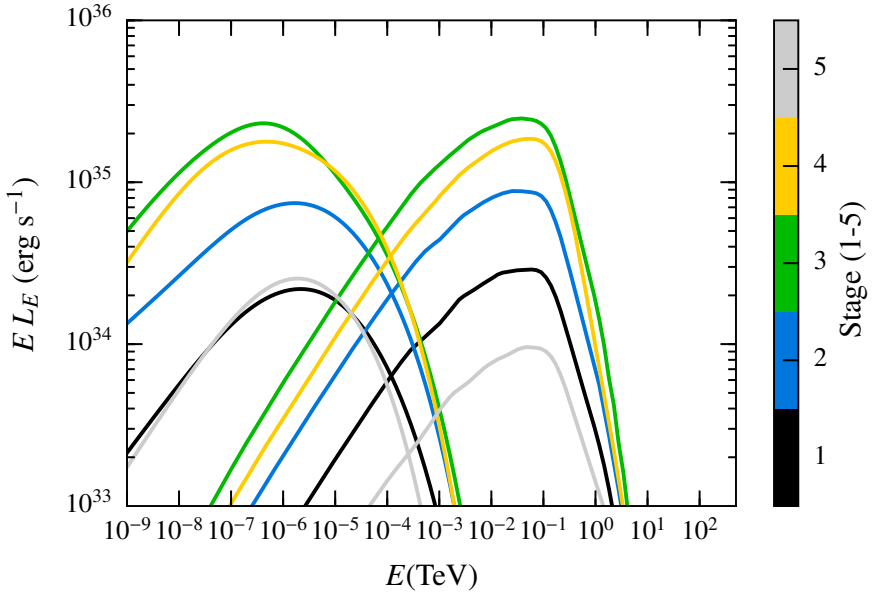

Figure 5.4: Spectral Energy Distributions for the 5 stages shown in Fig. 5.1. Stage 1 corresponds to the compression phase, whereas stage 3 is the disruption phase; $\chi_B = 10^{-3}$ is adopted, and $\phi_{\rm obs} = 30°$.

with few large ones and increasingly many more small ones, being the clump size and mass distributed as a power-law (Moffat and Corcoran, 2009). The X-ray spectrum of single and binary massive stars is compatible with this picture of dominant small-scale clumps and rarer large clumps Moffat, 2008.

For simplicity, we consider the clumps to be spherical, and neglect vorosity (i.e. porosity in velocity space, see e.g. Muijres et al., 2011), which in the present context can be considered as a minor effect. An empirical number density distribution of clumps with radius $R_{\rm c}$ is adopted:

$$n(R_{\rm c}) = \frac{{\rm d}N}{{\rm d}R_{\rm c}{\rm d}V} = n_0 {R_{\rm c}}^{-\alpha}, \tag{5.5}$$

with clump radii ranging $R_{\rm c,min} < R_{\rm c} < R_{\rm c,max}$. The value of $R_{\rm c,min}$ can be considered close to the Sobolev length, $R_{\rm Sob} \approx 0.01 R_*$ (e.g. Owocki and Cohen, 2006), while the clump size is at most of the order of R_* (Liermann et al., 2010), although it may be significantly smaller. As clumps propagate from the region where they form, at $\sim 1 - 2\,R_*$ from the star centre, they can grow linearly with the stellar distance or somewhat slower for a slab geometry, but they can be also broken down by instabilities (see the discussion at the end of sect. 3.3 in Bosch-Ramon, 2013).

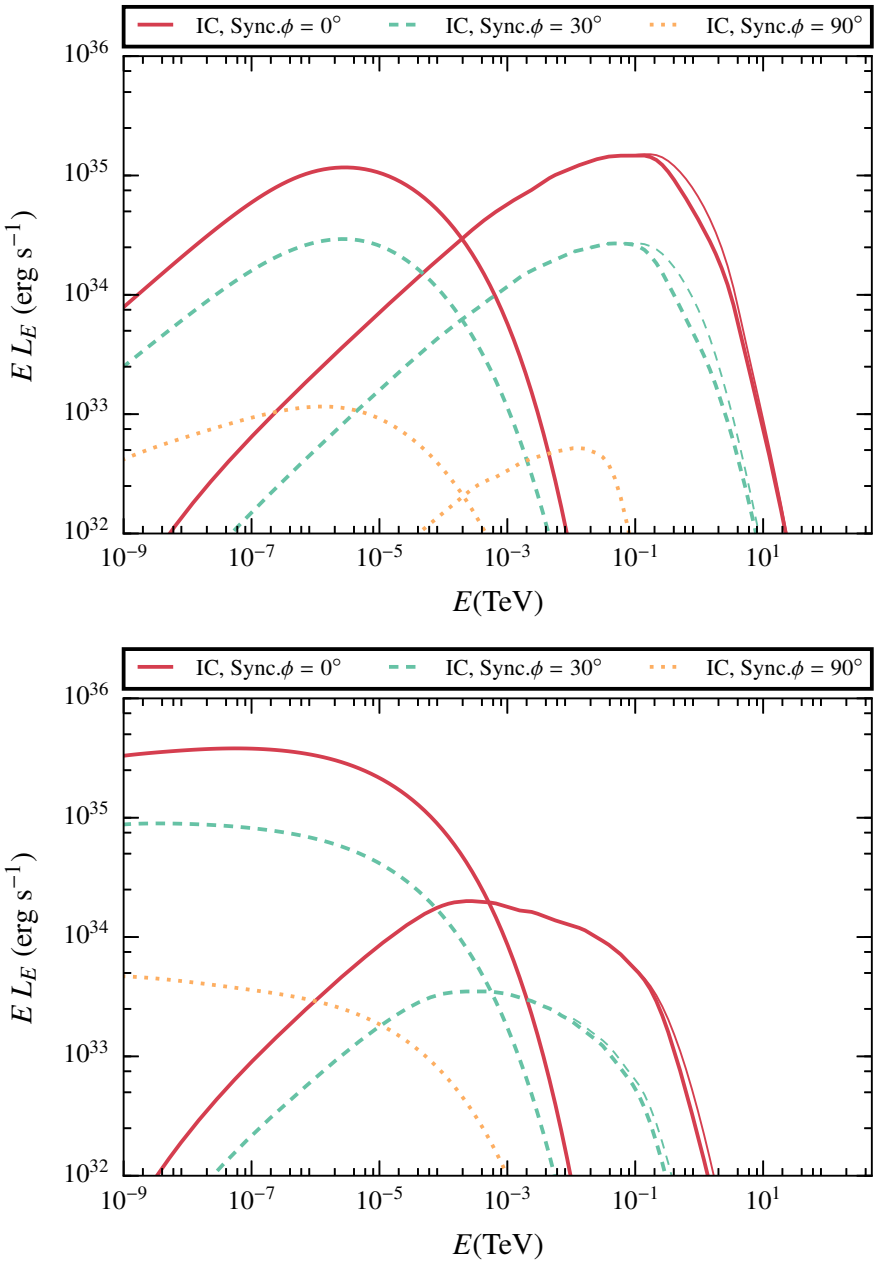

Figure 5.5: Top panel: Synchrotron and IC SEDs for the compression phase for $\phi_{\rm obs} = 0$, 30, and 90°, and $\chi_B = 10^{-3}$. The thin lines represent the emission without taking into account gamma-ray absorption due to electron-positron pair creation, i.e. the production SED. Bottom panel: the same as for the top panel but for $\chi_B = 1$.

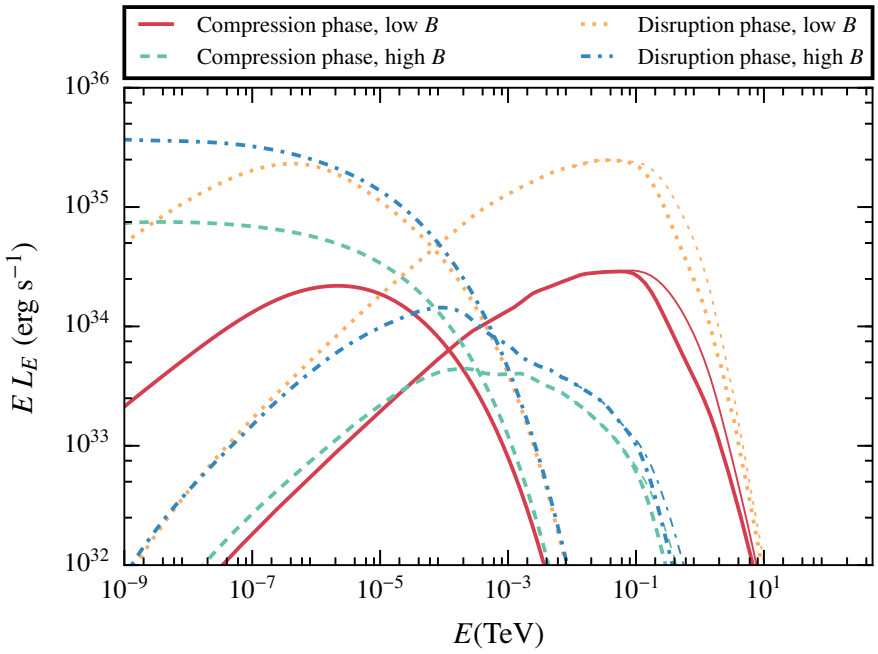

Figure 5.6: A comparison between the SEDs of the compression and disruption phases, for $\phi_{\rm obs} = 30°$.

Assuming that all clumps have the same density and that the inter-clump medium is void, the clump volume filling factor is simply $f = \chi^{-1}$ (e.g. Hamann et al., 2008), and the distribution function should meet the following normalization condition:

$$\frac{4\pi}{3}\int_{R_{\rm c,min}}^{R_{\rm c,max}} R_{\rm c}^3\, n(R_{\rm c})\,{\rm d}R_{\rm c} = f\,. \tag{5.6}$$

Fixing $R_{\rm c,min} = 0.01R_*$ and $R_{\rm c,max} = 0.5R_*$, we can solve Eq. (5.6) to obtain the normalization constant n_0.

Whether clump-jet interactions appear as a transient or as a persistent phenomenon is determined by the duty-cycle (DC) of these events. To determine DC we need to estimate the jet penetration rate of the clumps, $\dot{N}$, and their lifetime, $t_{\rm c}$ (Bosch-Ramon, 2013). The jet crossing time will be more relevant than $t_{\rm c}$ for jet powers $R_{\rm c}/R_{\rm j}$ times the limit provided in Eq. (5.4). In this chapter we are interested in bright sources, and therefore the jet power will be assumed to be close to the limit provided in Eq. (5.4). In fact, this is likely the case in the powerful jet sources Cyg X-3 and Cyg X-1.

The jet subtends a certain solid angle, Ω, as seen from the optical star. To interact with the jet, a clump must propagate within this solid angle. Considering a conical jet with $R_{\rm j} = \theta_{\rm j} z_{\rm j}$ and that the clump enters

the jet roughly between $0.5R_{\rm orb} \lesssim z \lesssim 1.5R_{\rm orb}$ (so $\Delta z \sim R_{\rm orb}$), we obtain $\Omega \approx \theta_j/2 = 0.05$. The differential rate of arrival to the jet for clumps of radius $R_{\rm c}$ can be estimated as $\mathrm{d}\dot{N} = \Omega d^2 v_{\rm w} n(R_{\rm c})\mathrm{d}R_{\rm c}$, where for simplicity $d \approx \sqrt{R_{\rm orb}^2 + z_{\rm j}^2}$. The differential DC for those clumps is $\mathrm{d}DC = t_{\rm c}\mathrm{d}\dot{N}$, with $t_{\rm c} \sim R_{\rm c}/v_{\rm sh}$, which we approximate here to $t_{\rm c} = R_{\rm c}/v_{\rm w}$ as we deal with powerful jets[2]. From all this, the following estimate for the arrival of clumps with radius between R_1 and R_2 can be obtained:

$$DC(R_1, R_2) = \Omega d^2 n_0 \int_{R_1}^{R_2} R_{\rm c}^{-\alpha+1}\mathrm{d}R_{\rm c} \approx \frac{\theta_{\rm j}}{2} d^2 n_0 \int_{R_1}^{R_2} R_{\rm c}^{-\alpha+1}\mathrm{d}R_{\rm c}. \quad (5.7)$$

We explore different values of the power-law index: $2.5 \leqslant \alpha \leqslant 6$. Values of $\alpha \geq 4$ imply that small clumps dominate the wind mass. Interestingly, as the energy emitted by one clump-jet interaction is expected to be $\propto t_{\rm c} \times R_{\rm c}^2 \propto R_{\rm c}^3$, one also obtains that for $\alpha > 3$ the non-thermal radiation will be dominated by the smallest clumps that can enter into the jet, i.e. those with $R_{\rm c} \sim R_0$. On the other hand, values of $\alpha \approx 2.5$ are in accordance to the values inferred for WR stars (Moffat, 2008)[3].

The non-thermal luminosity of the clump-jet collective interactions depends on the dominant clump size; gamma rays can be mostly produced by small or large clumps. The DC may be dominated by small clumps, and still the luminosity may be dominated by the largest ones. Nevertheless, the simulations show that clumps significantly larger than R_0 cannot increase considerably the luminosity output, and may even radiate less than smaller clumps interacting with the jet. The reason is that, unless $(\theta_{\rm j}/0.1)(10/\chi)$ is well below one (see Eq. 5.1), larger clumps will likely disrupt the whole jet, strongly reduce the effect of Doppler boosting, and might even switch off particle acceleration. For the parameters adopted in this work, it seems therefore natural to consider clumps of radii between $\sim R_0$ and few times larger.

The top panel of Fig. 5.7 shows the DC dependence on α, whereas the bottom panel shows the same but for the average luminosity of the collective clump-jet interactions. We have focused on $1\,R_0 < R_{\rm c} < 3\,R_0$, splitting this range into $1\,R_0 < R_{\rm c} < 2\,R_0$ and $2\,R_0 < R_{\rm c} < 3\,R_0$, although a curve for $R_{\rm c} > 3\,R_0$ is also shown. The radius $3\,R_0$ has been considered as the upper-limit for the clumps to be relevant from the radiation point of view in the

2 This assumption makes the estimate of the luminosity for collective interactions more conservative.

3 The value given is actually $N(m) \propto m^{\gamma}$, with $\gamma = 1.5 \pm 0.1$. Assuming constant density, spherical clumps, one derives $\alpha \approx 2.5$.

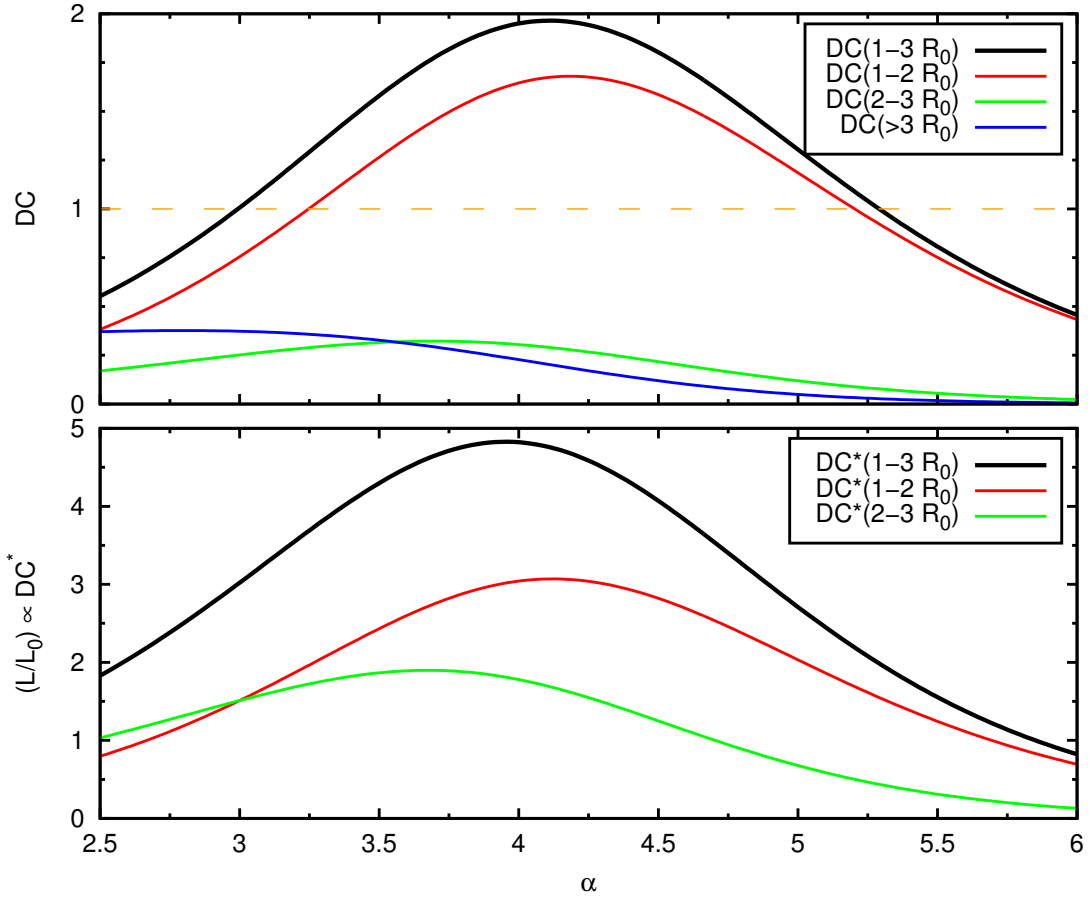

Figure 5.7: Top panel: Duty-cycle in the radius ranges $1-2\,R_0$, $2-3\,R_0$, $1-3\,R_0$, and $>3\,R_0$ for a wind clump number distribution $n \propto {R_c}^{-\alpha}$. A value $\alpha \approx 5$ represents a wind dominated by small clumps, whereas $\alpha_2 \approx 2.5$ is an observational value for WR stars; R_0 is the minimum clump size given by Eq. (5.1). Bottom panel: Duty-cycle weighted by the effective section of the shock, and therefore its potential luminosity, shown in units of the luminosity L_0 produced in the interaction of one clump of $R = R_0$ with the jet. The case $>3\,R_0$ is not shown as it may imply jet disruption.

context of this thesis, that is $(\theta_j/0.1)(10/\chi) \sim 1$. The results obtained allow the derivation of a rather robust conclusion: clumps with $R_c > R_0$ will be always present inside the jet unless the α parameter deviates strongly from the expected values. Also, the averaged total luminosity should be a factor of a few larger than the estimate obtained for a jet interacting with one clump of radius R_0 (again unless α is in the extremes of the explored range). We studied cases with different $R_{c,max}$-values (not shown here), and found that our conclusions hold for a wide range of $R_{c,max} \sim 0.1-1 R_*$.

For jet powers well below the value given in Eq. (5.4), the clump-jet interaction luminosity is $\propto L_j$ and therefore lower than the reference case, but the event duration is longer by $\propto v_{sh}^{-1} \propto L_j^{-1/2}$ (recall that v_{sh} must be used instead of v_w, see above). Thus, to first order, the decrease in the radiation luminosity will effectively be $\propto L_j^{1/2}$, although a more accurate relation should be derived numerically.

If clumps with $R_c > 3R_0$ are present and $DC \gtrsim 0.5$, the jet will be likely disrupted most of the time in the region of interest, $z_j \sim R_{orb}$. As noted, this is expected to significantly reduce the effects of Doppler boosting, and potentially might even switch off particle acceleration. In the scenario explored, i.e. $(\theta_j/0.1)(10/\chi) \sim 1$, a value $DC \sim 0.5$ for $R_c > 3R_0$ will be achieved only for $\alpha \lesssim 3$ and $R_{c,max} \sim 0.2 R_*$. This sets limits on the wind properties that allow clump-jet interactions to produce significant gamma-ray emission. These are however somewhat extreme, possibly unrealistic, wind parameters, in particular concerning the constraint on α, as in that case the wind mass would be dominated by the largest clumps.

Finally, let us explore situations different from $(\theta_j/0.1)(10/\chi) \sim 1$:

1. Fixing $(\theta_j/0.1) \sim 1$: Sources with $(10/\chi) > 1$ would imply that R_0 would be larger, and there may be no clumps big enough to cross the shocked wind surrounding the jet. In addition, a χ well below 10 would mean a rather homogeneous wind. On the other hand, for $(10/\chi) < 1$, R_0 would be smaller; all the clumps may be able to reach the jet, and they may be also dense enough to fully enter inside. This would have the disrupting effect of a wind with most of its mass in large, penetrating clumps (this kind of scenario is simulated in Perucho and Bosch-Ramon, 2012). Additionally, the number of clumps would be lower by $\chi^{-1} \propto f$ (see Eq. (5.6)), but because t_c is actually $\propto f^{-1/2} \propto \chi^{1/2}$, the radiation luminosity would be $\propto f^{1/2} \propto \chi^{-1/2}$ lower.

2. Fixing $(10/\chi) \sim 1$: Taking $(\theta_j/0.1) < 1$ would imply that smaller clumps could reach the jet but the latter would be denser, making

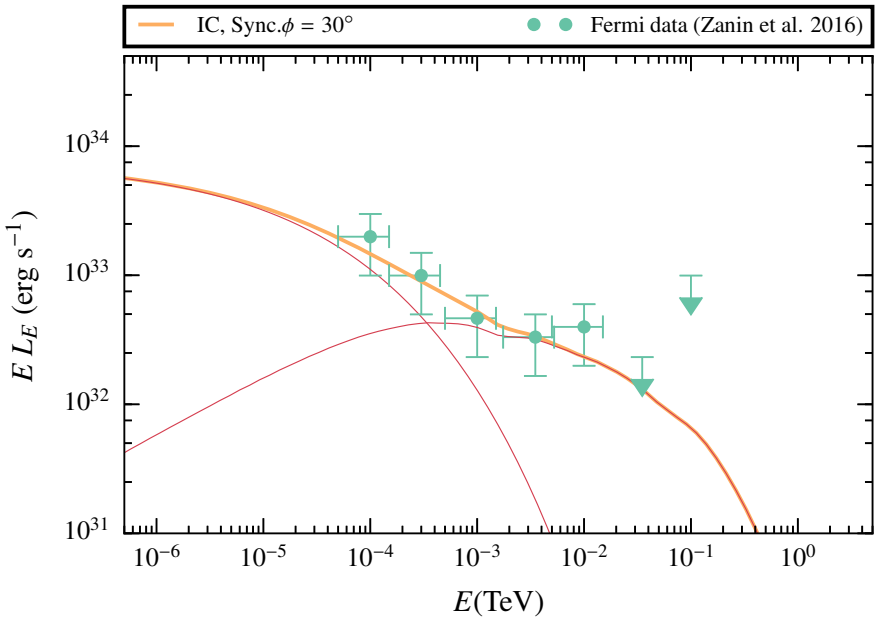

Figure 5.8: Synchrotron and IC SEDs (thin lines, red) computed for the compression phase and the sum of the two contributions (thick, orange line) plotted together with the Fermi data of Cyg X-1 published in Zanin et al., 2016. In this case, we have adopted a rather strong magnetic field ($\chi_B = 0.5$) and fixed the acceleration efficiency to $\eta_{NT} = 0.01$. The observing angle is $\phi_{obs} = 30°$.

clump penetration more difficult. Also, jet penetration would be less frequent ($DC \propto \Omega \propto \theta_j$). On the other hand, if $(\theta_j/0.1) > 1$, jet penetration would be significantly easier and more frequent, but clumps should be larger to first cross the shocked wind surrounding the jet.

5.5 DISCUSSION AND SUMMARY

For typical values of the clumping factor of massive star winds, and of the jet geometry and power, we obtain that clumps of intermediate size, say a few % of the stellar radius, can overcome the shocked wind surrounding the jet, and penetrate into the latter. For $\chi \sim 10$, clumps can already sustain the jet impact long enough for fully penetrate into the jet, allowing for a dynamically strong interaction. Under such circumstances, and assuming moderate acceleration efficiencies, say $\eta_{NT} \sim 0.01 - 0.1$, we predict significant gamma-ray luminosities for galactic sources at few kpc distances. For mildly relativistic jets, the impact of Doppler boosting is non-negligible even for relatively large jet viewing angles, $\sim 30°$. If Γ_j

were higher, clump-jet interactions would be detected for viewing angles within a relatively narrow cone around the jet orientation, whereas $\Gamma_j \to 1$ would mean lower luminosities, although potentially still detectable if non-thermal efficiencies were high.

In what follows we focus on the possibility of explaining the persistent GeV emission detected from Cyg X-1 and Cyg X-3 during the low-hard state and GeV activity periods, respectively. The calculations presented in Sect. 5.3 for one clump-jet interaction were carried out for a system with similar properties to those of Cyg X-1. For Cyg X-3, the results would be similar, but $R_{\rm orb}$ and thus R_0 would be ~ 10 times smaller, and the jet power and therefore the non-thermal emission ~ 10 times higher (see Yoon et al., 2016, and references therein for a comparison of these two sources). The IC luminosity in the high B case would be lower though with respect to the injected luminosity because of the higher jet power. From the one-clump interaction properties, one can extrapolate the characteristic gamma-ray luminosity in the context of collective clump-jet interactions.

The collective clump-jet interaction luminosity, in the GeV (0.1–100 GeV) range, calculated averaging over one orbit[4], and the computed clump evolution, for a jet inclination with the line of sight of $\phi_{\rm obs} = 30°$, is $\sim 10^{35}\,(\eta_{\rm NT}/0.1)$ erg s^{-1} for Cyg X-1 and ($\sim 10^{36}\,(\eta_{\rm NT}/0.1)$ erg s^{-1} for Cyg X-3), with an uncertainty of a factor ~ 0.5–2 (including the high and the low B cases in that range). Assuming that the jet in Cyg X-1 is perpendicular to the orbital plane, its inclination with respect to the line of sight is $\phi_{\rm obs} \sim 30°$ (Orosz et al., 2011). In Cyg X-3, the jet inclination may be similar or even smaller (see, e.g., Mioduszewski et al. 2001; Dubus et al. 2010a; see however Martí et al. 2001). Section 5.4 shows that $DC \sim 1$ are expected. Therefore, taking into account that the GeV luminosity in Cyg X-1 and Cyg X-3 are $\approx 5 \times 10^{33}$ (Zanin et al., 2016) and $\approx 3 \times 10^{36}$ erg s^{-1} (Fermi LAT Collaboration et al., 2009), respectively, one can derive the required non-thermal efficiency to be $(\eta_{\rm NT}/0.1) \sim 0.05$ for Cyg X-1, and ~ 3 for Cyg X-3 (for $\phi_{\rm obs} = 30°$; ~ 0.5 for $\phi_{\rm obs} \sim 0°$).

For Cyg X-1 the observational constraints only require a very modest non-thermal fraction ($\sim 1\%$). A comparison with Fermi data published in Zanin et al., 2016 is shown in Fig. 5.8, where a rather strong magnetic field ($\chi_{\rm B} = 0.5$) and a fixed acceleration efficiency ($\eta_{\rm NT} = 0.01$) were needed to reproduce the observational data, assuming $DC = 1$. We note that this is a simplified model, but it is interesting that even so it can

4 The GeV luminosity was also computed in inferior and superior conjunction so that the estimate was more representative.

approximately match the Fermi data. A similar toy-application of our model to Cyg X-3 could be also performed (not shown here), for similar parameters to those of Cyg X-1 but a much larger non-thermal fraction. In this case, the energetics is however rather demanding ($\sim 30\%$). Nevertheless, the presented calculations are obtained fixing $\Gamma_j = 2$, while in fact different Γ_j-values are possible, and despite the relation between Γ_j and the Lorentz factor of the shocked jet flow is non-trivial (it depends on the postshock flow re-acceleration), slightly faster jets could alleviate the tight energetics for the Cyg X-3-like scenario. In addition, adopting a low magnetic field and the (probable) possibility of DC of a few would relax further the energetic constraints. Finally, the numerical calculations carried out are also likely to underestimate the non-thermal emission because the computational grid encloses a relatively small region, and part of the radiation, and the last stages of the clump evolution, are not accounted for (see Sect. 5.3).

Values of $DC \ll 1$ would lead to flares rather than to a smoother clump-jet interaction continuum. This requires a much higher degree of inhomogeneity than the assumed in most of this work, as strong changes in $R_{c,min}$ and $R_{c,max}$ are not plausible, and DC is not very sensitive to α. However, as noted in Sect. 5.4, the radiation luminosity is $\propto \chi^{-1/2}$, meaning that for the same parameters, very inhomogeneous winds interacting with jets will be on average less radiatively efficient than moderately inhomogeneous ones.

Part IV

CONCLUDING REMARKS

6

CONCLUDING REMARKS

Throughout this thesis we have developed a tool to study the non-thermal radiation of different sources with relativistic emitters. Making use of the results of hydrodynamic simulations, we built a code to compute the evolution of NT particles and their IC and synchrotron radiation. Then we applied this tool to three different scenarios, of either extragalactic and galactic nature. These scenarios have several features in common:

1. The emitting flow moves at relativistic speeds, making the computation of the Doppler boosting of key importance.

2. They present an axis of symmetry and therefore can be studied at first order through 2D axisymmetric simulations.

3. The magnetic field is not expected, to first order, to be strong enough to be dynamically relevant, so the study can be performed without magneto-hydrodynamic simulations.

4. The most efficient non-thermal radiation processes are IC and synchrotron emission.

5. The environment of the source is rich, and we put the focus on its interaction with the relativistic fluid, where the NT particles are accelerated.

With this last point in mind, this thesis shows the importance of a complex environment in relativistic sources, where an inhomogeneity in the region of the fluid can act as a source of inertia in the system and produce shocks. We have shown the impact of this interactions in several contexts. Here we outline the most important remarks of each one.

STAR-JET INTERACTIONS IN AGN

In the case of the AGN jet interacting with a star, the work done appeared published in de la Cita et al., 2016, and we found that:

- The size of the emitter is enhanced; a large-scale bow-shock structure is produced increasing the NT luminosity.

- The Doppler boosting is of key importance given the relativistic nature of the (collimated) jet. This implies that the angle between the jet direction and the line of sight determines the observed luminosity.

- The luminosity levels found by our work point towards detectable gamma-ray emission in AGN, under the adopted assumptions and with a rich stellar population.

PULSAR WIND INTERACTING WITH A CLUMPLY STELLAR WIND

In this case, the work done has been published in de la Cita et al., 2017b, and has the following remarkable conclusions:

- We have shown that the clump makes the contact discontinuity move closer to the pulsar, with the whole emitting region experimenting a more powerful, less diluted pulsar wind, which modifies the escape and synchrotron energy losses of particles.

- In the majority of the configurations studied, the appearance of a clump boosts the luminosity significantly, pointing out the importance of these interactions.

- A specific study of the binary PSR B1259 – 63 was performed, both addressing the GeV Fermi flare, and the TeV observations. For the first case, our model was unable to reproduce the data, but in the second case we model the passage of the compact object through the decretion disc of the companion as an encounter with a big clump. This second model was more successful, showing how the impact of such an interaction can reproduce the SED in the TeV range.

CLUMPY WIND-JET INTERACTIONS IN HMMQS

The third main study of this thesis (de la Cita et al., 2017a) has been submitted to A&A and accepted for publication. Here we outline its most important conclusions:

- For the clump size, density contrast and height with respect to the base of the jet considered, being in fact rather characteristic parameters, the clump is able so *survive* enough time to emit gamma rays before disruption.

- The luminosity levels found could be enough to explain the observations of Cyg X-1 and Cyg X-3 adopting conservative parameters.

- A specific study for Cyg X-1 was carried out, finding a good match with the Fermi observations.

- We have shown that such a clump-jet interactions would have a duty cycle of $\sim$1, it is to say, at every time at least one clump with the studied characteristics would penetrate inside the jet.

FUTURE WORK

The obvious step forward in this research is twofold: on one hand, to extend the methods developed in the thesis to cover aspects as synchrotron self-Compton internal pair creation or hadronic mechanisms for non-thermal radiation, in order to cover a wider range of emitters. On the other hand, the application of this method to either 3D, or MHD simulations (or both) would allow us to have a more realistic picture of the emitters. This would lead to more accurate SEDs, to less a priori assumptions and, if the time-resolution of the simulations is good enough, also to light-curves in the cases where they would be relevant.

Such improvements in our methods would eventually lead to a change in our approach in the study. Instead of focusing on more general works like those presented in this thesis, where we were interested in showing the importance of different mechanisms of emission in certain contexts without focusing on a specific source, we could start trying to reproduce the observations of these sources. Spectral energy distributions, light-curves and/or maps of the emitting region should match the available observations in future studies.

LIST OF ACRONYMS

AGILE Astro-Rivelatore Gamma a Immagini LEggero.
AGN Active Galactic Nucleus.
BH black hole.
CGRO Compton Gamma-ray Observatory.
COMPTEL Imaging Compton Telescope.
CTA Cherenkov Telescope Array.
EGRET Energetic Gamma Ray Experiment Telescope.
Fermi Fermi Gamma-ray Space Telescope.
FF fluid frame.
GRB Gamma-ray Burst.
H.E.S.S. High Energy Stereoscopic System.
HAWC High-Altitude Water Cherenkov Observatory.
HE high energy.
HMMQ High-mass microquasar.
IATC Imaging Atmostpheric Cherenkov Telescope.
IC inverse Compton.
INFC inferior conjunction.
IR infrared.
KN Klein-Nishina.
LAT Large Area Telescope.
LF laboratory frame.
MAGIC Major Atmospheric Gamma Imaging Cherenkov Telescopes.
NS neutron star.

NT non-thermal.
RHD relativistic hydrodynamical.
SED spectral energy distribution.
SMBH supermassive black hole.
SUPC superior conjunction.
VERITAS Very Energetic Radiation Imaging Telescope Array System.
VHE very high energy.

BIBLIOGRAPHY

Aharonian, F. A. (2004). *Very high energy cosmic gamma radiation : a crucial window on the extreme Universe*.

Aharonian, F. A. and S. V. Bogovalov (2003). "Exploring physics of rotation powered pulsars with sub-10 GeV imaging atmospheric Cherenkov telescopes". In: *New A* 8, pp. 85–103. DOI: 10.1016/S1384-1076(02)00200-2. eprint: astro-ph/0208036.

Aharonian, F. A., S. V. Bogovalov, and D. Khangulyan (2012). "Abrupt acceleration of a 'cold' ultrarelativistic wind from the Crab pulsar". In: *Nature* 482, pp. 507–509. DOI: 10.1038/nature10793.

Aharonian, F. et al. (2005). "Discovery of the binary pulsar PSR B1259-63 in very-high-energy gamma rays around periastron with HESS". In: *A&A* 442, pp. 1–10. DOI: 10.1051/0004-6361:20052983. eprint: astro-ph/0506280.

Aharonian, F. et al. (2006a). "3.9 day orbital modulation in the TeV γ-ray flux and spectrum from the X-ray binary LS 5039". In: *A&A* 460, pp. 743–749. DOI: 10.1051/0004-6361:20065940. eprint: astro-ph/0607192.

Aharonian, F. et al. (2006b). "Microquasar LS 5039: a TeV gamma-ray emitter and a potential TeV neutrino source". In: *Journal of Physics Conference Series* 39, pp. 408–415. DOI: 10.1088/1742-6596/39/1/106. eprint: astro-ph/0508658.

Aharonian, F. et al. (2009). "Very high energy γ-ray observations of the binary PSR B1259-63/SS2883 around the 2007 Periastron". In: *A&A* 507, pp. 389–396. DOI: 10.1051/0004-6361/200912339.

Albert, J. et al. (2007). "Very High Energy Gamma-Ray Radiation from the Stellar Mass Black Hole Binary Cygnus X-1". In: *ApJ* 665, pp. L51–L54. DOI: 10.1086/521145. arXiv: 0706.1505.

Alfvén, H. (1942). "Existence of Electromagnetic-Hydrodynamic Waves". In: *Nature* 150, pp. 405–406. DOI: 10.1038/150405d0.

Araudo, A. T. et al. (2007). "Gamma-ray emission from massive young stellar objects". In: *A&A* 476, pp. 1289–1295. DOI: 10.1051/0004-6361:20077636. arXiv: 0708.2955.

Araudo, A. T., V. Bosch-Ramon, and G. E. Romero (2009). "High-energy emission from jet-clump interactions in microquasars". In: *A&A* 503, pp. 673–681. DOI: 10.1051/0004-6361/200811519. arXiv: 0906.4803 [astro-ph.HE].

Araudo, A. T., V. Bosch-Ramon, and G. E. Romero (2013). "Gamma-ray emission from massive stars interacting with active galactic nuclei jets". In: *MNRAS* 436, pp. 3626–3639. DOI: 10.1093/mnras/stt1840. arXiv: 1309.7114 [astro-ph.HE].

Barkov, M. V., F. A. Aharonian, and V. Bosch-Ramon (2010). "Gamma-ray Flares from Red Giant/Jet Interactions in Active Galactic Nuclei". In: *ApJ* 724, pp. 1517–1523. DOI: 10.1088/0004-637X/724/2/1517. arXiv: 1005.5252 [astro-ph.HE].

Barkov, M. V., V. Bosch-Ramon, and F. A. Aharonian (2012a). "Interpretation of the Flares of M87 at TeV Energies in the Cloud-Jet Interaction Scenario". In: *ApJ* 755, 170, p. 170. DOI: 10.1088/0004-637X/755/2/170. arXiv: 1202.5907 [astro-ph.HE].

Barkov, M. V. et al. (2012b). "Rapid TeV Variability in Blazars as a Result of Jet-Star Interaction". In: *ApJ* 749, 119, p. 119. DOI: 10.1088/0004-637X/749/2/119. arXiv: 1012.1787 [astro-ph.HE].

Bednarek, W. (2013). "High energy γ-ray emission from compact galactic sources in the context of observations with the next generation Cherenkov Telescope Arrays". In: *Astroparticle Physics* 43, pp. 81–102. DOI: 10.1016/j.astropartphys.2012.05.001. arXiv: 1205.1116 [astro-ph.HE].

Bednarek, W. and P. Banasiński (2015). "Non-thermal Radiation from Collisions of Compact Objects with Intermediate-scale Jets in Active Galaxies". In: *ApJ* 807, 168, p. 168. DOI: 10.1088/0004-637X/807/2/168. arXiv: 1506.01181 [astro-ph.HE].

Bednarek, W. and R. J. Protheroe (1997). "Gamma-rays from interactions of stars with active galactic nucleus jets". In: *MNRAS* 287, pp. L9–L13. eprint: astro-ph/9612073.

Bodaghee, A. et al. (2013). "Gamma-Ray Observations of the Microquasars Cygnus X-1, Cygnus X-3, GRS 1915+105, and GX 339-4 with the Fermi Large Area Telescope". In: *ApJ* 775, 98, p. 98. DOI: 10.1088/0004-637X/775/2/98. arXiv: 1307.3264 [astro-ph.HE].

Bogovalov, S. V. and F. A. Aharonian (2000). "Very-high-energy gamma radiation associated with the unshocked wind of the Crab pulsar". In: *MNRAS* 313, pp. 504–514. DOI: 10.1046/j.1365-8711.2000.03250.x. eprint: astro-ph/0003157.

Bogovalov, S. V. et al. (2008). "Modelling interaction of relativistic and non-relativistic winds in binary system PSR B1259-63/SS2883 - I. Hydrodynamical limit". In: *MNRAS* 387, pp. 63–72. DOI: 10.1111/j.1365-2966.2008.13226.x. arXiv: 0710.1961.

Bogovalov, S. V. et al. (2012). "Modelling the interaction between relativistic and non-relativistic winds in the binary system PSR B1259-63/SS2883- II. Impact of the magnetization and anisotropy of the pulsar wind". In: *MNRAS* 419, pp. 3426–3432. DOI: 10.1111/j.1365-2966.2011.19983.x. arXiv: 1107.4831 [astro-ph.HE].

Bordas, P. et al. (2015). "Detection of Persistent Gamma-Ray Emission Toward SS433/W50". In: *ApJ* 807, L8, p. L8. DOI: 10.1088/2041-8205/807/1/L8. arXiv: 1411.7413 [astro-ph.HE].

Bosch-Ramon, V. (2011). "Radio emission from high-mass binaries with non-accreting pulsars". In: *ArXiv e-prints*. arXiv: 1103.2996 [astro-ph.HE].

Bosch-Ramon, V. (2012). "Fermi I particle acceleration in converging flows mediated by magnetic reconnection". In: *A&A* 542, A125, A125. DOI: 10.1051/0004-6361/201219231. arXiv: 1205.3450 [astro-ph.HE].

Bosch-Ramon, V. (2013). "Clumpy stellar winds and high-energy emission in high-mass binaries hosting a young pulsar". In: *A&A* 560, A32, A32. DOI: 10.1051/0004-6361/201322249. arXiv: 1310.5641 [astro-ph.HE].

Bosch-Ramon, V. (2015). "Non-thermal emission from standing relativistic shocks: an application to red giant winds interacting with AGN jets". In: *A&A* 575, A109, A109. DOI: 10.1051/0004-6361/201425208. arXiv: 1501.03118 [astro-ph.HE].

Bosch-Ramon, V. and M. V. Barkov (2016). "The effects of the stellar wind and orbital motion on the jets of high-mass microquasars". In: *A&A* 590, A119, A119. DOI: 10.1051/0004-6361/201628564. arXiv: 1604.06360 [astro-ph.HE].

Bosch-Ramon, V. and D. Khangulyan (2009). "Understanding the Very-High Emission from Microquasars". In: *International Journal of Modern*

Physics D 18, pp. 347–387. DOI: 10.1142/S0218271809014601. arXiv: 0805.4123.

Bosch-Ramon, V. and D. Khangulyan (2011). "Monte Carlo Simulations of Radio Emitting Secondaries in γ-Ray Binaries". In: *PASJ* 63, pp. 1023–1033. DOI: 10.1093/pasj/63.5.1023. arXiv: 1105.2172 [astro-ph.HE].

Bosch-Ramon, V., G. E. Romero, and J. M. Paredes (2006). "A broadband leptonic model for gamma-ray emitting microquasars". In: *A&A* 447, pp. 263–276. DOI: 10.1051/0004-6361:20053633. eprint: astro-ph/0509086.

Bosch-Ramon, V., D. Khangulyan, and F. A. Aharonian (2008). "Non-thermal emission from secondary pairs in close TeV binary systems". In: *A&A* 482, pp. 397–402. DOI: 10.1051/0004-6361:20079252. arXiv: 0801.4547.

Bosch-Ramon, V., M. Perucho, and M. V. Barkov (2012a). "Clouds and red giants interacting with the base of AGN jets." In: *A&A* 539, A69, A69. DOI: 10.1051/0004-6361/201118622. arXiv: 1201.5279 [astro-ph.HE].

Bosch-Ramon, V. et al. (2012b). "Simulations of stellar/pulsar-wind interaction along one full orbit". In: *A&A* 544, A59, A59. DOI: 10.1051/0004-6361/201219251. arXiv: 1203.5528 [astro-ph.HE].

Bosch-Ramon, V., M. V. Barkov, and M. Perucho (2015). "Orbital evolution of colliding star and pulsar winds in 2D and 3D: effects of dimensionality, EoS, resolution, and grid size". In: *A&A* 577, A89, A89. DOI: 10.1051/0004-6361/201425228. arXiv: 1411.7892 [astro-ph.HE].

Böttcher, M. and C. D. Dermer (2005). "Photon-Photon Absorption of Very High Energy Gamma Rays from Microquasars: Application to LS 5039". In: *ApJ* 634, pp. L81–L84. DOI: 10.1086/498615. eprint: astro-ph/0508359.

Bowman, M., J. P. Leahy, and S. S. Komissarov (1996). "The deceleration of relativistic jets by entrainment". In: *MNRAS* 279, p. 899.

Bucciantini, N., E. Amato, and L. Del Zanna (2005). "Relativistic MHD simulations of pulsar bow-shock nebulae". In: *A&A* 434, pp. 189–199. DOI: 10.1051/0004-6361:20042205. eprint: astro-ph/0412534.

Caliandro, G. A. et al. (2015). "Gamma-Ray Flare Activity from PSR B1259-63 during 2014 Periastron Passage and Comparison to Its 2010 Passage". In: *ApJ* 811, 68, p. 68. DOI: 10.1088/0004-637X/811/1/68. arXiv: 1509.02856 [astro-ph.HE].

Cerutti, B. et al. (2010). "Modeling the three-dimensional pair cascade in binaries. Application to LS 5039". In: *A&A* 519, A81, A81. DOI: 10.1051/0004-6361/201014459. arXiv: 1006.2683 [astro-ph.HE].

Chandrasekhar, S. (1961). *Hydrodynamic and hydromagnetic stability*.

Chernyakova, M. et al. (2006). "XMM-Newton observations of PSR B1259-63 near the 2004 periastron passage". In: *MNRAS* 367, pp. 1201–1208. DOI: 10.1111/j.1365-2966.2005.10039.x. eprint: astro-ph/0601241.

Chernyakova, M. et al. (2014). "Multiwavelength observations of the binary system PSR B1259-63/LS 2883 around the 2010-2011 periastron passage". In: *MNRAS* 439, pp. 432–445. DOI: 10.1093/mnras/stu021. arXiv: 1401.1386 [astro-ph.HE].

Chernyakova, M. et al. (2015). "Multi-wavelength observations of the binary system PSR B1259-63/LS 2883 around the 2014 periastron passage". In: *MNRAS* 454, pp. 1358–1370. DOI: 10.1093/mnras/stv1988. arXiv: 1508.01339 [astro-ph.HE].

Colella, P. and P. R. Woodward (1984). "The Piecewise Parabolic Method (PPM) for Gas-Dynamical Simulations". In: *Journal of Computational Physics* 54, pp. 174–201. DOI: 10.1016/0021-9991(84)90143-8.

Drury, L. O. (1983). "An introduction to the theory of diffusive shock acceleration of energetic particles in tenuous plasmas". In: *Reports on Progress in Physics* 46, pp. 973–1027. DOI: 10.1088/0034-4885/46/8/002.

Dubus, G. (2006a). "Gamma-ray absorption in massive X-ray binaries". In: *A&A* 451, pp. 9–18. DOI: 10.1051/0004-6361:20054233. eprint: astro-ph/0509633.

Dubus, G. (2006b). "Gamma-ray binaries: pulsars in disguise?" In: *A&A* 456, pp. 801–817. DOI: 10.1051/0004-6361:20054779. eprint: astro-ph/0605287.

Dubus, G. (2013). "Gamma-ray binaries and related systems". In: *A&A Rev.* 21, 64, p. 64. DOI: 10.1007/s00159-013-0064-5. arXiv: 1307.7083 [astro-ph.HE].

Dubus, G. and B. Cerutti (2013). "What caused the GeV flare of PSR B1259-63?" In: *A&A* 557, A127, A127. DOI: 10.1051/0004-6361/201321741. arXiv: 1308.4531 [astro-ph.HE].

Dubus, G., B. Cerutti, and G. Henri (2008). "The modulation of the gamma-ray emission from the binary LS 5039". In: *A&A* 477, pp. 691–700. DOI: 10.1051/0004-6361:20078261. arXiv: 0710.0968.

Dubus, G., B. Cerutti, and G. Henri (2010a). "Relativistic Doppler-boosted emission in gamma-ray binaries". In: *A&A* 516, A18, A18. DOI: 10.1051/0004-6361/201014023. arXiv: 1004.0511 [astro-ph.HE].

Dubus, G., B. Cerutti, and G. Henri (2010b). "The relativistic jet of Cygnus X-3 in gamma-rays". In: *MNRAS* 404, pp. L55–L59. DOI: 10.1111/j.1745-3933.2010.00834.x. arXiv: 1002.3888 [astro-ph.HE].

Dubus, G., A. Lamberts, and S. Fromang (2015). "Modelling the high-energy emission from gamma-ray binaries using numerical relativistic hydrodynamics". In: *A&A* 581, A27, A27. DOI: 10.1051/0004-6361/201425394. arXiv: 1505.01026 [astro-ph.HE].

Eichler, D. and V. Usov (1993). "Particle acceleration and nonthermal radio emission in binaries of early-type stars". In: *ApJ* 402, pp. 271–279. DOI: 10.1086/172130.

Fermi LAT Collaboration et al. (2009). "Modulated High-Energy Gamma-Ray Emission from the Microquasar Cygnus X-3". In: *Science* 326, pp. 1512–. DOI: 10.1126/science.1182174.

Ginzburg, V. L. and S. I. Syrovatskii (1964). "The Secondary Electron Component of Cosmic Rays and the Spectrum of General Galactic Radio Emission". In: *Soviet Ast.* 8, p. 342.

Gould, R. J. and G. P. Schréder (1967). "Pair Production in Photon-Photon Collisions". In: *Physical Review* 155, pp. 1404–1407. DOI: 10.1103/PhysRev.155.1404.

Grove, J. E. et al. (1995). "Evidence for Shock Acceleration in the Binary Pulsar System PSR B1259-63". In: *ApJ* 447, p. L113. DOI: 10.1086/309568.

Gruber, D. et al. (2014). "The Fermi GBM Gamma-Ray Burst Spectral Catalog: Four Years of Data". In: *ApJS* 211, 12, p. 12. DOI: 10.1088/0067-0049/211/1/12. arXiv: 1401.5069 [astro-ph.HE].

H.E.S.S. Collaboration et al. (2013). "H.E.S.S. observations of the binary system PSR B1259-63/LS 2883 around the 2010/2011 periastron passage". In: *A&A* 551, A94, A94. DOI: 10.1051/0004-6361/201220612. arXiv: 1301.3930 [astro-ph.HE].

Hamann, W.-R., L. M. Oskinova, and A. Feldmeier (2008). "Spectrum formation in clumpy stellar winds". In: *Clumping in Hot-Star Winds*. Ed. by W.-R. Hamann, A. Feldmeier, and L. M. Oskinova, p. 75.

Hardcastle, M. J. et al. (2003). "Radio and X-Ray Observations of the Jet in Centaurus A". In: *ApJ* 593, pp. 169–183. DOI: 10.1086/376519. eprint: astro-ph/0304443.

Hartman, R. C. et al. (1999). "The Third EGRET Catalog of High-Energy Gamma-Ray Sources". In: *ApJS* 123, pp. 79–202. DOI: 10.1086/313231.

Hayakawa, S. (1952). "Propagation of the Cosmic Radiation through Intersteller Space". In: *Progress of Theoretical Physics* 8, pp. 571–572. DOI: 10.1143/PTP.8.571.

Hubbard, A. and E. G. Blackman (2006). "Active galactic nuclei jet mass loading and truncation by stellar winds". In: *MNRAS* 371, pp. 1717–1721. DOI: 10.1111/j.1365-2966.2006.10808.x. eprint: astro-ph/0604585.

Johnston, S. et al. (1992). "PSR 1259-63 - A binary radio pulsar with a Be star companion". In: *ApJ* 387, pp. L37–L41. DOI: 10.1086/186300.

Johnston, S. et al. (2005). "Radio observations of PSR B1259-63 through the 2004 periastron passage". In: *MNRAS* 358, pp. 1069–1075. DOI: 10.1111/j.1365-2966.2005.08854.x. eprint: astro-ph/0501660.

Jones, T. W., D. Ryu, and I. L. Tregillis (1996). "The Magnetohydrodynamics of Supersonic Gas Clouds: MHD Cosmic Bullets and Wind-swept Clumps". In: *ApJ* 473, p. 365. DOI: 10.1086/178151. eprint: astro-ph/9606106.

Kennel, C. F. and F. V. Coroniti (1984). "Magnetohydrodynamic model of Crab nebula radiation". In: *ApJ* 283, pp. 710–730. DOI: 10.1086/162357.

Khangulyan, D. V. et al. (2013). "Star-Jet Interactions and Gamma-Ray Outbursts from 3C454.3". In: *ApJ* 774, 113, p. 113. DOI: 10.1088/0004-637X/774/2/113. arXiv: 1305.5117 [astro-ph.HE].

Khangulyan, D. and F. Aharonian (2005). "On the formation of energy spectra of synchrotron X-rays and inverse Compton γ-rays in binary systems with luminous optical stars". In: *High Energy Gamma-Ray Astronomy*. Ed. by F. A. Aharonian, H. J. Völk, and D. Horns. Vol. 745. American Institute of Physics Conference Series, pp. 359–364. DOI: 10.1063/1.1878430. eprint: astro-ph/0503499.

Khangulyan, D. et al. (2007). "TeV light curve of PSR B1259-63/SS2883". In: *MNRAS* 380, pp. 320–330. DOI: 10.1111/j.1365-2966.2007.12075.x. eprint: astro-ph/0605663.

Khangulyan, D., F. Aharonian, and V. Bosch-Ramon (2008). "On the formation of TeV radiation in LS 5039". In: *MNRAS* 383, pp. 467–478. DOI: 10.1111/j.1365-2966.2007.12572.x. arXiv: 0707.1689.

Khangulyan, D. et al. (2011). "Gamma-Ray Signal from the Pulsar Wind in the Binary Pulsar System PSR B1259-63/LS 2883". In: *ApJ* 742, 98, p. 98. DOI: 10.1088/0004-637X/742/2/98. arXiv: 1104.0211 [astro-ph.HE].

Khangulyan, D. et al. (2012). "Post-periastron Gamma-Ray Flare from PSR B1259-63/LS 2883 as a Result of Comptonization of the Cold

Pulsar Wind". In: *ApJ* 752, L17, p. L17. DOI: 10.1088/2041-8205/752/1/L17. arXiv: 1107.4833 [astro-ph.HE].

Khangulyan, D., S. V. Bogovalov, and F. A. Aharonian (2014a). "Binary Pulsar System PSR B1259-63/LS2883 as a Gamma-Ray Emitter". In: *International Journal of Modern Physics Conference Series* 28, 1460169, p. 1460169. DOI: 10.1142/S2010194514601690.

Khangulyan, D., F. A. Aharonian, and S. R. Kelner (2014b). "Simple Analytical Approximations for Treatment of Inverse Compton Scattering of Relativistic Electrons in the Blackbody Radiation Field". In: *ApJ* 783, 100, p. 100. DOI: 10.1088/0004-637X/783/2/100. arXiv: 1310.7971 [astro-ph.HE].

Kijak, J. et al. (2011). "Spectrum evolution in binary pulsar B1259-63/LS 2883 Be star and gigahertz-peaked spectra". In: *MNRAS* 418, pp. L114–L118. DOI: 10.1111/j.1745-3933.2011.01155.x. arXiv: 1109.1013 [astro-ph.GA].

Kishishita, T. et al. (2009). "Long-Term Stability of Nonthermal X-Ray Modulation in the Gamma-Ray Binary LS 5039". In: *ApJ* 697, pp. L1–L5. DOI: 10.1088/0004-637X/697/1/L1. arXiv: 0904.1064 [astro-ph.HE].

Klebesadel, R. W., I. B. Strong, and R. A. Olson (1973). "Observations of Gamma-Ray Bursts of Cosmic Origin". In: *ApJ* 182, p. L85. DOI: 10.1086/181225.

Komissarov, S. S. (1994). "Mass-Loaded Relativistic Jets". In: *MNRAS* 269, p. 394. DOI: 10.1093/mnras/269.2.394.

Kong, S. W., K. S. Cheng, and Y. F. Huang (2012). "Modeling the Multiwavelength Light Curves of PSR B1259-63/LS 2883. II. The Effects of Anisotropic Pulsar Wind and Doppler Boosting". In: *ApJ* 753, 127, p. 127. DOI: 10.1088/0004-637X/753/2/127. arXiv: 1205.2147 [astro-ph.HE].

Kraushaar, W. et al. (1965). "Explorer XI Experiment on Cosmic Gamma Rays." In: *ApJ* 141, p. 845. DOI: 10.1086/148179.

Lamberts, A. et al. (2013). "Simulating gamma-ray binaries with a relativistic extension of RAMSES". In: *A&A* 560, A79, A79. DOI: 10.1051/0004-6361/201322266. arXiv: 1309.7629 [astro-ph.IM].

Liermann, A. et al. (2010). "Structured stellar winds". In: *Revista Mexicana de Astronomia y Astrofisica Conference Series*. Vol. 38. Revista Mexicana de Astronomia y Astrofisica, vol. 27, pp. 50–51.

Lucy, L. B. and P. M. Solomon (1970). "Mass Loss by Hot Stars". In: *ApJ* 159, p. 879. DOI: 10.1086/150365.

Lyubarsky, Y. and J. G. Kirk (2001). "Reconnection in a Striped Pulsar Wind". In: *ApJ* 547, pp. 437–448. DOI: 10.1086/318354. eprint: astro-ph/0009270.

Malyshev, D., A. A. Zdziarski, and M. Chernyakova (2013). "High-energy gamma-ray emission from Cyg X-1 measured by Fermi and its theoretical implications". In: *MNRAS* 434, pp. 2380–2389. DOI: 10.1093/mnras/stt1184. arXiv: 1305.5920 [astro-ph.HE].

Maraschi, L. and A. Treves (1981). "A model for LSI61 deg 303". In: *MNRAS* 194, 1P–5P. DOI: 10.1093/mnras/194.1.1P.

Martí, J. M. . and E. Müller (1996). "Extension of the Piecewise Parabolic Method to One-Dimensional Relativistic Hydrodynamics". In: *Journal of Computational Physics* 123, pp. 1–14. DOI: 10.1006/jcph.1996.0001.

Martí, J. M. et al. (1997). "Morphology and Dynamics of Relativistic Jets". In: *ApJ* 479, pp. 151–163.

Martí, J., J. M. Paredes, and M. Peracaula (2001). "Development of a two-sided relativistic jet in Cygnus X-3". In: *A&A* 375, pp. 476–484. DOI: 10.1051/0004-6361:20010907.

Mignone, A., T. Plewa, and G. Bodo (2005). "The Piecewise Parabolic Method for Multidimensional Relativistic Fluid Dynamics". In: *ApJS* 160, pp. 199–219. DOI: 10.1086/430905. eprint: astro-ph/0505200.

Mioduszewski, A. J. et al. (2001). "A One-sided Highly Relativistic Jet from Cygnus X-3". In: *ApJ* 553, pp. 766–775. DOI: 10.1086/320965. eprint: astro-ph/0102018.

Mirabel, I. F. (2006). "Very energetic gamma-rays from microquasars and binary pulsars". In: *Science* 312, p. 1759. DOI: 10.1126/science.1129815. eprint: astro-ph/0606393.

Miškovičová, I. et al. (2016). "Chandra X-ray spectroscopy of focused wind in the Cygnus X-1 system. II. The non-dip spectrum in the low/hard state - modulations with orbital phase". In: *A&A* 590, A114, A114. DOI: 10.1051/0004-6361/201322490. arXiv: 1604.00364 [astro-ph.HE].

Moffat, A. F. J. (2008). "Observational overview of clumping in hot stellar winds". In: *Clumping in Hot-Star Winds*. Ed. by W.-R. Hamann, A. Feldmeier, and L. M. Oskinova, p. 17.

Moffat, A. F. J. and M. F. Corcoran (2009). "Understanding the X-ray Flaring from η Carinae". In: *ApJ* 707, pp. 693–704. DOI: 10.1088/0004-637X/707/1/693. arXiv: 0910.2395 [astro-ph.HE].

Morlino, G., M. Lyutikov, and M. Vorster (2015). "Mass loading of bow shock pulsar wind nebulae". In: *MNRAS* 454, pp. 3886–3901. DOI: 10.1093/mnras/stv2189. arXiv: 1505.01712 [astro-ph.HE].

Muijres, L. E. et al. (2011). "Predictions of the effect of clumping on the wind properties of O-type stars". In: *A&A* 526, A32, A32. DOI: 10.1051/0004-6361/201014290.

Müller, C. et al. (2014). "TANAMI monitoring of Centaurus A: The complex dynamics in the inner parsec of an extragalactic jet". In: *A&A* 569, A115, A115. DOI: 10.1051/0004-6361/201423948. arXiv: 1407.0162 [astro-ph.HE].

Negueruela, I. et al. (2011). "Astrophysical Parameters of LS 2883 and Implications for the PSR B1259-63 Gamma-ray Binary". In: *ApJ* 732, L11, p. L11. DOI: 10.1088/2041-8205/732/1/L11. arXiv: 1103.4636 [astro-ph.HE].

Odell, S. L. (1981). "Radiation force on a relativistic plasma and the Eddington limit". In: *ApJ* 243, pp. L147–L149. DOI: 10.1086/183462.

Okazaki, A. T. et al. (2011). "Hydrodynamic Interaction between the Be Star and the Pulsar in the TeV Binary PSR B1259-63/LS 2883". In: *PASJ* 63, pp. 893–901. DOI: 10.1093/pasj/63.4.893. arXiv: 1105.1481 [astro-ph.HE].

Olmi, B. et al. (2014). "On the magnetohydrodynamic modelling of the Crab nebula radio emission". In: *MNRAS* 438, pp. 1518–1525. DOI: 10.1093/mnras/stt2308. arXiv: 1310.8496 [astro-ph.HE].

Orosz, J. A. et al. (2011). "The Mass of the Black Hole in Cygnus X-1". In: *ApJ* 742, 84, p. 84. DOI: 10.1088/0004-637X/742/2/84. arXiv: 1106.3689 [astro-ph.HE].

Owocki, S. P. and D. H. Cohen (2006). "The Effect of Porosity on X-Ray Emission-Line Profiles from Hot-Star Winds". In: *ApJ* 648, pp. 565–571. DOI: 10.1086/505698. eprint: astro-ph/0602054.

Owocki, S. P. et al. (2009). "Gamma-Ray Variability from Wind Clumping in High-Mass X-Ray Binaries with Jets". In: *ApJ* 696, pp. 690–693. DOI: 10.1088/0004-637X/696/1/690. arXiv: 0902.2278 [astro-ph.HE].

Pacholczyk, A. G. (1970). *Radio astrophysics. Nonthermal processes in galactic and extragalactic sources*.

Padmanabhan, T. (2001). *Theoretical Astrophysics - Volume 2, Stars and Stellar Systems*.

Paredes-Fortuny, X. (2016). "Observational and theoretical study of the interaction of relativistic winds from young pulsars with inhomogeneous stellar winds". Ph.D. Thesis. Universitat de Barcelona.

Paredes-Fortuny, X. et al. (2015). "Simulations of an inhomogeneous stellar wind interacting with a pulsar wind in a binary system". In: *A&A* 574, A77, A77. DOI: 10.1051/0004-6361/201424672. arXiv: 1411.3593 [astro-ph.HE].

Perucho, M. (2014). "Jet Propagation and Deceleration". In: *International Journal of Modern Physics Conference Series* 28, 1460165, p. 60165. DOI: 10.1142/S2010194514601653. arXiv: 1310.7746 [astro-ph.HE].

Perucho, M. (2015). "Radio source evolution". In: *ArXiv:1507.03355 e-prints*. arXiv:1507.03355: 1507.03355.

Perucho, M. and V. Bosch-Ramon (2008). "On the interaction of microquasar jets with stellar winds". In: *A&A* 482, pp. 917–927. DOI: 10.1051/0004-6361:20078929. arXiv: 0802.1134.

Perucho, M. and V. Bosch-Ramon (2012). "3D simulations of microquasar jets in clumpy stellar winds". In: *A&A* 539, A57, A57. DOI: 10.1051/0004-6361/201118262. arXiv: 1112.2520 [astro-ph.HE].

Perucho, M. et al. (2004). "Stability of hydrodynamical relativistic planar jets. I. Linear evolution and saturation of Kelvin-Helmholtz modes". In: *A&A* 427, pp. 415–429. DOI: 10.1051/0004-6361:20040349. eprint: astro-ph/0407548.

Perucho, M. et al. (2014). "On the deceleration of Fanaroff-Riley Class I jets: mass loading by stellar winds". In: *MNRAS* 441, pp. 1488–1503. DOI: 10.1093/mnras/stu676. arXiv: 1404.1209 [astro-ph.HE].

Pittard, J. M. (2007). "A Clumping-independent Diagnostic of Stellar Mass-Loss Rates: Rapid Clump Destruction in Adiabatic Colliding Winds". In: *ApJ* 660, pp. L141–L144. DOI: 10.1086/518365. eprint: astro-ph/0703617.

Porth, O., S. S. Komissarov, and R. Keppens (2014). "Three-dimensional magnetohydrodynamic simulations of the Crab nebula". In: *MNRAS* 438, pp. 278–306. DOI: 10.1093/mnras/stt2176. arXiv: 1310.2531 [astro-ph.HE].

Press, W. H. et al. (1992). *Numerical recipes in Fortran 77. The art of scientific computing*. 2nd ed. Cambridge University Press.

Puls, J., J. S. Vink, and F. Najarro (2008). "Mass loss from hot massive stars". In: *A&A Rev.* 16, pp. 209–325. DOI: 10.1007/s00159-008-0015-8. arXiv: 0811.0487.

Rahoui, F. et al. (2011). "A Multiwavelength Study of Cygnus X-1: The First Mid-infrared Spectroscopic Detection of Compact Jets". In: *ApJ* 736, 63, p. 63. DOI: 10.1088/0004-637X/736/1/63. arXiv: 1105.0336 [astro-ph.HE].

Rees, M. J. (1978). "The M87 jet - Internal shocks in a plasma beam". In: *MNRAS* 184, 61P–65P. DOI: 10.1093/mnras/184.1.61P.

Romero, G. E. et al. (2003). "Hadronic gamma-ray emission from windy microquasars". In: *A&A* 410, pp. L1–L4. DOI: 10.1051/0004-6361:20031314-1. eprint: astro-ph/0309123.

Romero, G. E., M. V. Del Valle, and M. Orellana (2010). "Gamma-ray absorption and the origin of the gamma-ray flare in Cygnus X-1". In: *A&A* 518, A12, A12. DOI: 10.1051/0004-6361/200913938. arXiv: 1005.0803 [astro-ph.HE].

Romoli, C. et al. (2015). "H.E.S.S. observations of PSR B1259-63 during its 2014 periastron passage". In: *ArXiv e-prints*. arXiv: 1509.03090 [astro-ph.HE].

Runacres, M. C. and S. P. Owocki (2002). "The outer evolution of instability-generated structure in radiatively driven stellar winds". In: *A&A* 381, pp. 1015–1025. DOI: 10.1051/0004-6361:20011526.

Sabatini, S. et al. (2010). "Episodic Transient Gamma-ray Emission from the Microquasar Cygnus X-1". In: *ApJ* 712, pp. L10–L15. DOI: 10.1088/2041-8205/712/1/L10. arXiv: 1002.4967 [astro-ph.HE].

Sierpowska-Bartosik, A. and D. F. Torres (2007). "Pulsar Model of the High-Energy Phenomenology of LS 5039". In: *ApJ* 671, pp. L145–L148. DOI: 10.1086/525041. arXiv: 0708.0189.

Sierpowska, A. and W. Bednarek (2005). "γ-rays from cascades in close massive binaries containing energetic pulsars". In: *MNRAS* 356, pp. 711–726. DOI: 10.1111/j.1365-2966.2004.08490.x. eprint: astro-ph/0410304.

Sironi, L. and A. Spitkovsky (2011). "Acceleration of Particles at the Termination Shock of a Relativistic Striped Wind". In: *ApJ* 741, 39, p. 39. DOI: 10.1088/0004-637X/741/1/39. arXiv: 1107.0977 [astro-ph.HE].

Szostek, A. and A. A. Zdziarski (2008). "Effects of the stellar wind on X-ray spectra of Cygnus X-3". In: *MNRAS* 386, pp. 593–607. DOI: 10.1111/j.1365-2966.2008.13073.x. arXiv: 0710.5591.

Takata, J. et al. (2012). "Modeling High-energy Light curves of the PSR B1259-63/LS 2883 Binary Based on 3D SPH Simulations". In: *ApJ* 750, 70, p. 70. DOI: 10.1088/0004-637X/750/1/70. arXiv: 1203.2179 [astro-ph.HE].

Tam, P. H. T. et al. (2015). "High-energy Observations of PSR B1259-63/LS 2883 through the 2014 Periastron Passage: Connecting X-Rays to the GeV Flare". In: *ApJ* 798, L26, p. L26. DOI: 10.1088/2041-8205/798/1/L26. arXiv: 1412.2483 [astro-ph.HE].

Tavani, M. and J. Arons (1997). "Theory of High-Energy Emission from the Pulsar/Be Star System PSR 1259-63. I. Radiation Mechanisms and Interaction Geometry". In: *ApJ* 477, pp. 439–464. eprint: astro-ph/9609086.

Tavani, M., J. Arons, and V. M. Kaspi (1994). "Regimes of high-energy shock emission from the Be star/pulsar system PSR 1259-63". In: *ApJ* 433, pp. L37–L40. DOI: 10.1086/187542.

Tavani, M. et al. (2009). "Extreme particle acceleration in the microquasar CygnusX-3". In: *Nature* 462, pp. 620–623. DOI: 10.1038/nature08578. arXiv: 0910.5344 [astro-ph.HE].

Thompson, D. J. et al. (1977). "Final SAS-2 gamma-ray results on sources in the galactic anticenter region". In: *ApJ* 213, pp. 252–262. DOI: 10.1086/155152.

Uchiyama, Y. et al. (2009). "Suzaku Observations of PSR B1259-63: A New Manifestation of Relativistic Pulsar Wind". In: *ApJ* 698, pp. 911–921. DOI: 10.1088/0004-637X/698/1/911. arXiv: 0904.1238 [astro-ph.HE].

Volpi, D. et al. (2008). "Non-thermal emission from relativistic MHD simulations of pulsar wind nebulae: from synchrotron to inverse Compton". In: *A&A* 485, pp. 337–349. DOI: 10.1051/0004-6361:200809424. arXiv: 0804.1323.

Yoon, D. and S. Heinz (2016). "Bow-shock Pulsar Wind Nebulae Passing Through Density Discontinuities". In: *ArXiv e-prints*. arXiv: 1610.02696 [astro-ph.HE].

Yoon, D., A. A. Zdziarski, and S. Heinz (2016). "Formation of recollimation shocks in jets of high-mass X-ray binaries". In: *MNRAS* 456, pp. 3638–3644. DOI: 10.1093/mnras/stv2954. arXiv: 1508.04539 [astro-ph.HE].

Zabalza, V. et al. (2013). "Unraveling the high-energy emission components of gamma-ray binaries". In: *A&A* 551, A17, A17. DOI: 10.1051/0004-6361/201220589. arXiv: 1212.3222 [astro-ph.HE].

Zanin, R. et al. (2016). "Gamma rays detected from Cygnus X-1 with likely jet origin". In: *A&A* 596, A55, A55. DOI: 10.1051/0004-6361/201628917. arXiv: 1605.05914 [astro-ph.HE].

Zdziarski, A. A. et al. (2016a). "High-energy gamma-rays in the hard spectral state of Cyg X-1". In: *ArXiv e-prints*. arXiv: 1607.05059 [astro-ph.HE].

Zdziarski, A. A., A. Segreto, and G. G. Pooley (2016b). "The radio/X-ray correlation in Cyg X-3 and the nature of its hard spectral state". In: *MNRAS* 456, pp. 775–789. DOI: 10.1093/mnras/stv2647. arXiv: 1508.02049 [astro-ph.HE].

de la Cita, V. M. et al. (2016). "Coupling hydrodynamics and radiation calculations for star-jet interactions in active galactic nuclei". In: *A&A*

591, A15, A15. DOI: 10.1051/0004-6361/201527084. arXiv: 1604.02070 [astro-ph.HE].

de la Cita, V. M. et al. (2017a). "Gamma rays from clumpy wind-jet interactions in high-mass microquasars". In: *A&A* accepted for publication.

de la Cita, V. M. et al. (2017b). "Non-thermal radiation from a pulsar wind interacting with an inhomogeneous stellar wind". In: *A&A* 598, A13, A13. DOI: 10.1051/0004-6361/201629112. arXiv: 1611.03788 [astro-ph.HE].

del Palacio, S., V. Bosch-Ramon, and G. E. Romero (2015). "Gamma-ray binaries beyond one-zone models: an application to LS 5039". In: *A&A* 575, A112, A112. DOI: 10.1051/0004-6361/201424713. arXiv: 1412.8167 [astro-ph.HE].

von Kienlin, A. et al. (2014). "The Second Fermi GBM Gamma-Ray Burst Catalog: The First Four Years". In: *ApJS* 211, 13, p. 13. DOI: 10.1088/0067-0049/211/1/13. arXiv: 1401.5080 [astro-ph.HE].